Effect of a thermomechanical treatment on the fatigue behaviour of a quenched and tempered steel

Zur Erlangung des akademischen Grades eines
DOKTORS DER INGENIEURWISSENSCHAFTEN (DR.-ING.)

von der KIT-Fakultät für Maschinenbau
des Karlsruher Instituts für Technologie (KIT)

genehmigte
Dissertation

von

M.Sc. Amin Khayatzadeh

Tag der mündlichen Prüfung:	19. 09. 2024
Hauptreferent:	Prof. Dr.-Ing. Martin Heilmaier
Korreferent:	Prof. Dr.-Ing. Eberhard Kerscher

Kurzfassung

Die Eigenschaften der Ermüdungsfestigkeit sind für viele industrielle Anwendungen von großem Interesse, und in vielen Forschungslabors werden Untersuchungen zum Ermüdungsverhalten und zu den Schadensmechanismen bei niedrigen und hohen Ermüdungszyklen durchgeführt, um die Mechanismen des Ermüdungsverhaltens zu analysieren und vorherzusagen. Aufgrund seiner hervorragenden Ermüdungseigenschaften ist Stahl einer der besten Kandidaten für Anwendungen mit hoher Ermüdungsfestigkeit, und unter den Stählen ist SAE4140 Vergütungsstahl (deutsche Bezeichnung: 42CrMo4) einer der favorisierten Stähle für Anwendungen, bei denen eine hohe Ermüdungsfestigkeit gefordert ist. In der vorliegenden Arbeit wurde eine thermomechanische Behandlung (engl. thermomechanical treatment (TMT)) bei der maximalen Temperatur der dynamischen Reckalterung (engl. dynamic strain aging (DSA)) entwickelt und an SAE4140 im vergüteten Zustand durchgeführt, um deren Einfluss auf das Ermüdungsverhalten zu analysieren. Es wurde gezeigt, dass für $N_f \geq 7 \times 10^5$ Zyklen, bei denen der kritische Riss an einem nichtmetallischen Einschluss innerhalb des Volumens beginnt, die angewandte TMT die Dauerfestigkeit um 8% erhöht. Während der thermomechanischen Behandlung erhöht die plastische Verformung im Temperaturbereich der dynamischen Reckalterung die Versetzungsdichte im Gefüge, insbesondere um die Einschlüsse herum. Diese Erhöhung der Versetzungsdichte könnte zu einer stabileren Versetzungsstruktur um die nichtmetallischen Einschlüsse herum führen, die die

Rissbildung verzögert oder verhindert und somit zu einer höheren Lebensdauer und einer höheren Ermüdungsfestigkeit führt. Bei $N_f < 7 \times 10^5$ Zyklen, bei denen die Rissbildung an der Oberfläche erfolgt, ist jedoch nicht nur keine Verbesserung des Ermüdungsverhaltens zu beobachten, sondern auch eine erhebliche Verschlechterung der Ermüdungslebensdauer. Es wurde festgestellt, dass die zyklische mechanische Zug-Druck-Belastung (mechanische Behandlung) während der thermomechanischen Behandlung zu einer signifikanten Verringerung der Druckeigenspannung und einer Einführung von Zugeigenspannungen an der Oberfläche und unter der Oberfläche des Probekörpers führt. Im Falle der Rissinitiierung an der Oberfläche und unter der Oberfläche vereinfacht die eingeführte Zugeigenspannung die Rissbildung und das Risswachstum im Vergleich zu den Proben ohne mechanische Behandlung und führt letztlich zu einem früheren Ermüdungsversagen in diesem Bereich. Darüber hinaus wurde festgestellt, dass im Falle einer inneren Rissbildung durch den nichtmetallischen Einschluss ($N_f \geq 7 \times 10^5$ Zyklen) nur eine kombinierte thermomechanische Behandlung bei der Temperatur des maximalen DSA die den Einschluss umgebende Mikrostruktur stabilisieren und die Ermüdungsgrenze erhöhen kann. Andererseits haben individuelle thermische Behandlungen (engl. thermal treatment (TT)) und mechanische Behandlungen (engl. mechanical treatment (MT)) negative bzw. keine nennenswerte Auswirkungen auf die Ermüdungsgrenze.

Darüber hinaus zeigt die Analyse der Bruchflächen von TMT- und wärmebehandelten (engl. heat treatment (HT)) Proben einerseits keine Korrelation zwischen der Einschlusstiefe und der Fisheye-größe und der Ermüdungslebensdauer. Es wurde jedoch sowohl bei TMT- als auch bei HT-Proben festgestellt, dass die Form des Einschlusses eine wichtige Rolle bei der Rissbildung und der Ermüdungslebensdauer der Proben spielt. Es wurde festgestellt, dass kleine Einschlüsse mit scharfen Kanten ebenso nachteilig sein können wie runde Einschlüsse mit deutlich größeren Einschlussflächen, da sich die Spannungen um die scharfen Kanten herum während der Ermüdungsversuche stärker konzentrieren.

Abstract

Fatigue strength properties are of high interest to many industrial applications, and investigations on fatigue behaviour and damage mechanisms under low and high cycle fatigue are being conducted at many research laboratories to analyse and predict the fatigue behaviour mechanisms. Due to the high fatigue properties of steel, it is one of the best candidates for applications requiring fatigue strength, and among steels, SAE4140 quenched and tempered steel (German designation: 42CrMo4) is one of the most favourable for high fatigue strength applications. In the current work, a thermo-mechanical treatment (TMT) has been developed and conducted on quenched and tempered SAE4140 steel at the maximum temperature of dynamic strain aging (DSA) to analyse its influence on fatigue behaviour. It has been shown that for $N_f \geq 7 \times 10^5$ cycles, where the critical crack initiates at non-metallic inclusion inside the volume, the applied TMT increases the fatigue strength by 8%. During the TMT, plastic deformation in the temperature range of DSA increases the dislocation density in the microstructure, especially around the inclusions. This increase in the dislocation density could introduce a more stable dislocation structure around the non-metallic inclusions, which delays or prevents crack initiation and thus, resulting in higher lifetimes and increased fatigue strengths. However, for $N_f < 7 \times 10^5$ cycles, where the crack initiation is at the surface, not only can not be seen any improvement in the fatigue behaviour, but also a significant degradation in the fatigue lifetime has been detected. It has been

found that the applied cyclic tensile-compressive mechanical loading (mechanical treatment) during TMT leads to a significant reduction in compressive residual stress and an introduction of tensile residual stress at the surface and subsurface of the specimen. In the case of surface and subsurface crack initiation regimes, the introduced tensile residual stress simplifies crack nucleation and growth compared to the specimens without an applied mechanical treatment and it ultimately leads to earlier fatigue failure in this regime. Furthermore, it has been realised that in the case of internal crack initiation from non-metallic inclusions ($N_f \geq 7 \times 10^5$ cycles), only a combined thermo-mechanical treatment at the temperature of maximum DSA can stabilize the microstructure surrounding the inclusion and increase the fatigue strength. On the other hand, individual thermal treatment (TT) and mechanical treatment (MT) have a negative and negligible effect on the fatigue strength, respectively.

Furthermore, fracture surface analysis of both TMT and heat-treated (HT) specimens indicates no correlation between inclusion depth and fisheye size on one hand and the fatigue lifetime on the other hand. However, in both TMT and HT specimens, it has been found that the shape of inclusion plays an important role in the crack initiation and fatigue lifetime of the specimens. It is observed that small inclusions including sharp edges can be as detrimental as round inclusions with significantly larger inclusion areas due to higher stress concentration around the sharp edges during fatigue experiments.

Abbreviations

DSA	Dynamic Strain Aging
EDS	Energy Dispersive X-Ray Spectroscopy
FGA	Fine Granular Area
FCG	Fatigue Crack Growth
GBF	Granular Bright Facet
HCF	High Cycle Fatigue
HT	Heat Treatment
HV	Vickers Hardness
LCF	Low Cycle Fatigue
MT	Mechanical Treatment
NP	Non-shot Peened
RA	Rough Area
RCW	Round Cut Wire
SA	Smooth Area
SEM	Scanning Electron Microscope
TMT	Thermomechanical Treatment
TT	Thermal Treatment
VHCF	Very High Cycle Fatigue
XRD	X-Ray diffraction analysis

Table of contents

Acknowledgement

I extend my sincere gratitude to the Institute for Applied Materials - Materials Science (IAM-WK) at the Karlsruhe Institute of Technology (KIT) for providing the platform for this research, funded by the German Research Foundation (DFG). Foremost, my gratitude goes to Prof. Martin Heilmaier for providing the opportunity to write this dissertation at IAM-WK. I am especially appreciative of his scientific guidance and prompt, detailed feedback on manuscripts. Special thanks to Prof. Kerscher for being the project partner in this project and for all his valuable contributions, discussions, and outstanding collaboration.

I am grateful to my department heads, Dr. Karl-Heinz Lang and Dr. Stefan Guth, for their support and fruitful collaboration. Additionally, I extend acknowledgments to our project partner at the Technical University of Kaiserslautern, Jan Sippel, for his valuable contributions and efforts during this project.

I express appreciation to Dr. Jens Gibmeier for his contribution to the residual stress analyses, one of the key highlights in this research project.

Furthermore, I want to convey my sincere appreciation to Sebastian Höhne, Ralf Rößler, Tobias Unger, Sven Burkhardt, Marc Brecht, and Dietmar for keeping testing machines operational and solving complex problems.

I extend special thanks to all my colleagues for their support throughout this research, with a particular acknowledgment to Lars Riedel for his tips and to Michaela Nagel for her continuous assistance in metallography.

I would like to express my appreciation for the dedication and efforts of student assistants Alexander Zeizinger (Sascha) and Soheil Molaei during the course of this research project.

Lastly, my deepest thanks go to my family and girlfriend for their valuable support.

Karlsruhe, in February 2024 Amin Khayatzadeh

1 Introduction and Motivation

One of the most significant mechanical properties for engineering applications is the fatigue strength of steel. As a result of the common fatigue failure in the long lifetime of moving machine parts, there is a remarkable demand to develop steels with high fatigue strength in the industry [1,2]. Among different kinds of steels, SAE4140 quenched and tempered steel (German designation: 42CrMo4) shows very good fatigue strength and is favourable for cyclic loading applications [3]. There are three different regimes for fatigue analyses: low-cycle fatigue (LCF), high-cycle fatigue (HCF), and very high-cycle fatigue (VHCF) regimes. Low Cycle Fatigue (LCF) refers to a form of fatigue characterized by plastic deformation occurring and leading to failure within a relatively low number of cycles, typically less than 10^5. In contrast, High Cycle Fatigue (HCF) failure occurs under alternating stresses within the elastic range, resulting in a significantly higher number of cycles, typically exceeding 10^5 [4,5]. Furthermore, when the number of cycles surpasses 10^7, it is categorized as Very High Cycle Fatigue (VHCF) [5]. However, the fracture surface analysis shows that the lifetime of quenched and tempered steels in the HCFand VHCF regimes is restricted by internal crack initiations at non-metallic inclusions, from which fatigue cracks initiate and grow [6–9]. Physical and chemical processes during melting and solidification process of steel production are the main causes of non-metallic inclusion formation [8]. Contrary to HCF and VHCF regimes, in the LCF regime crack initiation at the surface or

subsurface is the main fatigue failure reason [6–9]. There are several studies to increase the fatigue strength of steel and minimize crack initiation at non-metallic inclusions. One approach to avoid the negative influences of inclusions is to enhance the steel purity and limit the formation of critical inclusions during production [10,11] or to control the size of inclusion with rare earth addition [12]. Another promising method to reach higher fatigue strength and better fatigue behaviour of steel is a thermo-mechanical treatment (TMT) in the temperature regime of maximum dynamic strain aging (DSA) which can be conducted after the production of steel [13,14]. TMT refers to a process in which a steel is subjected to both thermal and mechanical treatments at the same time. During TMT, an interaction occurs between dislocations and alloying atoms (e.g., carbon in the case of steels), in which alloying atoms are impeded in their movement. However, the chosen temperature for this process is the temperature of maximum DSA, where diffusing solute atoms interact with moving dislocation [14]. As a result of DSA and diffusing alloying atoms into the dislocation (especially around the non-metallic inclusion), a dislocation structure with higher dislocation density could be formed which is remarkably more stable than before [13,14].

Kerscher proved an increase in the fatigue strength of high-strength bearing steel in the HCF regime after applying a TMT at the temperature of maximum DSA [15]. It is assumed that as a result of TMT at the temperature of

maximum DSA, dislocation undergoes a change, which strengthens the microstructures around the non-metallic inclusions and consequently prevents or delays crack initiation, ultimately increasing the fatigue strength [15]. However, the details of the strengthening mechanism taking place around the inclusions due to a TMT are still not fully understood. Moreover, it is unclear whether the shape, area, and position relative to the surface (e.g., depth) of inclusion affect the effectiveness of a TMT or whether a TMT may affect the shape, area, and position of critical crack-initiating inclusions. Other researchers also tried to analyse and investigate the influence of shape, size, and inclusion depth of crack-initiating non-metallic inclusions on fatigue lifetimes. However, the majority of these studies are not experimental investigations and they rely on simulations [16,17]. Several experimental studies have been conducted indicating that there is no discernible correlation between the areas of critical non-metallic inclusions or the depth of inclusions and the cyclic lifetime (N_f). [18–20]. On the contrary, other investigations indicated that the area and inclusion depth of critical inclusions reduce with increasing fatigue lifetime [21,22]. Analysis of the effect of non-metallic inclusions on fatigue behaviour requires consideration of different parameters such as type, shape, area, distribution of these inclusions, as well as the applied stress. Consideration of all these parameters makes analysis of fatigue behaviour more complicated [23,24].

In addition, it has been observed by other investigations that cyclic loading treatment at different temperatures may lead to the generation of tensile residual stress at the surface and subsurface of the specimens [25]. It is known that the presence of tensile residual stresses or a significant reduction of compressive residual stresses increases the fatigue crack growth rates and consequently decreases the fatigue strength and lifetime [26,27]. Since TMT contains both mechanical and thermal treatments, including cyclic mechanical loading at the temperature of maximum DSA, residual stress analyses need to be conducted to investigate on the effects of TMT on the residual stress at the surface and subsurface of the TMT specimens.

This work aims to obtain a suitable TMT at a temperature of maximum DSA for quenched and tempered steel SAE4140 to enhance its fatigue strength and fatigue lifetimes in both LCF and HCF regimes. The focus of other investigations regarding TMT at the temperatures of DSA was mainly on the HCF and VHCF regimes [14,28]. In this work, the fatigue behaviour of TMT specimens within the LCF regime and the regime where crack initiation occurs from the surface and subsurface is also analysed and a solution to improve the fatigue lifetime and minimize the negative influence of TMT in this regime is proposed.

Furthermore, the study focuses on the role of fisheye formation in the fatigue behaviour and fatigue lifetime of specimens and the influence of important parameters of non-metallic inclusions such as shape, area, and position on the fatigue lifetime of steel SAE4140 in the HCF regime. The last

approach of this work is to find the answer whether a TMT, which improves the fatigue behaviour in the HCF regime [13,14], influences the shape, area, and position of critical inclusions and whether the TMT effectiveness is affected by these parameters.

Chapter 2 presents an introduction to the fundamentals of fatigue failure and crack initiation, DSA effect, and cyclic hardening/softening. It also reviews existing research on TMT conducted at the temperature of dynamic strain aging (DSA). Chapters 3 and 4 present the used material, applied heat treatment (HT) and experimental procedures, respectively. The process of all additional treatments including TMT, mechanical treatment (MT) and thermal treatment (TT) after initial heat treatment (HT) are presented in the Chapter 5. The results of fatigue and fracture surface analyses, with a focus on TMT and HT specimens, are presented and discussed in Chapters 6 and 7, respectively. Finally, a conclusive summary including important findings are provided in Chapter 8.

2 Fundamentals

2.1 Fatigue failure and lifetime

Fatigue failures are the result of alternating stresses, which may be considerably lower than the stress required to cause failure during a single loading. Any part or moving component can be affected by fatigue [29]. The first approach to fatigue began with Albert who published the first fatigue test result in 1837 [30]. However, Wöhler was the first engineer who conducted investigations on railway axles. He systematically investigated the relationship between stress amplitude and number of cycles to failure. Furthermore, he introduced the concept of fatigue strength [31]. The S-N curves or Wöhler curves are based on his works. Figure 2.1 represents three different elements of an S-N curve including (a) the line of the finite life region, which increases by reducing the stress amplitude; (b) the knee point, which shows the minimum number of fatigue cycles at which no fatigue failure occurs despite increasing stress cycles; and (c) the horizontal line representing the fatigue strength, below which no fatigue failure can be observed [32].

The modified Miner's rule which is shown in figure 2.1, is a simple way to consider the influences of stresses below the fatigue strength [33].

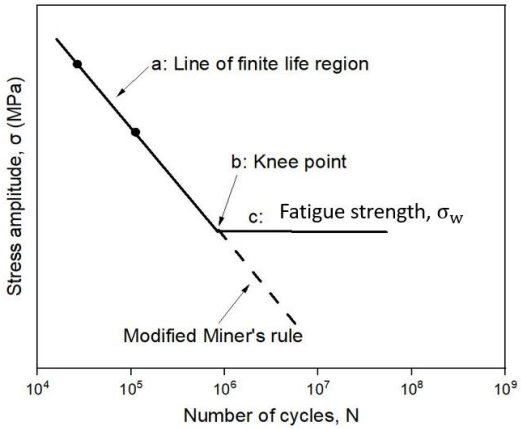

Figure 2.1 An example of S-N curve consisting different elements [32].

The process eventually leading to fatigue failure can be divided into the following stages: (1) microcrack nucleation; (2) short crack growth; (3) long crack growth; and (4) final failure. Microcrack nucleation and short crack growth stages are often considered as ‘‘crack initiation period” while long crack growth is termed as ‘‘crack propagation period” [34,35]. The complete service life to fatigue failure, N_f, can be determined from the number of cycles, N_i, required for fatigue crack initiation and the number of cycles, N_p, required for a crack to propagate from the initial to the critical crack length, at which final failure can be expected to occur [34].

$$N_f = N_i + N_p \quad (1)$$

2.2 Fatigue behaviour of steels

As it is discused above, the term fatigue failure contains two stages: crack initiation and crack propagation. In order to analyse the fatigue behaviour of steel, it is essential to analyse both, crack initiation and crack propagation. Furthermore, crack initiation in steels occurs either at the surface or subsurface of the specimen or inside the volume, depending on the stress level and lifetime [7]. Both, surface and internal crack initiations have their own characteristics, which will be discussed in detail.

2.2.1 Crack initiation at surface

Surface crack initiation usually takes place at high stress amplitudes and low cycle numbers, occurring prior to reaching 10^6 cycles to failure [36,37]. Fatigue fracture surface analysis in Figure 2.2a shows a typical example of surface crack initiation. It can be seen that no inclusion is found at the crack initiation site. However, in some cases, inclusions can be found at the surface and subsurface crack initiation sites of the specimen (Figure 2.2b) [38].

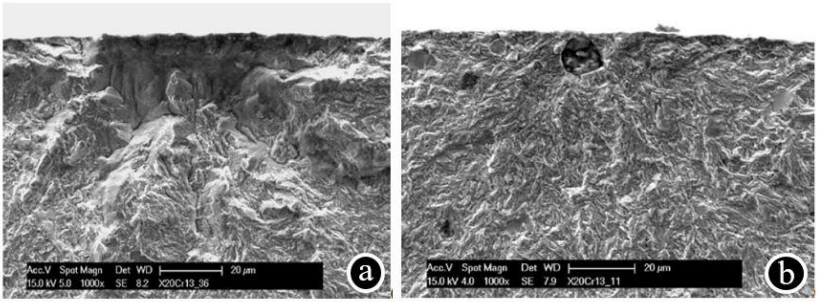

Figure 2.2 Crack initiation at the surface of martensitic chromium stainless steel. (a) Surface crack initiation without inclusion at 860 MPa with a lifetime of 2.24×10^5 cycles; (b) Surface crack initiation with inclusion at 753 MPa with a lifetime of 1.7×10^8 cycles [38].

Minimizing surface roughness plays an important role in avoiding crack initiation at the surface of the specimens without inclusions [39].

2.2.2 Internal crack initiation

Internal cracks initiate typically after more than 10^6 cycles and are the dominant fatigue failure mechanism at lower stress amplitudes [37]. One of the main features of internal crack initiation is that cracks normally initiate at non-metallic inclusions and are surrounded by a circular area called fisheye which is shown in Figure 2.3 [21].

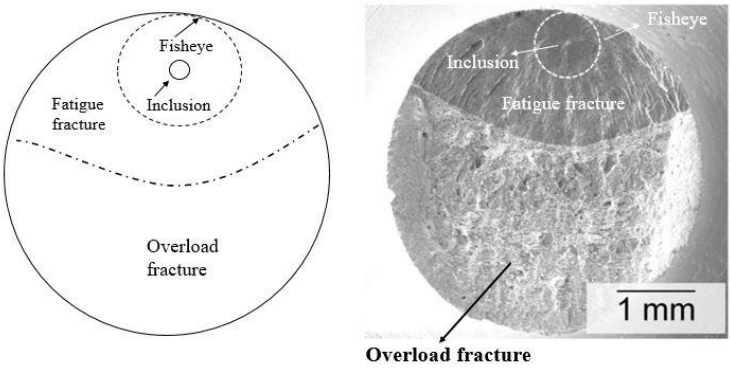

Figure 2.3 Schematic illustration and SEM fracture surface analysis of an internal fatigue crack initiation [21].

This fatigue fracture zone contains crack initiation from the inclusion and fisheye formation and progresses until the material remaining is no longer strong enough to support the load and it finally breaks (overload fracture). It may take millions of cycles for the crack to travel from the fatigue fracture zone to the overload fracture zone [40].

- **Internal crack initiation at non-metallic inclusions**

The fatigue strength of steels in the HCF and VHCF regimes is limited due to inhomogeneities in the microstructure, and especially non-metallic inclusions inside the volume from which fatigue cracks initiate and grow [6–9]. The non-metallic inclusions in steel are due to physical and chemical processes during melting and solidification process of steel production [8]. To reach higher fatigue strength, it is of high interest to minimize the negative influence of non-metallic inclusions. One approach is to improve steel

cleanliness and control non-metallic inclusions during production [10]. Non-metallic inclusions can be categorized and analysed based on their type (chemical composition), size, shape, and distance to the surface of the specimen (inclusion depth).

- **Type and morphology of non-metallic inclusions**

Non-metallic inclusions can be categorized based on the chemical compositions as oxides (e.g. SiO_2, Al_2O_3, Ti_2O_3, MnO and also complex oxides MnO-SiO_2, CaO-Al_2O_3 or AlCaO), sulphides (e.g. MnS, CaS), nitrides (e.g. TiN, BN, VN) and carbides (e.g. TiC). Furthermore, complex inclusions have also been observed, which are a combination of the above-mentioned inclusions, such as oxy-sulphides of cerium (Al_2O_3–MnS), and multi-phase inclusions (e.g. MnS–TiN–CeO_2–CeS) [41–43]. Each inclusion type has its own characteristics; however, the focus of this work is on the AlCaO (CaO-Al_2O_3) inclusions, which are mainly found as crack initiation sites for quenched and tempered steel SAE4140.AlCaO (CaO-Al_2O_3) inclusion is the most common and detrimental inclusion type among various steel grades. These inclusions are mainly spherical [42,44,45].

- **Size of non-metallic inclusion**

The size of inclusion is dependent on the type of inclusion and varies from about 1 µm to 50 µm. The biggest inclusion sizes belong typically to the oxide inclusions containing dominant elements of Al and Ca (e.g. CaO-

Al_2O_3) [23]. However, the size of inclusion itself does not have a considerable influence on the fatigue lifetime and crack propagation mechanism [18,19]. As can be seen from Figure 2.4, the size (square root of critical non-metallic inclusion area), $\sqrt{area_{inc}}$, scatters significantly versus fatigue lifetime [19].

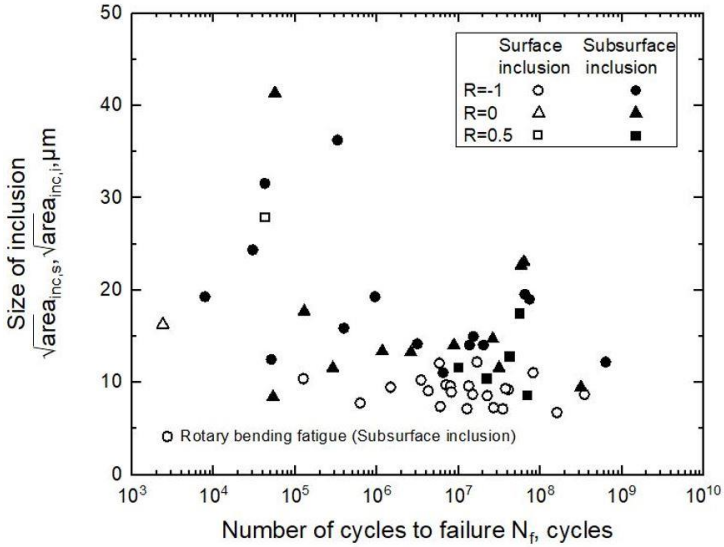

Figure 2.4 Relationship between size of inclusion and lifetime of high carbon–chromium bearing steel with the inclusion type of TiC [19].

- **Depth of non-metallic inclusion (inclusion depth)**

The term 'inclusion depth' signifies the distance between the center of inclusion and the nearest free surface edge [20]. Figure 2.5 shows the relationship between inclusion depth and lifetime for axial and rotary loading

fatigue for high carbon–chromium- bearing steel. The inclusion depths are widely distributed across the specimen from 40 µm and 1240 µm, and no correlation can be observed between N_f and the inclusion depth [19].

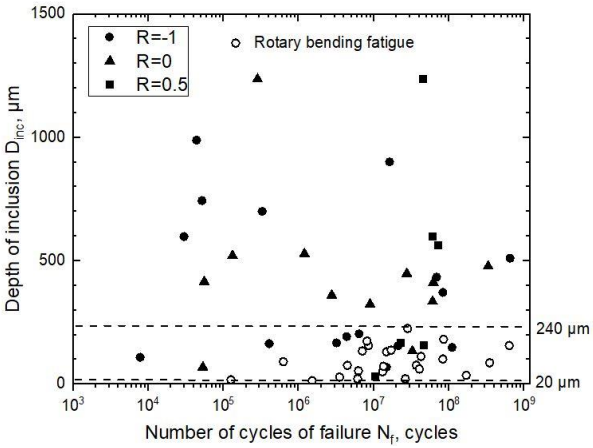

Figure 2.5 Evaluation of the experimental relationship between the depth of inclusion from the surface and the lifetime of high carbon–chromium- bearing steel with the inclusion type of TiC [19].

2.2.3 Crack propagation in steels

As discussed in subsection 2.1, the next stage after the crack initiation period is crack propagation until failure of the specimen or component. The crack propagation stage may be considered a part of long crack growth. In case of internal crack initiation at non-metallic inclusions, the fracture surface may exhibit a Fine Granualar Area (FGA) and fisheye formation around the inclusion [46,47].

- **Formation of fine granular area (FGA) and fisheye during crack propagation**

The formation of a fisheye may be comparable to long fatigue crack growth and is a part of the crack propagation stage until the failure of the specimen [46]. A typical fisheye failure is characterized by an optically brighter area, while the inclusion is located at the center of it. A rough region might be seen around the inclusion which is called GBF (Granular bright facet) or Fine Granular Area [18]. Figure 2.6 depicts a schematic illustration of formed fisheye and GBF during crack propagation at the fracture surface of the specimen.

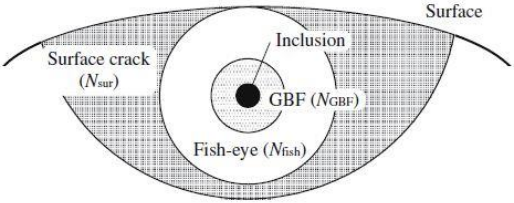

Figure 2.6 Schematic representation of formed fisheye and GBF during crack propagation at the fracture surface of the specimen [18].

However, it is noticeable that an FGA does not necessarily form around a crack-initiating inclusion. Figures 2.7a and 2.7b show two internal fatigue crack initiations at inclusions with and without FGA formation respectively.

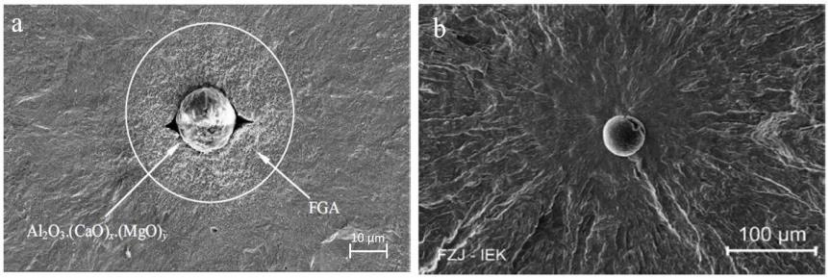

Figure 2.7 Fracture morphology analysis in the VHCF regime: (a) Formation of FGA around the inclusion (100Cr6 steel, σ_a= 780 MPa, $N_f = 1.76 \times 10^8\ cycles$); (b) Crack propagation without FGA formation (34CrNiMo6, σ_a= 430 MPa, $N_f = 2.57 \times 10^8\ cycles$) [48].

The fisheye grows in a vacuum and typically extends to the surface of the specimen. Under the influence of ambient air, oxidation-assisted crack propagation occurs, which is much faster compared to crack growth in a vacuum (Figure 2.8a) [18,49]. However, in some cases, final failure takes place before the fisheye reaches the surface of the specimen (shown in Figure 2.8b) [50].

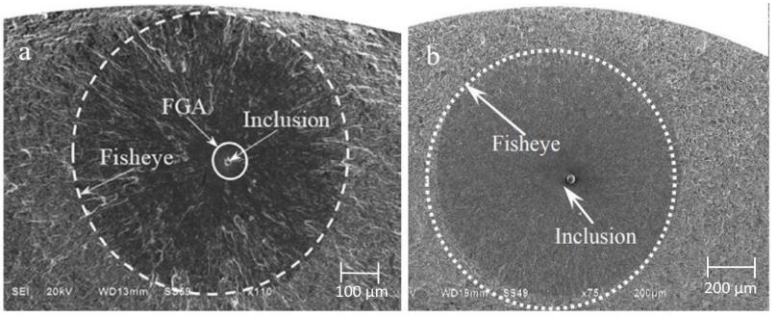

Figure 2.8 (a) Growth of fisheye until it reaches the free surface (Cr-Ni-W Gear Steel (main chemical composition (wt %) is 0.16 C, 0.19 Si, 0.33 Mn, 1.55 Cr, 4.22 Ni, 0.97 W, 0.01

V), σ_a= 600 MPa, $N_f = 2.93 \times 10^7\ cycles$) [49]; (b) Internal fisheye formation (X5CrNi18-10, σ_a= 575 MPa, $N_f = 4.25 \times 10^6\ cycles$) [50].

- **Growth of fisheye at different stages**

Fisheyes on fracture surfaces often show a circular smooth area (SA) around the inclusion. This kind of fisheye formation occurs within a single stage, and the resulting fracture surface exhibits two different zones (FGA and SA). On the other hand, the growth of fisheye may also occur in two different stages (three different zones) that may contain FGA around the inclusion, SA, and a rough area (RA), which can form around the SA [46,47]. The transition from a smooth to a rough fisheye surface goes along with a significant increase in crack propagation rate. Figure 2.9a depicts fisheye growth in two stages, and Figure 2.9b shows the corresponding increasing crack growth rate due to the transition from smooth to rough [46].

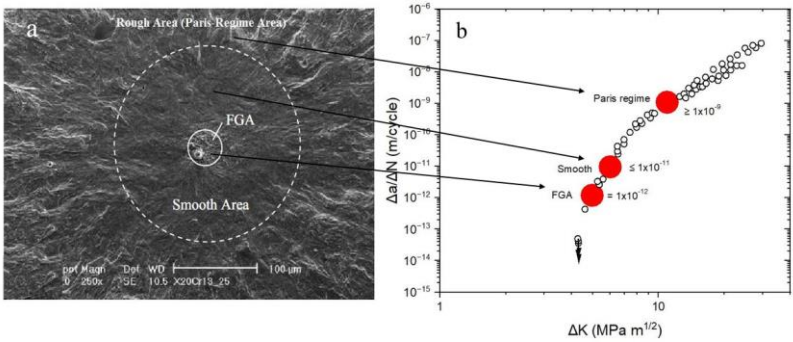

Figure 2.9 (a) Growth of fisheye at differents stages (a transition from SA to RA); (b) Estimation of fisheye growth rates and its Δk values based on the long fatigue crack growth curve (FCG curve) [46].

2.3 Stress concentration around the inclusion and defect

Small defects and non-metallic inclusions are among the main causes of crack initiation and fatigue failure of steels. The main reason is that during fatigue failure the stress concentration and distribution around the inclusion or defect is significantly higher than other parts of the specimen or component. This ultimately leads to the initiation and growth of the crack, and subsequently, fatigue failure. Parameters such as the position (whether it is at the surface or inside the volume), the shape of inclusion or defect, the size of defect or inclusion, and the adhesion of inclusion to the matrix, etc can have remarkable influences on the stress concentration and distribution around the inclusion or defect [51,52].

2.3.1 Maximum stress intensity factor (K_{max})

The maximum stress intensity factor (K_{max}) is an approximate way of analysing the maximum stress distribution around a flaw or defect. Murakami suggested K_{max} for many arbitrary inclusion and defect shapes. He obtained an empirical relation between K_{max} on one hand, and inclusion or defect area and the maximum normal stress at the critical position of the inclusion on the other hand [1,52]. According to his quantitative equations, the surface inclusions, lacking neighboring grains, therefore, the maximum stress intensity around them are higher than an inclusion of the same size in

a location inside the volume [1,53]. Depending on the location of the defect or inclusion, it can be estimated as follows:

$K_{max} = 0.65 \times \sigma_a \times \sqrt{\pi\sqrt{area}}$ for a surface defect or inclusion (2)

$K_{max} = 0.5 \times \sigma_a \times \sqrt{\pi\sqrt{area}}$ for an internal defect or inclusion (3)

Murakami considered the inclusion or defect as a crack initiation point. However, the largest inclusion or defect is not necessarily the most detrimental one, since the location and shape of inclusion or defect also play important roles [16,52,54].

2.4 Cyclic hardening/softening under stress-controlled condition

Cyclic hardening and softening are mechanical behaviours exhibited by materials subjected to repeated loading and unloading cycles. In the case of cyclic hardening, the interactions among dislocations hinder their further movement, resulting in an increase in the materials' resistance to deformation. Cyclic hardening under stress-controlled condition is present when the cyclic stress amplitude remains constant and the cyclic strain amplitude decreases as the number of cycles increases. Consequently, cyclic softening is the opposite phenomenon, where a material becomes less resistant to deformation as it undergoes cyclic loading and unloading [55]. During cyclic

softening, the cyclic strain amplitude increases with increasing number of cycles [55,56]. Figure 2.10 shows the stress-controlled (342 MPa) cyclic hardening effect of bearing steel at 335 °C. Due to cyclic hardening, after the first cycle, the loop shrinks in width, which is a reduction in plastic strain amplitude [13].

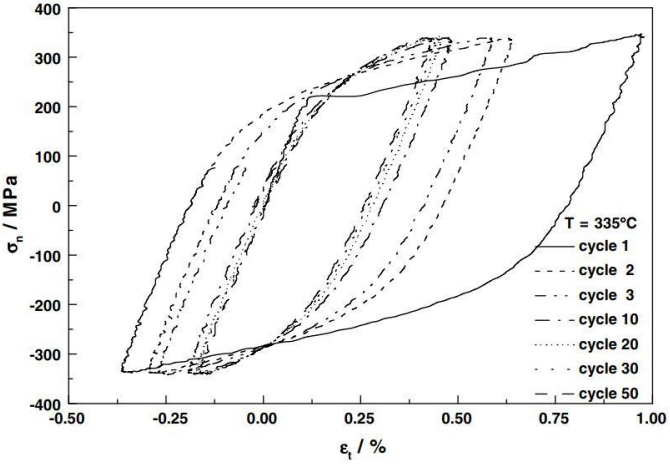

Figure 2.10 Cyclic hardening effect at 335 °C under stress-controlled condition (342 MPa) [13].

2.5 Influence of treatment in the temperature range of dynamic strain aging on the fatigue behaviour of steel

2.5.1 Dynamic strain aging (DSA)

Dynamic strain aging (DSA) is described as the interaction between diffusing solute atoms and moving dislocations, which may be temporarily arrested. DSA is highly dependent on the temperature and strain rate, which both affect the mobility of dislocations and diffusing solute atoms [57,58]. In other words, during DSA, the strain rate affects the dislocation velocity, and temperature influences the diffusion speed of solute atoms [59]. The diffusion rate of solute atoms corresponds to the temperature, which means that by increasing the temperature during DSA, the solute atom diffusion rate and consequently, the local solute concentration increase [60]. DSA mainly occurs when the strain rate and temperature are in the range, where diffusing solute atoms and gliding dislocation have approximately the same velocity, allowing the solute atoms to pin the mobile dislocations. During DSA, serrated yielding can be observed as a result of a rapid generation of new dislocations. In the process of DSA and introducing new dislocations, the stress increases, however once the dislocations are released, the stress drops to sustain their movement until the solute atoms diffuse and repin these dislocations. At this point, the stress increases again to introduce new dislocations [61]. Serrated flow curves, which are associated with DSA,

have been observed in a wide range of alloys, where interstitial and substitial solutes have been considered as the cause [62]. This macroscopic unstable plastic flow pattern which is associated with the phenomenon of DSA under certain regimes of strain rate and temperature is called Portevin–Le Chatelier (PLC) effect [62,63]. Figure 2.11 represents the PLC effect during DSA in the plastic region of stress-strain curve of NiCr22Mo9Nb (Inconel 625) which occurs from 200 °C to 500 °C at constant strain rate of $2 \times 10^{-4}\ s^{-1}$. The maximum PLC effect can be seen at 500 °C [64].

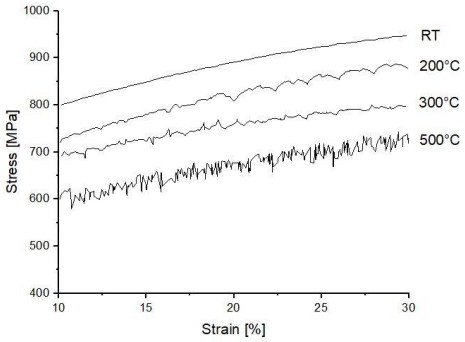

Figure 2.11 PLC effect during DSA in the plastic region of stress-strain curve of NiCr22Mo9Nb at constant strain rate of $2 \times 10^{-4}\ s^{-1}$ and temperatures of 200 °C, 300 °C and 500 °C [64].

Materials known to exhibit discontinuities in deformation due to DSA microprocesses contain various alloys, including Ni, Cu, Al, Au, and V. Furthermore, this phenomenon is observable in both body-centered cubic (bcc) and face-centered cubic (fcc) steels and different iron-based alloys

[13,58,60–62]. In the case of iron-based alloys, solute atoms such as C, Si, Mn and, Ni can be considered responsible for DSA [62].

2.5.2 Influence of DSA on the strengthening of the microstructure

During plastic deformation in the DSA regime, and due to interacting dislocations with alloying elements (e.g., carbon in the case of steels), and are, thus, impeded in their movement. This locking process can boost the resistance to any further dislocation movement, thereby strengthening the microstructure [13,65].

- **Effect of DSA temperature on the strengthening**

Figure 2.12 shows the influence of DSA temperature ranges on the strengthening effect of bearing steel SAE52100 during cyclic loading. It is observable that the plastic strain amplitude at a given stress level of 342 MPa varies for different temperatures. For all temperatures, cyclic hardening can be seen. At a temperature of 380 °C, the plastic strain amplitude remains stable after a few strengthening cycles. However, the maximum strengthening effect occurs at the temperature of 335 °C, which can be seen in a reduced plastic strain amplitude [13].

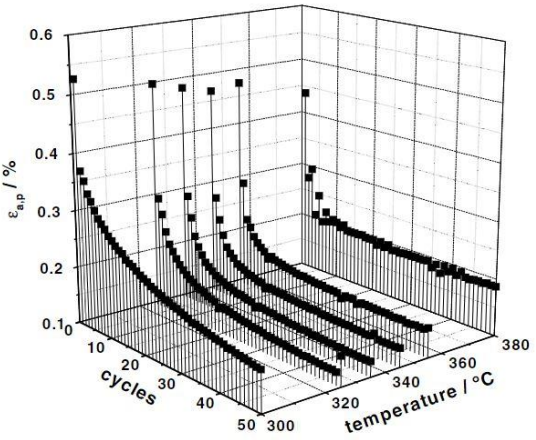

Figure 2.12 Influence of DSA temperature on the strengthening of SAE52100 [13].

The reason for the reduction in strengthening at a temperature lower and higher than 335 °C can be explained by the lower and higher diffusion rate of solute atoms which cannot be adjusted to the mobile dislocation and therefore a lower immobilisation of dislocations [13].

2.5.3 Influence of DSA on the fatigue strength of steel

As described in subsection 2.3, the crack initiation from inclusion is one of the most common reasons for the fatigue failure of steels. One possibility to increase the fatigue strength of steel in the HCF and VHCF regimes is the strengthening of the microstructure around the inclusion by DSA. As a result of DSA and diffusing solute atoms into the dislocation around the

non-metallic inclusion, a new dislocation structure with higher dislocation density could be formed which is remarkably more stable than before and therefore, it could lead to an increase in fatigue strength [13,14,65]. To strengthen the dislocation structure around the inclusions, a thermomechanical treatment (TMT) in the temperature range of DSA can be applied [13,14].

- **Influence of a TMT in the DSA regime on the fatigue strength of steels**

Increasing the fatigue strength of high strength steels by a combination of both mechanical and thermal treatments, including cyclic mechanical loading at the temperature of maximum DSA (TMT) has been proved in the HCF regimes. Kerscher showed that applying stepwise increasing load amplitude at the temperature of maximum DSA enables us to reach the DSA strengthening effect. Since the crack initiation in the HCF regime is mainly from inclusion, the DSA strengthening effect could delay or prevent the initiation of the crack [13]. Figure 2.13 shows the fatigue behaviour of martensitic SAE52100 in the initial state and after two different thermomechanical treatments designated as TMT1 and TMT2. The TMT1 was conducted at the temperature of maximum DSA, which is 275 °C, with a constant load amplitude of 1740 MPa. The results show no improvement in the fatigue lifetime and compared to the initial state, the fatigue strength of specimens with TMT1 has been reduced. However, the TMT2, which differs from TMT1 as the applied load was increased at every fifth cycle by

equidistant steps to the same maximum load amplitude as TMT1. The same temperature which was used during TMT1 is also applied for TMT2. The TMT2 can increase the fatigue strength from 940 MPa (initial state) to 1060 MPa (as shown in Figure 2.13) [14,66].

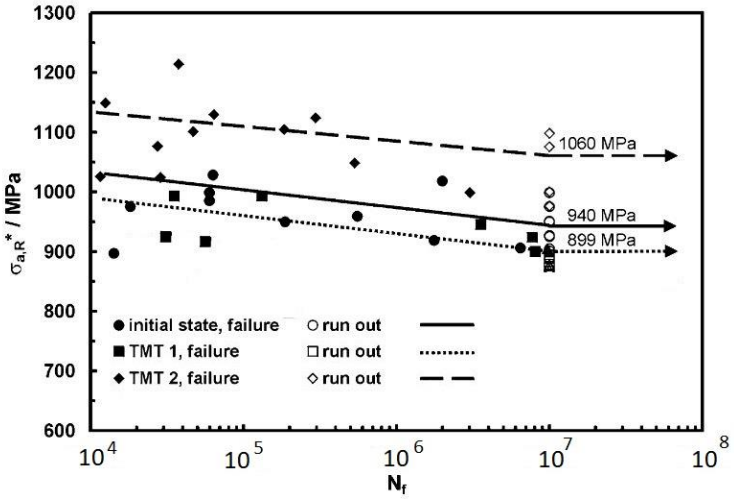

Figure 2.13 Comparison of S-N curve for initial state and after two different TMT treatments [14].

In contrary to a TMT, a pure thermal treatment (TT) at the temperature of maximum DSA does not increase the fatigue strength. In fact, it decreases the fatigue strength due to annealing effects, which reduce the hardness and strength of the material [14].

2.6 Influence of residual stresses on the crack propagation and fatigue behaviour

Residual stresses are stresses which remain in the body of material after manufacturing or any treatments in the absence of external forces or thermal gradients [67]. Residual stresses can be either beneficial or detrimental to the behaviour of the components in service depending on their sign, magnitude, stability, material's state, loading, and environmental conditions. It is well-known that residual stress has a significant influence on fatigue crack growth and fatigue strength [68]. It has been reported by several investigations that the presence of tensile residual stress or a significant reduction in compressive residual stress increases the fatigue growth rates and consequently, decreases the fatigue strength and lifetime of specimens and components. On the other hand, the generation of compressive residual stress impedes crack propagation, which can cause longer lifetimes and improves the fatigue strength of the specimen or component [26,27]. Residual stresses can have different origins and they are usually caused by misfits. These misfits can occur between different phases, different regions, and different parts within the same component. The origin of the misfit could be mechanical, thermal, or transformation strains due to the changes in crystal structure [69]. In the following subsections, the influence of compressive and tensile residual stresses on fatigue behaviour will be described in more detail.

2.6.1 Compressive residual stress and its effect on the fatigue behaviour

The term compressive residual stress refers to a negative residual stress condition. Residual stress arises when the applied stress in the component is beyond its elastic limit and in the range where plastic yielding occurs. Engineers care about residual stress because it affects material performance. Compressive residual stress can resist the applied tensile stress as it holds the crack faces shut, minimizing fatigue damage [70]. To take advantage of this concept, many compressive residual stress surface treatments have been developed. For example, shot peening, laser shock peening, and cold expansion can be applied to introduce compressive residual stress at the surface and subsurface of the components, which can considerably improve fatigue service lifetime [71]. Figure 2.14 shows the compressive residual stress introduced at the surface and subsurface of the specimens using different shot peening technologies, such as Rounded Cut Wire Shot (RCW), bearing steel (SUJ2), and Tungsten Carbide Ball (WC), in comparison to a non-shot peened specimen (NP) [72].

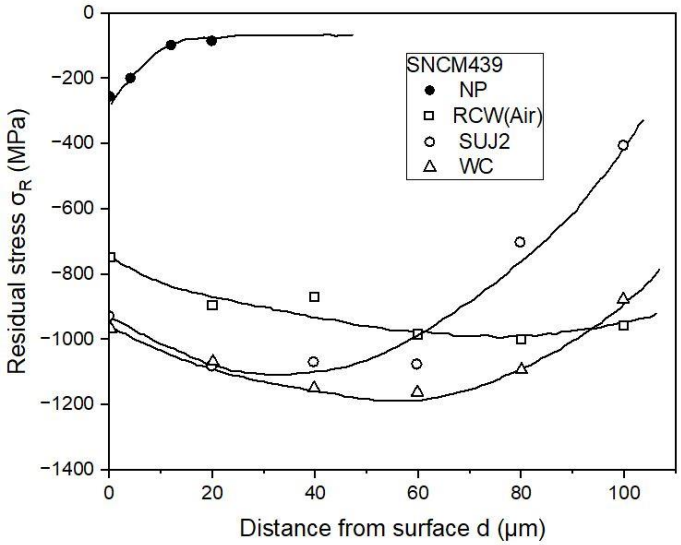

Figure 2.14 Compressive residual stress generated by different shot peening technologies [72].

The influence of the generated compressive residual stresses after shot peening on the fatigue lifetime and fatigue strength can be seen in Figure 2.15. All shot peening technologies presented here (SUJ2, RCW, and WC) lead to compressive residual stresses at the surface and subsurface, and subsequently, an enhancement in the fatigue strength and fatigue lifetime can be observed [72].

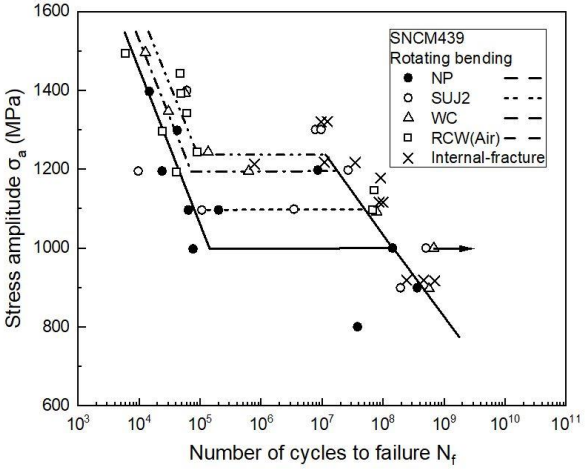

Figure 2.15 Influence of generated compressive residual after shot peening on the fatigue lifetime and fatigue strength [72].

2.6.2 Tensile residual stress and its effect on the fatigue behaviour

Tensile residual stresses can be often observed in the vicinity of weld defects like blowholes and slag inclusions or at the toes of fillet welds. On the contrary to compressive residual stresses, tensile residual stresses may promote fatigue crack propagation and hence lower fatigue lifetimes and also fatigue strengths. The reason for this is that tensile residual stresses can reduce these compressive stresses and increase the cyclic opening of the crack. That way, the crack opening displacement increases the crack growth

more in every cycle. Therefore, in order to estimate the lifetime, it is essential to analyse the influence of tensile residual stress on fatigue crack growth rate [73]. Records of fatigue crack closure in a tensile residual stress field indicate that the crack is completely opened in the entire loading range. However, in the absence of tensile residual stresses the crack is partially closed [74]. Figure 2.16 shows the fatigue crack growth behaviour of as-welded steel specimens under both tensile and compressive stress fields and compares the results with those for the base material. It can be seen that the fatigue crack growth rate of tensile residual stress specimens is higher than for the base metal and compressive residual stress specimens. Furthermore, the crack propagation threshold of an as-welded specimen is almost one-third of base metal [74].

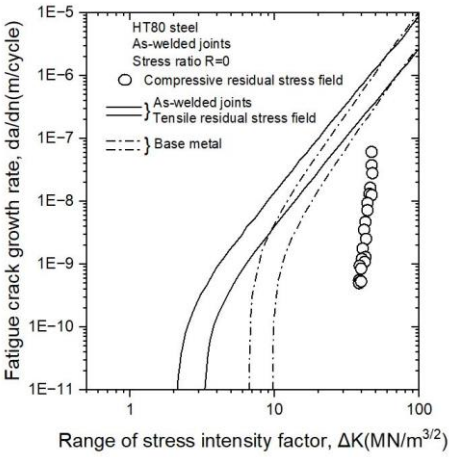

Figure 2.16 Influence of tensile and compressive residual stress fields on the fatigue crack growth rate [74].

2.6.3 Influence of treatments on the residual stress relaxations

Treatments such as thermal, mechanical, or combined thermo-mechanical treatments are widely used to improve the mechanical properties of metals. However, these treatments can generate residual stresses, which might not be desirable for fatigue strength. Thermal and mechanical energies can be considered as origins of residual stresses and have a significant impact on the generation of residual stresses. Both of them can convert the residual elastic strains to microplastic strains. As a result of supplying high amounts of thermal or mechanical energies, considerable residual stress relaxations can be found at the surface and subsurface of the components during thermal or thermomechanical treatments and each residual stress with thermal or mechanical origin has its own characteristics [25].

2.6.3.1 Influence of thermal treatment on the residual stress relaxation

Normally, thermal residual stress relaxation occurs during thermal treatments where inhomogeneous heating or cooling operations of the specimens lead to a loss of temperature balance between the core and surface of a material. These imbalances are due to the thermal gradient existence which causes the exceeding of the elasticity limit and even changes in the volume or length [75,76]. The most common thermal treatments are normalizing, annealing, quenching, and tempering. Thermal residual stress relaxation is highly influenced by the residual stress state itself and by the

material state. However, it has been reported for several types of steels that tempering can lead to a reduction in the compressive residual stress at both the surfaces and subsurfaces of the material [25,77]. For instance, the residual stress relaxation analyses after thermal treatments of quenched and tempered steel SAE4140 (42CrMo4) show that even after shot peening of the specimens, any further thermal treatments could reduce the compressive residual stress at the surface and subsurface [25].

2.6.3.2 Influence of mechanical treatment on the residual stress relaxation

Mechanical treatments such as straightening, stamping, shot peening, rolling and cyclic hardening are widely used for strengthening of metals. However, these mechanical treatments could lead to the generation of mechanical residual stresses in the body of the material [75].

- **Influence of cyclic loading treatment on the residual stress relaxation**

Cyclic loading has been used as a mechanical treatment process to improve the fatigue strength of high strength, and quenched and tempered steels [14]. Similar to thermal treatments, the analysis of residual stresses after cyclic loading of steel reveals a significant decrease in longitudinal and transverse residual stresses. Figures 2.17a and 2.17b represent the magnitudes of longitudinal residual stresses versus number of cycles at different cyclic stress amplitudes for quenched and tempered as well as normalized

steels. It can be seen that by increasing the cyclic stress amplitude the magnitude of residual stress is decreasing. It is noticeable that the first half cycle which is compressive, has a significant influence on the reduction of residual stress magnitudes. On the other hand, the second half cycle has either no influence on stress relaxation or the trend is reversed. Furthermore, a minimum stress amplitude is required to influence the magnitudes of residual stress during cycling. As can be seen from Figure 2.17a at the stress levels of 500 $\frac{N}{mm^2}$ and 600 $\frac{N}{mm^2}$, no more reduction in the residual stress magnitudes can be found, neither after the first cycle nor by increasing the number of cycles. Similar behaviour can be observed in Figure 2.17b at the stress levels ranging from 100 $\frac{N}{mm^2}$ to 300 $\frac{N}{mm^2}$. However, Figure 2.17a and 2.17b show that from above stress levels of 700 $\frac{N}{mm^2}$ and 400 $\frac{N}{mm^2}$, respectively, the residual stress magnitudes decrease considerably by increasing the number of cycles [25].

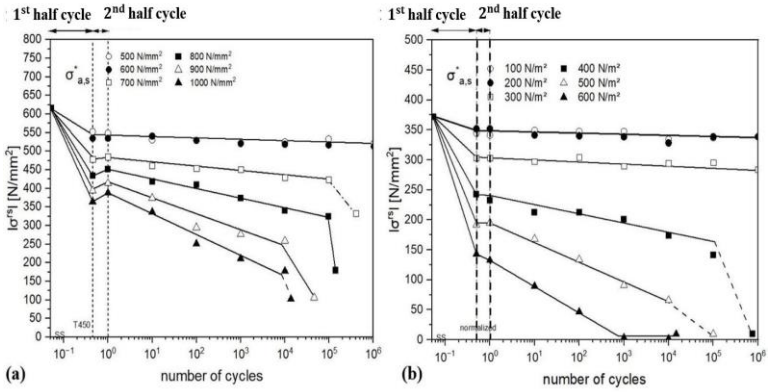

Figure 2.17 Effect of different cyclic loading amplitudes on the longitidunal residual stresses (a) quenched and tempered condition (b) the normalized condition [25].

2.6.3.3 Influence of cyclic loading at elevated temperature on the residual stresses

As discussed in subsection 2.5.3.1, TMT is one of the approaches to improve the fatigue strength of steels. However, a cyclic loading at elevated temperature could have a significant influence on the residual stresses. Figures 2.18a and 2.18b compare the magnitudes of residual stresses of quenched and tempered and normalized steels at different temperatures under constant stress loading of 800 $\frac{N}{mm^2}$ and 500 $\frac{N}{mm^2}$, respectively. It can be seen that in both, quenched and tempered and normalized steels by increasing the temperature from 25°C to 300°C and 400°C, the reduction in the magnitudes of residual stresses is getting more significant. Similar to Figure

2.17, the residual stress reduction in the first half cycle of Figure 2.18 is more remarkable than during the other cycles [25].

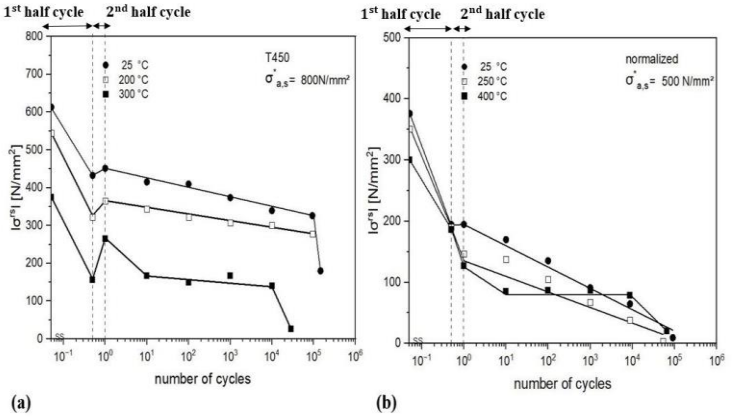

Figure 2.18 Effect of cyclic loading at elevated temperature on the magnitudes of longitudinal residual stresses for (a) quenched and tempered and (b) normalized [25]

This means that a thermomechanical treatment can also lead to a pronounced decrease in the magnitudes of residual stress at the surface of steels.

3 Specimen material and geometry

3.1 Specimen material

The investigated material was the low-alloy steel SAE4140 (German designation: 42CrMo4), which exhibits a high fatigue strength (712 MPa) after the quenching and tempering heat treatment and is therefore, often used for shafts and gears. The chemical composition of the test material is provided in Table 1 using spark spectrometry (OES).

Material	C	Si	Mn	P	S	Cr	Mo	Fe
wt (%)	0.43	0.259	0.743	0.012	0.039	1.06	0.207	Balance

Table 3.1 Chemical composition of the test material in wt.%.

The material was delivered in a soft-annealed state, in the form of round bars, from which a near-net-shape geometry of the specimens was machined by turning. These near-net-shape specimens were then heat-treated in a vacuum furnace (ALD Vacuum Technologies GmbH, Hanau, Germany). The heat treatment (HT) included austenitization at 840 °C for 20 min, followed by quenching in oil to reach room temperature, and tempering at 180 °C for 2 h. After the heat treatment, a fully martensitic microstructure was achieved, which shows a hardness of 594 $\pm$5 HV 0.5 (see subsection 6.4) with a 0.2% yield strength of 1500 MPa and an ultimate tensile strength of 1900 MPa [78].

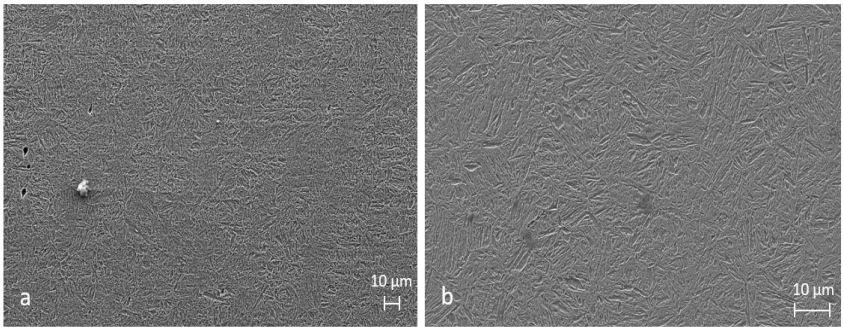

Figure 3.1 Microstructure evaluation of SAE4140 (a) before heat treatment (b) after quenching and tempering.

Figure 3.1a shows the microstructure of SAE4140 before quenching and tempering in a soft-annealed state. After the heat treatment, a fully martensitic microstructure was obtained which is shown in Figure 3.1b. The formation of lath martensites in the microstructure after heat treatment can be observed in Figure 3.1b.

3.2 Specimen geometry

After the quenching and tempering, the final specimen geometry was machined by turning. The critically stressed volume of the specimen was designed with a cylindrical gage length of 5 mm and a gauge length diameter of 4 mm which can be seen in Figure 3.2.

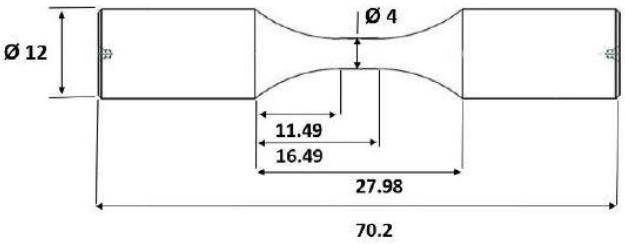

Figure 3.2 Specimen geometry used for the experiments (all dimensions in mm)

4 Testing setups and experimental procedures

4.1 Furnace for the heat treatment

A vacuum furnace (ALD Vacuum Technologies GmbH, Hanau, Germany) was used for the heat treatment of the specimens.

4.2 Servohydraulic testing machine

All fatigue tests as well as the treatments were conducted on a servo-hydraulic push-pull-testing machine (Instron GmbH, Darmstadt, Germany) with a capacity of 100 kN. A transducer (Interface Inc., Scottsdale, AZ, USA) was used to measure the force. The specimens were cycled under stress control with a sinusoidal waveform and a load ratio of R = -1 until failure or until the ultimate number of cycles $N_u = 10^7$ was reached. For fatigue tests in the LCF and HCF regime, a frequency of 50 Hz was applied, and the ultimate number of cycles was $N_u = 10^7$. During the heating of the TMT and TT specimens, an induction generator (Hüttinger, Freiburg, Germany) along with a coil were used, which were carefully adjusted to ensure a homogeneous temperature distribution within the gauge length. The temperature during the treatment was measured with type K thermocouples applied at the center, top, and bottom of the gauge length. An ex-

tensometer was used to measure the elongation of the specimens in the experiments and that was applied outside of the specimen's gauge length using alumina rods. The schematic design of the servohydraulic testing machine can be seen in Figure 4.1.

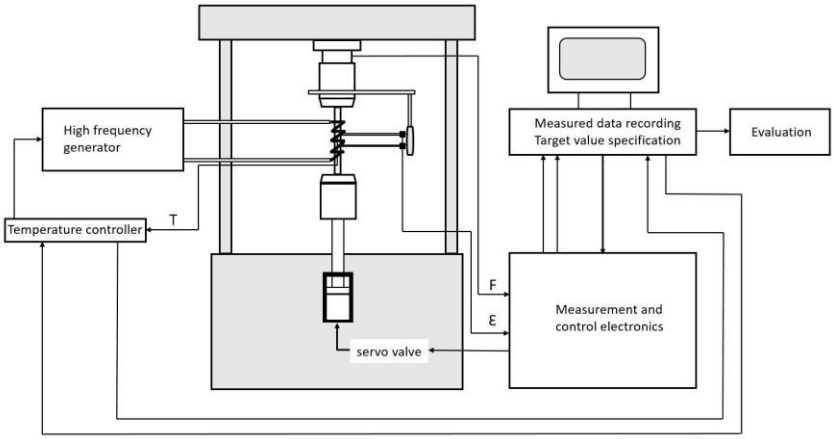

Figure 4.1 The schematic design of servohydraulic testing machine.

4.3 Applying the staircase method for the estimation of mean fatigue strength stress

The staircase test method is used to estimate accurate values of the mean fatigue strength stress up to 10^7 cycles. If the specimen fails before reaching 10^7 cycles, then it is considered a failure; otherwise, it is considered a run out specimen. An estimation is used for the stress amplitude of the first specimen. The stress amplitude of subsequent fatigue tests depends on the

test result of a specimen (failure or run out). If the test could reach 10^7 cycles without failure, then the next specimen is tested at the next higher stress amplitude. However, if the test failed before reaching 10^7 cycles, then the subsequent fatigue test is performed at the next-lower stress stress amplitude [79,80], as shown in Fig. 4.2.

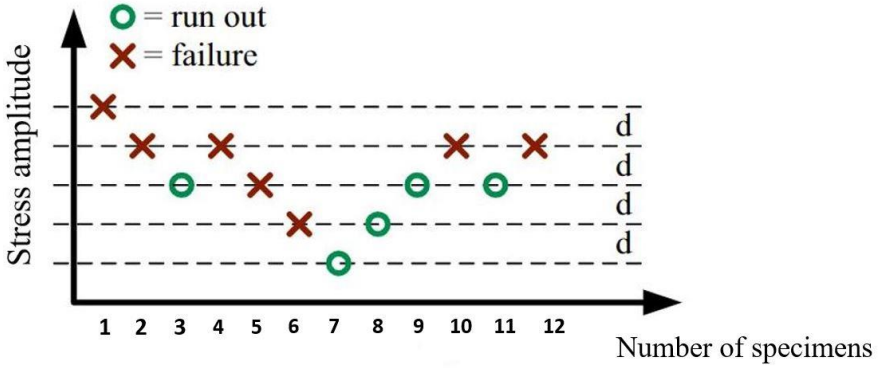

Figure 4.2 The staircase method principal [79].

To obtain the endurance limit of each treatment, the staircase method was applied using 12 specimens.

4.4 Specimen preparation for microstructural and hardness analysis

The specimens intended for microstructural and hardness analysis were cold mounted in methyl-methacrylate resin (VariKEM 200 by Schmitz

Metallographie, Germany) and stepwise ground and polished semi-automatically. The polishing steps were conducted at 15 N/specimen for a duration of 10 min by using diamond suspensions of 3 and 1 µm particle size, respectively. For microstructural analysis, the polished specimens were etched with Nital.

4.5 Hardness measurement

Hardness values on longitudinal and gradient subsections were measured using a Vickers-type microhardness tester Qness Q10 A+ (Qness GmbH, Salzburg, Austria) with an indentation load of 0.5 kg (HV 0.5).

4.6 Scanning electron microscope (SEM)

The fracture surfaces of specimens were analysed using an SEM EVO 50 (Carl Zeiss AG, Oberkochen, Germany). Secondary Electron Imaging (SEI) was used to measure the size of inclusions and the size of fisheyes, which are surrounding the inclusions. For the fracture surface analysis, the specimens were mounted on the SEM stub using carbon taper and conductive silver paste.

4.7 Energy Dispersive X-Ray spectroscopy Analysis (EDS)

To determine the chemical composition of the non-metallic inclusions on the fracture surfaces, an EDS detector (Thermo Fisher Scientific Inc., Waltham, MA, USA) mounted to the SEM was used.

4.8 Optical microscopy

Optical microscopy is carried out by using the Aristomet optical microscope from the Leitz company. The microscope has an objective turret with different lenses for 50x, 100x, 200x, 500x, and 1000x magnification.

4.9 X-Ray Diffraction (XRD)

The residual stress analyses were carried out on a ψ-diffractometer [81] with V-filtered CrKα radiation by use of the $\sin^2\psi$-method [82]. On the primary beam side, a focusing polycapillary X-ray optics with a nominal diameter of 100 µm and on the secondary side a 4 mm symmetrizing slit [83] was used. In the analysis, the surface parallel residual stresses in the axial and tangential direction in the center position were determined. Therefore, the {211} diffraction peak positions of α-Fe ($2\theta_0$ = 156.394°) were analysed at 15 ψ-angles in the range of ±60° (equidistant in $\sin^2\psi$). For the residual stress calculation, the elastic constants $E_{\{211\}}$ = 220 GPa and $\nu_{\{211\}}$

= 0.28 [84] were used. To determine the residual stress depth profile, subsequent electrochemical layer removal steps by the use of a LectroPol-5 device (Struers GmbH, Willich, Germany) were combined with residual stress analyses. The specimen's surface layer was removed using the electropolishing method. Electropolishing was chosen to ensure that no residual stress was introduced into the specimens during the layer removal process [85].

4.10 Shot-peening

The shot peening process was carried out with a shot peening machine (Baiker AG Strahlverfahrenstechnik, Germany) and a conventional air peening device using spherical high carbon steel balls (S110) with a hardness of 46 HRC (Rockwell hardness value [86]) and a diameter of 0.3 mm. The applied air pressure was 2 bar, flow rate 1.2 kg/min, nozzle distance 100 mm, nozzle diameter 8 mm, and moving speed of 1000 mm/s.

5 Additional treatments

In order to characterize the fatigue behaviour of TMT specimens, after the classical heat treatment (HT) of the specimens, which has been described in Chapter 3, additional thermomechanical treatments (TMT) have been conducted in the temperature regime of DSA to reveal the influence of TMT on the fatigue strength of 42CrMo4 steel. In this study, the HT specimens serve as a reference for the other treatments. Furthermore, MT and TT treatments were solely applied to investigate the effects of thermal and mechanical loading also individually.

5.1 Thermomechanical treatment (TMT)

The TMT was applied in the critically stressed volume in the cylindrical gauge length of the specimens with a length of 5 mm.

5.1.1 Process of finding the temperature of maximum DSA

The first step to conduct a TMT in the temperature regime of DSA is to find a suitable temperature in which DSA occurs to the maximum extent. The temperature of maximum DSA is assumed to be the temperature at which maximum cyclic hardening occurs [13]. Uniaxial cyclic tests were carried

out using stress-controlled loading conditions to investigate the cyclic hardening and softening effects of the specimens. The extent of cyclic hardening is defined as the reduction in plastic strain amplitude within the stress-controlled stress-strain hysteresis loop. Since at this temperature, the dislocation hardening is at its highest. Therefore, the process of finding the temperature of maximum DSA is based on the plastic strain amplitude measurements at the temperature of the DSA range [13,14]. In order to find the temperature of maximum DSA, the specimens were cycled for 20 cycles with a sinusoidal waveform at a constant stress amplitude (σ_a) of 1500 MPa and a frequency of 1 Hz at different temperatures ranging from 260 °C to 290 °C. An induction coil was used during the heating of the TMT, which was carefully adjusted to ensure a homogeneous temperature distribution within the gauge length. In Figure 5.1, a schematic diagram of the courses of temperature and stress to find the temperature of maximum DSA is shown.

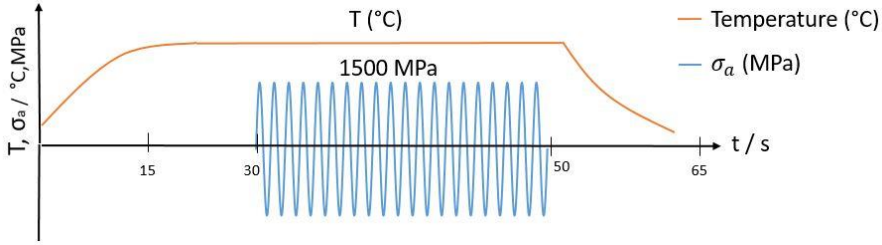

Figure 5.1 Schematic illustration of the process to find the temperature of maximum DSA.

The extensometer with a gauge section of 30 mm was applied outside of the specimen's gauge length using alumina rods. With the measured elongation of the specimen, the actual strain within the cylindrical gauge length cannot be determined since the radii towards the specimen's shoulders are within the measuring length. However, with the applied setup, a qualitative strain in the measuring length of the extensometer can be determined, which is, in turn, used to achieve Stress–Strain hysteresis loops and a qualitative plastic strain amplitude $\varepsilon_{(a,p,quali)}$. It is assumed that the cyclic hardening behaviour of the gauge length can be described with this qualitative plastic strain amplitude.

5.1.2 TMT process at the temperature of maximum DSA

The next step after finding the best temperature for the maximum DSA was to find a suitable mechanical load for the thermomechanical treatment. Since the highest stabilisation influence of the dislocation structure during the DSA process might be around the non-metallic inclusions, a stepwise increasing stress amplitude is chosen to have the maximum strengthening effects around the inclusions [14,66]. Applying increasing stress amplitudes with a sinusoidal waveform at a frequency of 1 Hz by equidistant steps of 100 MPa, 5 cycles at each step until maximum load level showing cyclic hardening which can be determined by the extensometer. The minimum and maximum stress amplitudes of TMT were defined as the lowest

and the highest stress amplitudes, which contribute to continuous cyclic hardening, thus displaying decreasing plastic strain amplitudes within the five cycles of the loading step [13]. The TMT was performed in the critically stressed volume in the cylindrical gage length of the specimens with a length of 5 mm. Figure 5.2 represents the schematic illustration of TMT.

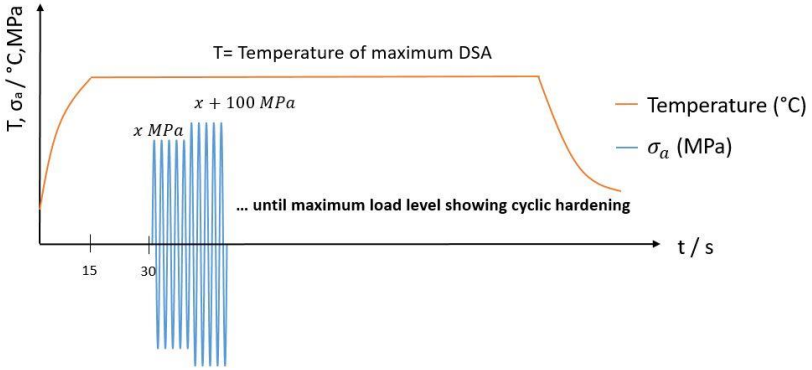

Figure 5.2 Schematic illustration of TMT in the temperature of maximum DSA.

5.2 Thermal treatment (TT)

The thermal treatment (TT) was conducted at the temperature of maximum DSA, which corresponds to the temperature of TMT. The heating duration of the TT specimen is the same as the TMT one. However, no mechanical load was applied for this treatment. A schematic illustration of the TT is shown in Figure 5.3.

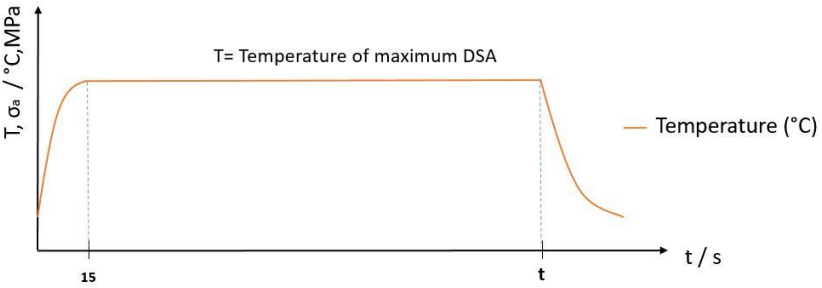

Figure 5.3 Schematic illustration of TT in the temperature of maximum DSA.

5.3 Mechanical treatment (MT)

The MT was conducted at room temperature. The mechanical load during MT corresponds to the mechanical load of TMT treatment. The schematic illustration of MT can be seen in Figure 5.4.

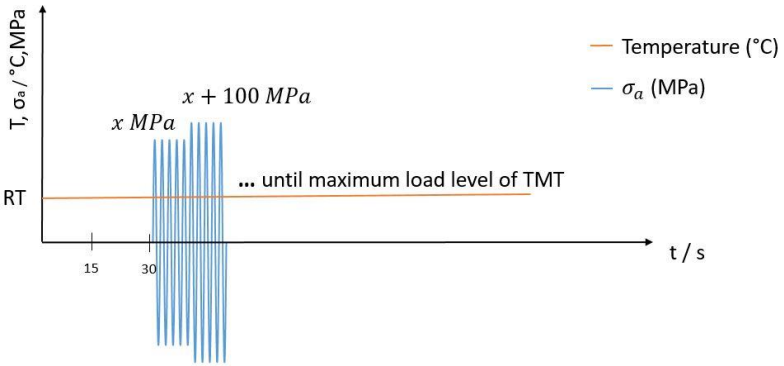

Figure 5.4 Schematic illustration of MT at room temperature.

6 Results

Part of the research results presented in this chapter have already been published in the following two-scientific journal articles. However, the published paper mentioned below have not been cited as references in this dissertation.

- Khayatzadeh, A.; Sippel, J.; Guth, S.; Lang, K.-H.; Kerscher, E. Infl ence of a Thermo-Mechanical Treatment on the Fatigue Lifetime and Crack Initiation Behavior of a Quenched and Tempered Steel. *Metals* **2022**, *12*, 204, doi:10.3390/met12020204.

Conceptualization, Lang, K.-H. and Kerscher, E.; investigation, Khayatzadeh, A. and Sippel, J.; writing-original draft preparation, Khayatzadeh, A. and Sippel, J.; writing-review and editing, Guth, S. and Lang, K.-H.; visualization, Khayatzadeh, A. and Sippel, J.; supervision, Guth, S. and Kerscher, E.; funding acquisition, Lang, K.-H. and Kerscher, E.

- Khayatzadeh, A.; Guth, S.; Heilmaier, M. Comparison of the Internal Fatigue Crack Initiation and Propagation Behavior of a Quenched and Tempered Steel with and without a Thermomechanical Treatment. *Metals* **2022**, *12*, 995, doi:10.3390/met12060995.

Conceptualization, Khayatzadeh, A. and Guth, S.; investigation, Khayatzadeh, A.; original draft preparation, Khayatzadeh, A.; writing-review and editing, Guth, S. and Heilmaier, M.; supervision, Heilmaier, M.

All authors have read and agreed to the published version of the manuscript.

6.1 Thermomechanical treatment (TMT)

It is assumed in Chapter 5 that a TMT is conducted at the temperature of maximum DSA. Therefore, first, it is essential to find the temperature of maximum DSA and after that, a suitable increasing mechanical load should be applied at this temperature in order to increase the fatigue strength and properties of the steel.

6.1.1 Finding the temperature of maximum DSA

It has been indicated in subsection 5.1.1 that in order to find the temperature of maximum DSA, the specimens were cycled at constant stress level for different temperatures. Figure 6.1 shows the cyclic hardening behaviour of the material at different temperatures for a stress amplitude of 1500 MPa and a loading frequency of 1 Hz. Cyclic hardening extent, as defined in subsection 2.4, was analysed using the ratio of the qualitative plastic strain amplitude in the first and 20th cycles. It can be observed that at all temperatures the reduction in the qualitative plastic strain amplitude (cyclic hardening) takes place and for each tested temperature the highest cyclic hardening occurs between the first and the second cycle and after that by increasing the number of cycles, the cyclic hardening effect reduces considerably. The highest extent of cyclic hardening, and, thus, the maximum of this ratio was found at 265 °C, which is interpreted as the temperature of the maximum DSA for the applied testing frequency of 1 Hz.

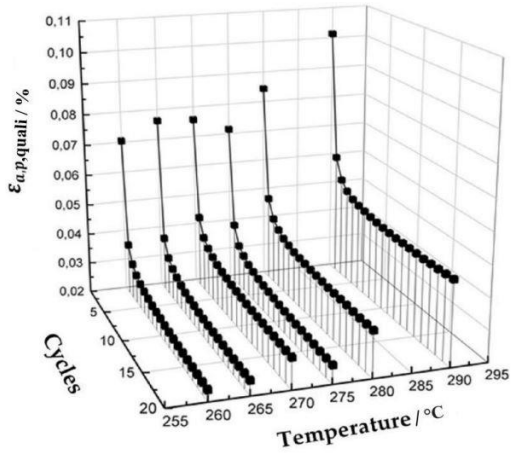

Figure 6.1 Analysis of the qualitative plastic strain amplitude $\varepsilon_{(a,p,quali)}$ at a constant stress level of 1500 MPa and at 1 Hz for different temperatures.

6.1.2 Finding a suitable mechanical load for TMT

To achieve an optimal strengthening effect at the temperature of maximum DSA, a suitable range for the stress amplitudes needs to be applied. As it is shown in subsection 5.1.2, in order to strengthen the microstructure of the specimens gradually, increasing load amplitudes were applied. The minimum selected stress amplitude was 600 MPa, Since for lower stress amplitudes, the plastic strain amplitude (determined by calculating the half-width of a closed hysteresis loop) was negligible. Figure 6.2 shows plastic strain amplitude decreases from 600 MPa to 1600 MPa. However, at 1700 MPa a cyclic softening occurred (cyclic softening is defined in subsection 2.4).

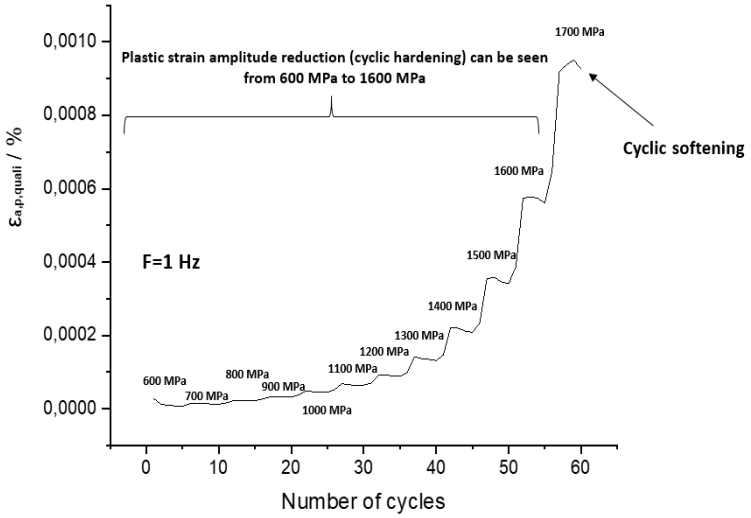

Figure 6.2 Plastic strain amplitude for increasing stress amplitudes from 600 MPa to 1700 MPa at 265°C.

6.1.3 Process of TMT after finding the suitable temperature and mechanical loads

After obtaining the suitable temperature and mechanical loads for the TMT and according to the TMT process which is described in subsection 5.1.2, the specimens were heated inductively to 265 °C at zero stress and were kept in this state for 15 s soaking time. Three thermoelements were used at the center, top, and bottom of the specimens during the soaking time to measure temperature and ensure a homogeneous temperature distribution

around the 5 mm gauge length. Then the sinusoidal cyclic mechanical treatment of the TMT was applied with a gradually increasing stress amplitude from 600 MPa to 1600 MPa. The total treatment duration was 70 s. Figure 6.3 shows the schematic illustration of the TMT process.

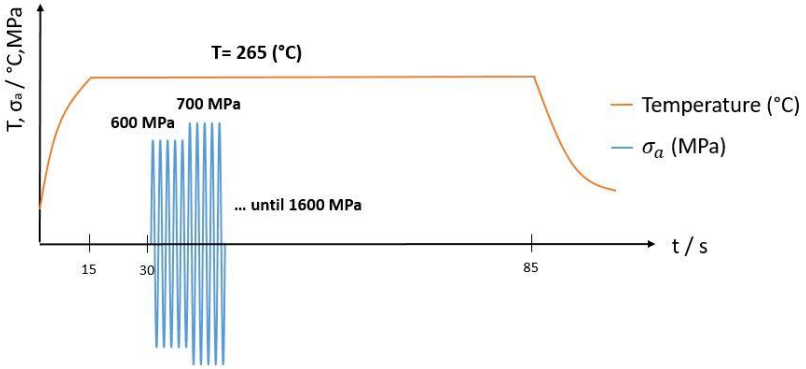

Figure 6.3 Complete schematic illustration of the TMT process after finding the temperature of maximum DSA and suitable mechanical loads.

6.1.4 Process of increasing the soaking time of TMT

An important consideration is whether a soaking time of 15 seconds is sufficient for the TMT process and after this duration, all parts of the gauge length have reached a homogeneous temperature of 265°C. Therefore, the soaking time was increased from 15 s to 300 s to see its effect on the fatigue lifetime, as shown in Figure 6.4.

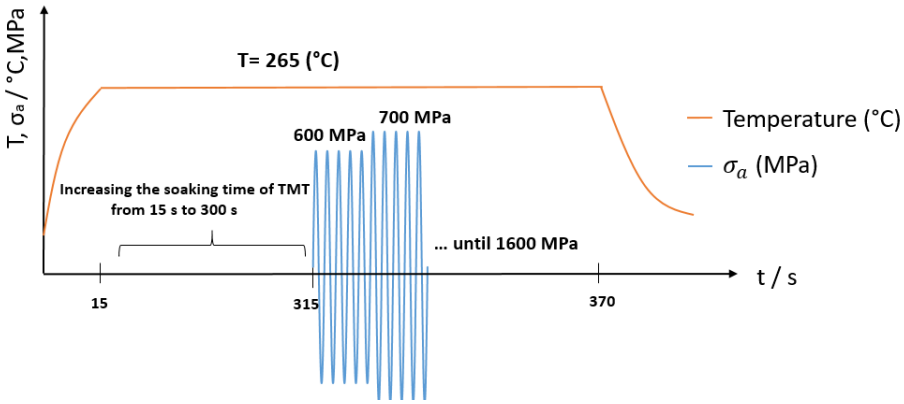

Figure 6.4 Complete schematic illustration of increasing the soaking time during TMT process.

6.2 Thermal treatment (TT)

In subsection 5.2 is described that TT corresponds to the temperature of TMT with the same treatment time period at a load-free condition without any mechanical treatment. Since from subsection 6.1.1, the maximum hardening effect and the optimal temperature for TMT was found at 265 °C, thus, TT was conducted at 265 °C for 70 s. Figure 6.5 represents the schematic illustration of TT.

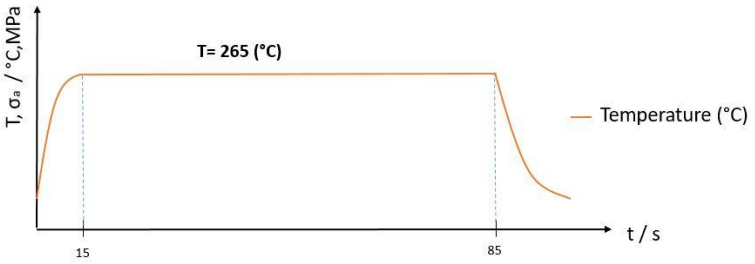

Figure 6.5 Complete schematic illustration of TT.

6.3 Mechanical treatment (MT)

According to subsection 5.3, and since the cyclic hardening effect during TMT occurs in the stepwise increasing stress amplitudes from 600 MPa to 1600 MPa (see subsection 6.1.2), thus, MT was conducted at room temperature and following stress amplitudes which is shown in Figure 6.6.

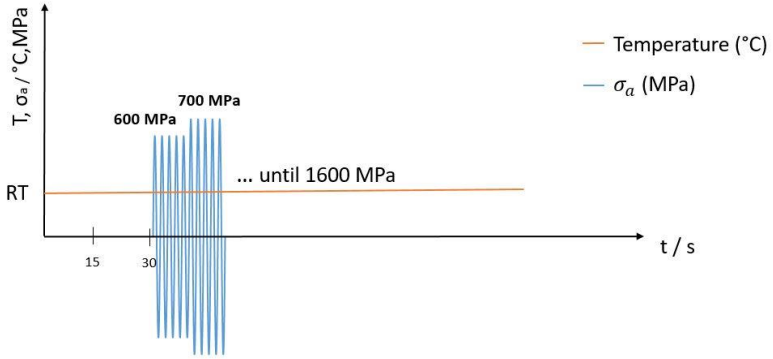

Figure 6.6 Complete schematic illustration of MT.

6.4 Hardness analysis of TT, MT, TMT and HT specimens

The hardness was measured on longitudinal subsections of HT, TMT, MT, and TT-treated specimens with a hardness profile along the specimen axis, which is shown in Figure 6.7a. The hardness was measured with 0.5 kg mass at the indenter at 20 equidistant positions with 0.5 mm distance between indentations. Figure 6.7b exhibits the longitudinal hardness values of HT, TMT, MT, and TT-treated specimens. The positions 5 to 15 correspond to the gauge length of specimens, in which the treatments were applied. For positions 5 to 15, the average hardness of the HT specimen is 594 ± 5 HV 0.5. For the same positions, the average hardness of the TT specimen is 568 ± 4 HV 0.5, which is significantly lower than for the other specimens. However, it can be observed that even outside of the gauge length, the hardness has decreased due to the TT when compared to other treatments. The hardness behaviour of HT and TMT specimens is almost similar. For the MT specimen, a minor hardness increase in the gauge length can be seen.

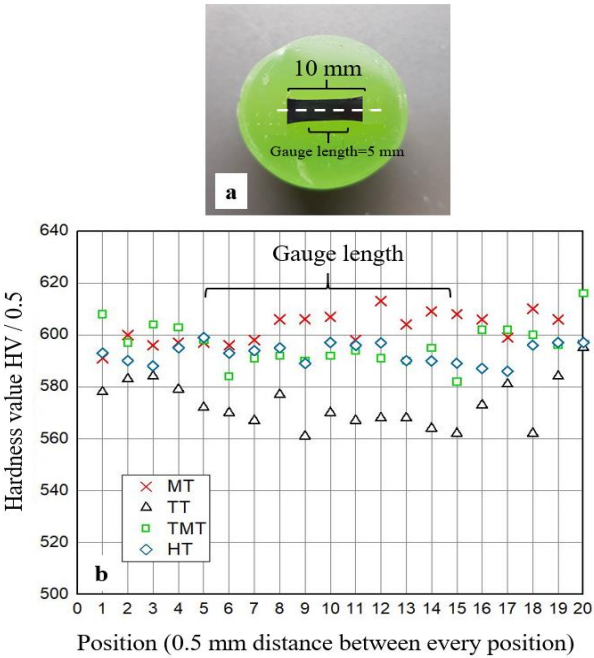

Figure 6.7 (a) A mounted specimen (b) Influence of different treatments on the specimen hardness.

6.5 Fatigue crack initiation sites

As described in subsections 2.2.1 and 2.2.2, the initiation of the crack can be from the surface or inside the volume of the specimen. The fatigue fracture surface analyses of HT, MT, TMT, and TT specimens show that the crack initiation in all the specimens with $N_f \geq 7 \times 10^5$ cycles originates from non-metallic inclusions inside the volume, which are surrounded by

fisheyes. On the other hand, for $N_f < 7 \times 10^5$ cycles, the crack initiates at the surface or subsurface of the specimens. Figure 6.8 shows the representative crack initiation positions at the surface (Figure 6.8a) and internal non-metallic inclusion surrounded by a fisheye (Figure 6.8b). The qualitative appearance of the crack initiation sites was comparable for all 4 categories of TMT, HT, TT, and MT specimens.

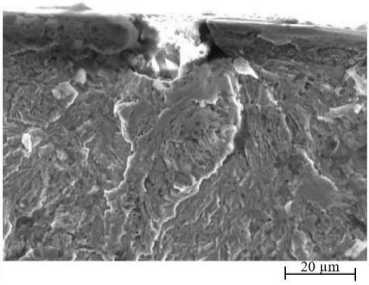

(a) HT σ_a = 900 MPa, N_f = 175,162 cycles

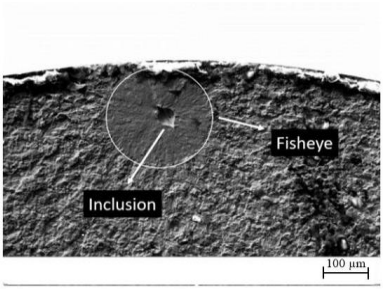

(b) with TMT σ_a = 775 MPa, N_f = 4,932,070 cycles

Figure 6.8 SEM images of two fracture surfaces: (a) crack initiation at a surface groove without any fisheye formation; (b) crack initiation at a critical inclusion inside the volume as well as the fisheye formation.

The fatigue fracture analysis indicates that the crack initiation site is independent of the applied treatment and mainly depends on the fatigue lifetime and applied stress amplitudes.

6.6 Fatigue behaviour of TMT, TT, MT and HT specimens

Fatigue behaviour analyses of TMT, TT, MT, and HT specimens show a significant difference between $N_f \geq 7 \times 10^5$ cycles, and $N_f < 7 \times 10^5$ cycles. The main difference in the fatigue behaviour is due to the crack initiation site, which is described in detail in subsection 6.5. Since the effect of treatments (TT, HT, MT, TMT) on crack initiation and fatigue behaviour is significantly different between the surface and internal conditions, it is essential to analyse the fatigue behaviour in two different fatigue lifetime regimes.

6.6.1 Fatigue behaviour of TMT, TT, MT and HT specimens for lifetimes longer than 7×10^5 cycles ($N_f \geq 7 \times 10^5$ cycles)

In this investigation, all the treated specimens with lifetimes $N_f \geq 7 \times 10^5$ are considered and their fatigue behaviours were analysed and compared with the HT specimen as a reference specimen. To obtain the endurance limit of each treatment, the staircase method was applied using 12 specimens which is shown in Figure 6.9.

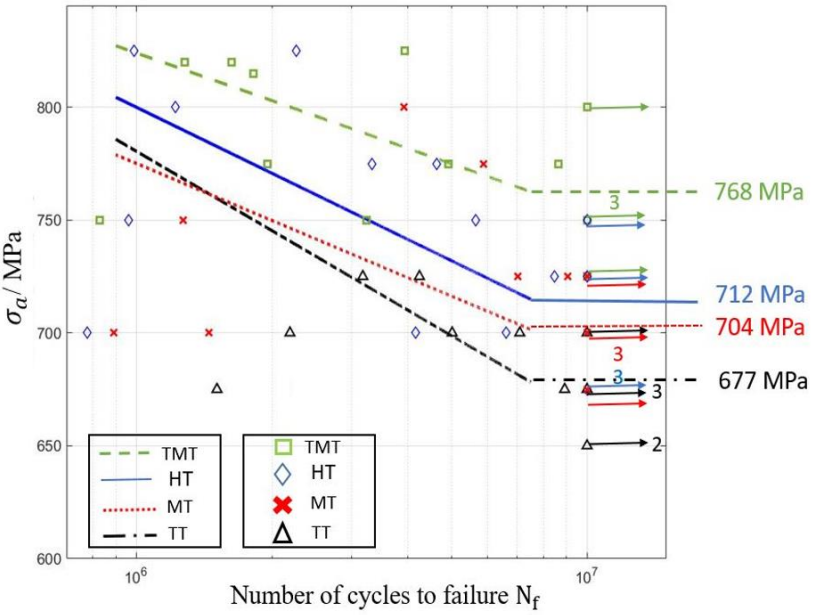

Figure 6.9 S–N curve for specimens with the TMT, TT, MT, and HT for $N_f \geq 7 \times 10^5$ cycles. The number of run-out specimens that reached $N_u = 10^7$ cycles without failure at a given stress amplitude is identified by the number beside the representative data point.

6.6.1.1 Fatigue behaviour comparison between HT and TMT specimens ($N_f \geq 7 \times 10^5$)

From Figure 6.9, the S–N curve of the TMT-treated and the reference HT specimens tested on the servo-hydraulic testing setup for $N_f \geq 7 \times 10^5$ cycles can be observed. For $N_f \geq 7 \times 10^5$ cycles, TMT-treated specimens show higher lifetimes and better fatigue behaviour than HT specimens, the endurance limit comparison reveals an improvement from 712 MPa to 768

MPa after TMT which means an 8% increase. Figure 6.9 proves the positive effect of a TMT in the temperature of DSA on fatigue strength.

- **Influence of TMT on the maximum stress intensity factor of critical inclusion ($K_{max,Inc}$)**

In order to determine the maximum stress intensity factor of critical inclusions, it was essential to measure the area of these critical inclusions (see Figure 6.10a). Subsequently, equation (3) in subsection 2.3.1 was used with the measured area of the crack-initiating inclusions to determine the maximum stress intensity factor for internal inclusions (see Figure 6.10b). As can be seen from Figure 6.10a, except for two large TMT inclusions (47 µm and 49 µm), the other inclusions for both TMT and HT specimens are in similar sizes, ranging from 22 µm to 36 µm. However, the minimum inclusion sizes with the size of 22 µm and 25 µm belong to the TMT specimen. In Figure 6.10b, the maximum stress intensity factor of the non-metallic inclusions ($K_{max,Inc}$) in the HCF regime for both the TMT and HT specimens is plotted over the fatigue lifetime. It is visible that for comparable inclusion areas and lifetimes, the values of $K_{max,Inc}$ are higher for the TMT specimens than for the reference HT specimens (as indicated by the numbers from 1 to 4 in Figure 6.10b) and almost no degradation in the other $K_{max,Inc}$ values for TMT specimens is observable when compared to those of HT specimens. Even the $K_{max,Inc}$ of minimum inclusion areas of TMT

specimens exhibit an increase and do not represent the lowest $K_{max,Inc}$ (numbers 2 and 3).

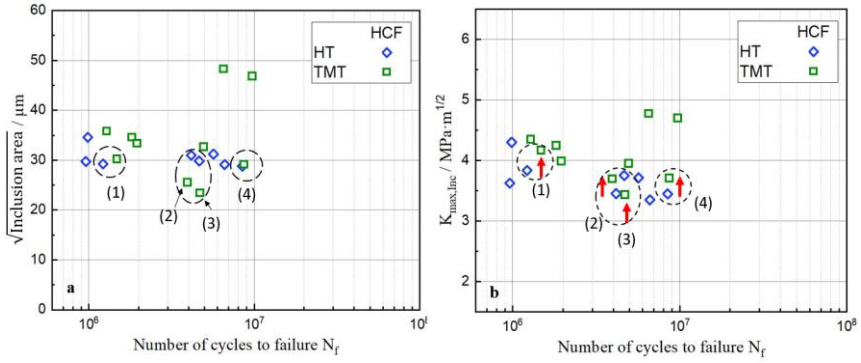

Figure 6.10 (a) Measured area of the crack-initiating inclusions versus a lifetime; (b) Maximum stress intensity factors $K_{max,Inc}$ at internal critical non-metallic inclusions versus a lifetime.

The majority of the TMT specimens exhibit a $K_{max,Inc}$ value that is equal to or higher than 3.9 MPa.m$^{1/2}$. In contrast, among the HT specimens, only one shows a $K_{max,Inc}$ exceeding 4 MPa.m$^{1/2}$, while the rest of the HT specimens have $K_{max,Inc}$ values below 4 MPa.m$^{1/2}$.

TMT and HT specimens originate from identical batches, ensuring that the area of critical inclusions are almost within the same ranges. However, TT and MT specimens belong to different batches, showing considerably different inclusion areas. Therefore, comparing the K_{max} values of TT and MT specimens with those of TMT and HT specimens is not reasonable.

6.6.1.2 Fatigue behaviour comparison between HT and TT specimens ($N_f \geq 7 \times 10^5$ cycles)

Figure 6.9 compares also the fatigue behaviour of TT and HT as reference specimens for $N_f \geq 7 \times 10^5$ cycles. It can be seen that after TT, the fatigue strength has decreased by 35 MPa.

6.6.1.3 Fatigue behaviour comparison between HT and MT specimens ($N_f \geq 7 \times 10^5$ cycles)

Figure 6.9 shows that for $N_f \geq 7 \times 10^5$ cycles and after an MT, no remarkable influence in the fatigue behaviour can be observed and the fatigue behaviour is similar to HT specimens. The endurance limit after an MT is 704 MPa, which means only a minor difference compared to the endurance limit of HT specimens (712 MPa).

6.6.2 Fatigue behaviour of TMT, TT, MT, and HT specimens for lifetimes shorter than 7×10^5 cycles ($N_f < 7 \times 10^5$ cycles)

For $N_f < 7 \times 10^5$ cycles, in which the crack initiates at the surface or subsurface, the results of the treated specimens show completely different behaviour from $N_f \geq 7 \times 10^5$ cycles. By considering the fatigue behaviour of different treated specimens in this regime (shown in Fig 6.11), 4 to 5 specimens for each treatment in this regime at different stress amplitudes were tested and observed that in all cases TMT and MT specimens have

remarkably shorter lifetimes than HT and TT specimens. For instance, it can be observed that at σ_a=1000 MPa TMT and MT specimens show almost half of the lifetimes of HT and TT specimens. Similarly, for other stress amplitudes such as 950 MPa, 925 MPa, and 900 MPa also the negative influence of TMT and MT on the lifetimes of the specimens is observable. In other words, contrary to $N_f \geq 7 \times 10^5$ cycles, the fatigue behaviour of TMT and MT specimens for $N_f < 7 \times 10^5$ cycles not only shows an increase in the fatigue lifetimes but also appears a remarkable decrease in the lifetimes of fatigue experiments. In all 5 different stress amplitudes which is shown in Figure 6.11, the lifetime of TMT and/or MT specimens is shorter than HT and TT specimens.

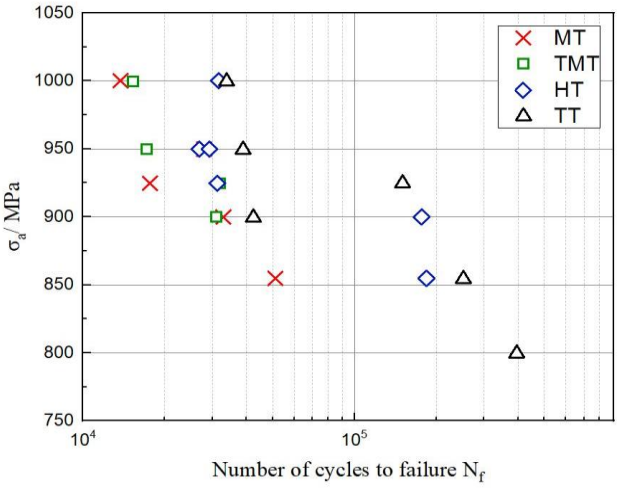

Figure 6.11 S–N curve for specimens with different treatments for the lifetimes shorter than 7×10^5 cycles ($N_f < 7 \times 10^5$ cycles).

6.7 Residual stress analysis

Fig 6.12 compares the residual stresses at the surface and subsurface of specimens with different treatments. A significant residual stress difference can be seen between the surface and subsurface of HT and TT specimens, as well as MT and TMT specimens. The surface and subsurface of the HT and TT specimens are surrounded by compressive residual stress. However, for TMT specimens, tensile residual stresses are present at the surface and subsurface. Furthermore, after MT a considerable reduction of compressive residual stress at the surface and subsurface is observable.

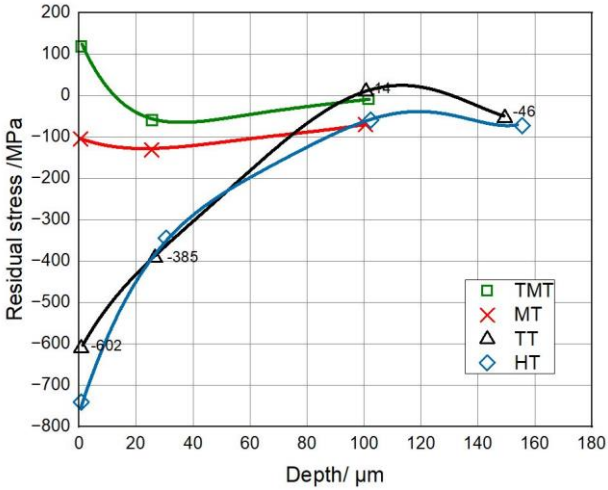

Figure 6.12 Axial residual stress analysis at surface and subsurface of specimens with different treatments.

The highest amount of compressive residual stress at the surface of the specimen belongs to the HT specimen (around -750MPa).

6.8 Influence of shot peening on the residual stress distribution, hardness, and lifetime of TMT specimens

The MT and TT specimens do not exhibit any enhancement in the fatigue lifetime and fatigue strength for $N_f \geq 7 \times 10^5$ cycles. Therefore, the shot peening was conducted only for TMT specimens to regenerate again the compressive residual stresses at the surface and subsurface, with the goal of increasing the fatigue lifetime of TMT specimens for $N_f < 7 \times 10^5$ cycles where no strengthening effect of DSA is observable and achieving improved fatigue behaviour of TMT specimens for both LCF and HCF regimes.

6.8.1 Influence of shot peening on the residual stress distribution

In the subsection 2.6.1 is described that one of the methods to introduce compressive residual stress is using shot peening. As it is specified in subsection 4.10, shot peening was conducted to reintroduce the compressive residual stress at the surface and subsurface of the TMT specimen. Figure 6.13 presents a considerable reintroduction of compressive residual stress

on the surface and subsurface after the shot peening of the TMT specimen (named TMT-shot peened). The generation of compressive residual stress after shot peening is even more pronounced than in HT and TT specimens. At a depth of 100 µm, the difference in compressive residual stress of the TMT specimen induced by shot peening and other specimens (TMT, HT, TT, and MT) is approximately 600 MPa to 700 MPa.

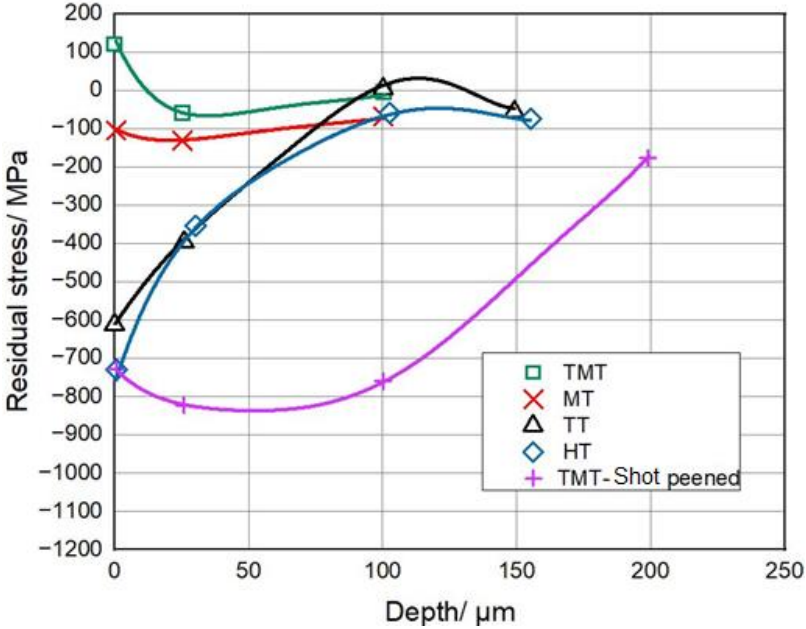

Figure 6.13 Influence of shot peening on the residual stress distribution near the surface of TMT specimen.

6.8.2 Influence of shot peening on the hardness values at the surface and subsurface of a TMT specimen

The hardness analysis at the gauge length of the TMT-shot peened specimen was conducted to investigate on the effect of shot peening on the hardness values at the surface and subsurface of a TMT specimen. Figure 6.14 shows the gradient hardness profile versus depth from the surface and subsurface after shot peening. It is observable that shot peening was able to increase the hardness at the surface and subsurface of a TMT specimen by almost 25 HV until the depth of 60 µm below the surface. The hardness values deeper than 60 µm reveal a significant hardness reduction.

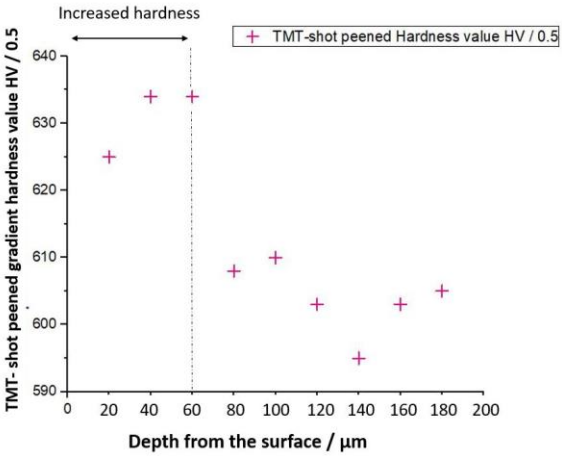

Figure 6.14 Influence of shot peening on the hardness values at the surface and subsurface of a TMT specimen.

6.8.3 Influence of shot peening on the lifetime of TMT specimen

After the shot peening of TMT specimens and reintroducing of compressive residual stresses at the surface and subsurface of the specimens, the TMT-shot peened specimens were cycled in two different regimes, depending on the crack initiation position to see the influence of the newly introduced compressive residual stresses on the fatigue behaviour and lifetime. Figure 6.15 shows the fatigue lifetime of TMT specimens before and after shot peening as well as the fatigue behaviour of HT specimens as a reference for $N_f < 7 \times 10^5$ cycles, in which cracks initiate typically from the surface and subsurface of specimens. It is visible that for all 4 given stress amplitudes of 1000 MPa, 950 MPa, 925 MPa, and 900 MPa remarkable increases in the lifetimes of TMT specimens after shot peening can be obtained. It is also observable that the improvement of fatigue lifetimes after shot peening at the stress amplitudes of 925 MPa and 900 MPa is much more significant than for the stress amplitudes of 1000 MPa and 950 MPa.

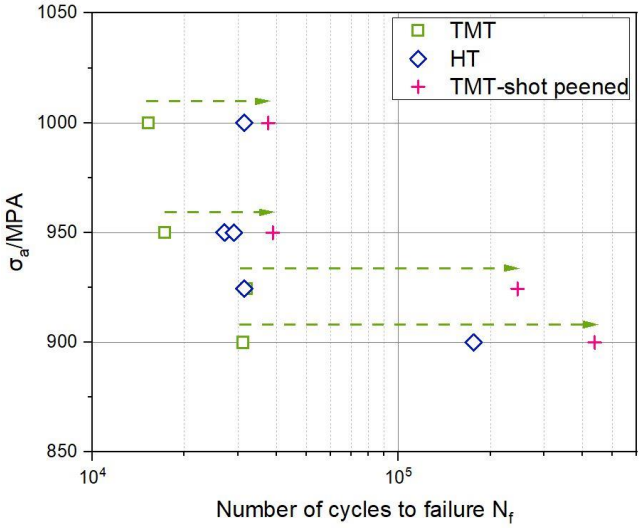

Figure 6.15 Influence of shot peening on the lifetime of TMT specimen for $N_f < 7 \times 10^5$ cycles.

In addition, the fatigue behaviour of TMT specimens for $N_f \geq 7 \times 10^5$ cycles in which the crack initiation is at inclusion inside the volume after shot peening also has been evaluated to see whether the introduced compressive residual stress at the surface and subsurface could also affect the specimens with crack initiation inside the volume or not. As can be seen from Fig 6.16, after shot peening, the TMT specimens still have better fatigue behaviour than HT specimens and the results are in the range of TMT specimens before shot-peening. However, no significant improvement in fatigue behaviour and lifetime of TMT specimens after shot peening can be observed in this regime.

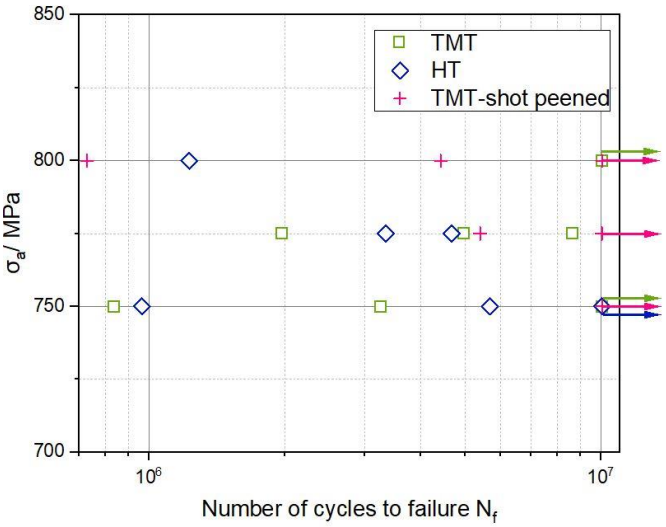

Figure 6.16 Influence of shot peening on the lifetime of TMT specimen for $N_f \geq 7 \times 10^5$ cycles.

6.9 Fatigue lifetime analysis of TMT and HT specimens at a constant stress amplitude in the HCF regime

Figure 6.17 shows the fatigue lifetimes of 16 specimens (eight HT specimens and eight TMT specimens) at the constant stress level of 775 MPa. In the considered lifetime regime, after the TMT the average lifetime was increased from 3.48×10^6 cycles to 4.97×10^6 cycles by about 40 %.

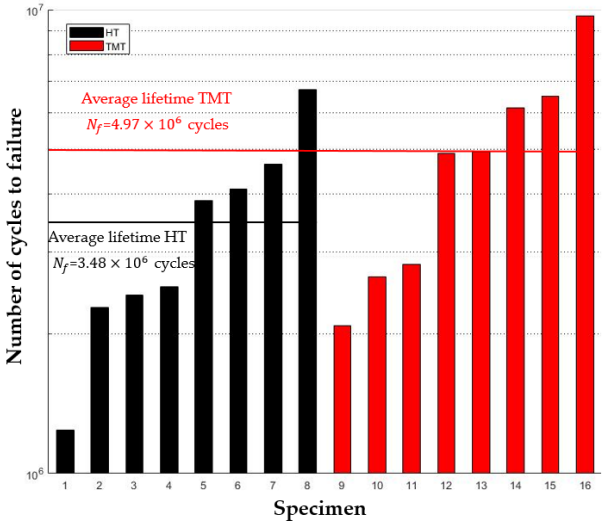

Figure 6.17 Fatigue lifetime analysis of HT and TMT specimens at a given stress amplitude of 775 MPa.

6.9.1 Influence of increasing soaking time during TMT on the fatigue lifetime at constant stress amplitude

The soaking time during TMT has been increased from 15 (s) to 300 (s) to realise the effect of increasing soaking time on the fatigue lifetime and behaviour (see Figure 6.4). After increasing the TMT soaking time to 300 s and similar to subsection 6.9, 8 specimens were cycled at the stress amplitude of 775 MPa. Therefore, the results are presented here. A significant

reduction in the average fatigue lifetime from 4.97×10^6 cycles to 5.097×10^5 cycles has been observed after increasing the soaking time to 300 (s).

6.9.1.1 Effect of increasing the soaking time during TMT on the hardness

As well, after increasing the soaking time to 300 s, the hardness analysis at the gauge length was conducted to realise the effect of increasing soaking time on the hardness of TMT specimens. The hardness analysis at the gauge length shows a significant average hardness reduction from 590 HV to 540 HV which is shown in Figure 6.18.

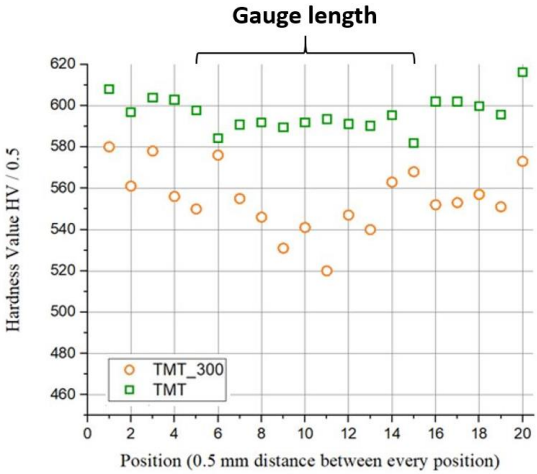

Figure 6.18 Effect of increasing the soaking time from 15 s to 300 s on the hardness.

6.10 Fractography and damage analysis

For a better understanding of the mechanisms leading to crack initiation and propagation and the reason for increasing the fatigue strength due to the TMT as well as for an analysis of the fatigue behaviour of the other treated specimens (HT, MT, and TT), all fracture surfaces have been analysed using SEM imaging.

6.10.1 Type of critical non-metallic inclusions on the fracture surface

For $N_f \geq 7 \times 10^5$ cycles, all the HT, TT, MT, and TMT specimen failures are due to cracks which were initiated at non-metallic inclusions containing similar chemical compositions, when analysed using EDS. It has been observed that in all cases the critical crack-initiating inclusions were always oxides containing aluminum and calcium, in particular AlCaO (CaO-Al_2O_3). Figure 6.19 exhibits a representative SEM image and EDS mapping analysis of a crack-initiating inclusion.

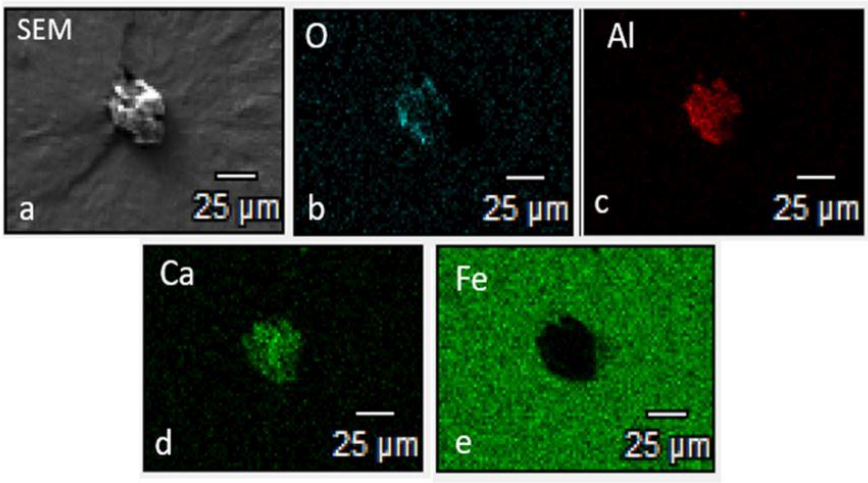

Figure 6.19 EDS mapping analysis of a crack-initiating inclusion. (a) SEM image; (b) O content; (c) Al content; (d) Ca content; (e) Fe content.

6.10.2 Shape of critical non-metallic inclusions on the fracture surface

Figure 6.20 shows two typical shapes of critical inclusions on fracture surfaces. There are eye-shaped inclusions containing sharp edges on one axis (Figure 6.20a) and round inclusions without sharp edges (Figure 6.20b). The form of critical inclusions at the fracture surface of the specimens is independent of the applied treatment and both forms of critical inclusions were found on the fracture surfaces of specimens treated with all four treatments.

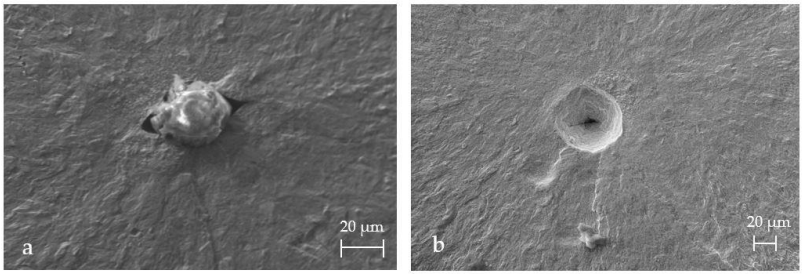

Figure 6.20 SEM images of two typical non-metallic inclusion shapes. (a) Eye-shaped inclusion including two sharp edges - HT specimen; (b) Round inclusion - TMT specimen.

Figure 6.21 shows two critical inclusions of TMT specimen fracture surfaces, which can neither be considered round nor eye-shaped. Instead, these inclusions include rather angular shapes, but no sharp edges can be observed.

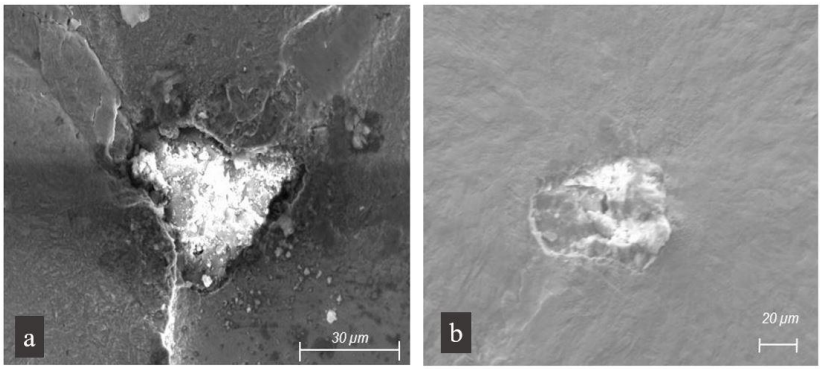

Figure 6.21 Non-metallic critical inclusions. (a,b) containing angular shape of TMT specimens.

A qualitative evaluation of the fracture surfaces resulting from high-cycle fatigue tests at constant stress amplitude (σ_a = 775 MPa) on both TMT and HT specimens shows that most of the inclusions are round shapes and almost 25% of the whole critical inclusions were eye-shaped ones (see Figure 6.22).

6.10.3 Influence of shape and area of critical inclusion on the fatigue lifetime

Figure 6.22 represents the area of critical inclusions of TMT and HT specimens versus the fatigue lifetime for the constant stress amplitude of 775 MPa. The markers indicate the form of critical inclusion. For both HT and TMT specimens, the critical area of non-metallic inclusions scatters significantly. However, for both treatments, no considerable influence of the inclusion area can be observed on the lifetime. Similar to the shape of inclusion, it has been observed that the TMT does not affect the inclusion size distribution of the specimens. All round and angular-shaped critical inclusions for both HT and TMT specimens exhibit a square root area greater than about 35 µm. All critical inclusions with square root areas smaller than about 35 µm are eye-shaped with sharp edges. Therefore, smaller inclusions including sharp edges can be as detrimental as larger ones without sharp edges, which is due to the stress concentration near the sharp edges.

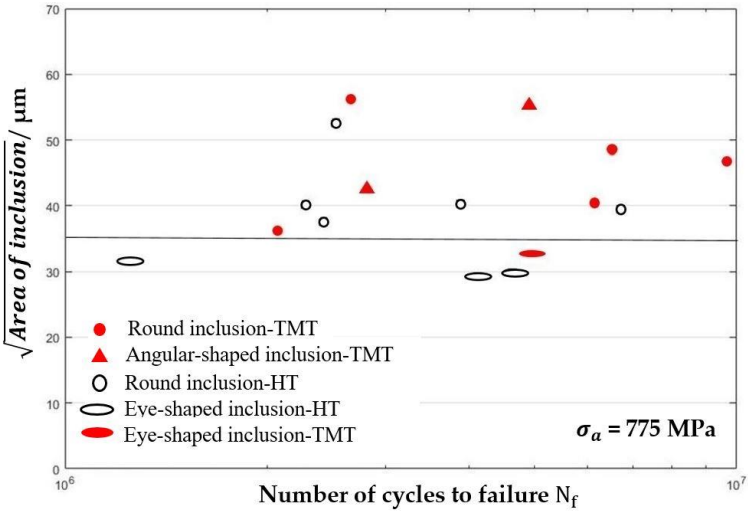

Figure 6.22 Area of critical inclusions for TMT and HT specimens versus lifetime at σ_a = 775 MPa.

Based on the square root of the inclusion area of 35 µm, the minimum required $K_{max,Inc}$ to induce a fatigue crack for inclusions without sharp edges is about 4.05 MPa.$m^{1/2}$. Accordingly, for eye-shaped inclusions featuring sharp edges, the required value of $K_{max,Inc}$ is lower.

6.10.4 Fisheye formation on the fracture surfaces

All tested specimens exhibit fisheyes around the critical inclusions in the HCF regime ($N_f \geq 7 \times 10^5$ cycles). Figure 6.23 shows typically formed fisheyes at fracture surfaces of three specimens. As can be seen in Figure 6.23a and 6.23b, crack initiations occur internally at the inclusion inside the

volume, and the inclusion is surrounded by the fisheye. Both presented fisheyes include a smooth area (SA) until reaching the surface and no remarkable changes in the structure of the fisheye surface can be seen. As soon as the fisheye reaches the surface, oxidation-assisted fatigue crack growth begins. In this stage, the cracks grow mostly away from the touching surface, as can be seen in Figure 6.23c. Therefore, the fisheye grows until the internal crack reaches the surface. In the fisheye presented in Figure 6.23c, a transition from smooth (SA) to rougher (RA) fracture surface with a wavy structure of radially extended peaks and troughs can be observed.

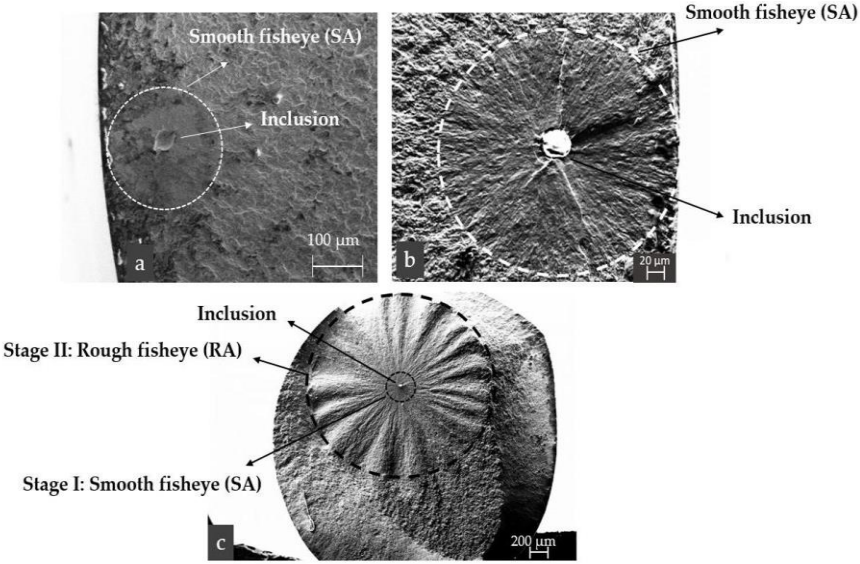

Figure 6.23 Analysis of formation and growth of fisheyes on fracture surfaces under a stress amplitude of 775 MPa. (a) TMT specimen, the inclusion is surrounded by a smooth fisheye (formation of fisheye in a single stage, $N_f = 4.9 \times 10^6$ cycles, depth of inclusion = 125 µm);

(b) HT specimen, inclusion is surrounded by a smooth fisheye (fisheye formation in a single stage, $N_f = 6.7\times10^6$ cycles, depth of inclusion = 180.8 µm); (c) TMT specimen, inclusion is surrounded by a small smooth fisheye and a bigger rough fisheye around the smooth one (formation of fisheye in two stages, $N_f = 9.7\times10^6$ cycles, depth of inclusion = 1.3 mm).

Similar to the inclusion shape, the transition of fisheye from the smooth stage to the rough stage is independent of the applied treatment and it mainly depends on the minimum distance of the inclusion to the free surface of the specimen (inclusion depth). This will be shown in subsection 6.10.6.

6.10.5 Influence of inclusion depth on the fatigue lifetime

Figure 6.24 compares the lifetimes of three HT specimens cycled under the high cycle fatigue regime at a constant stress amplitude of 775 MPa. It is observable that cracks initiated at inclusions with approximately similar inclusion area and form, but at different distances from the free surface (inclusion depth). The inclusion depth (330 µm vs 67.5 µm vs 180.8 µm) does not correlate with the lifetime. However, it should be noted that the limited number of experiments does not allow for any conclusive statements. Certainly, having more experimental results about the influence of inclusion depth on the fatigue lifetime would make the results more reliable.

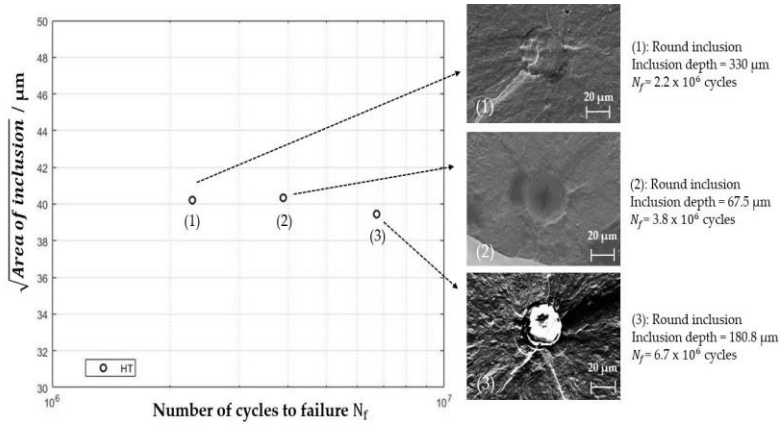

Figure 6.24 Effect analysis of the depth of inclusion on the fatigue lifetime for HT specimens at σ_a = 775 MPa.

6.10.6 Influence of inclusion depth on the fisheye formation

Figure 6.25 represents the fisheye radius (a) and the inclusion depth (b) of HT and TMT specimens versus the fatigue lifetime at a constant stress amplitude of 775 MPa, respectively. The data points in both diagrams correlate strongly for both TMT and HT specimens, which means in all cases fisheyes grow until the surface of the specimens and the size of inclusion depths and the radius of fisheyes are almost the same. Furthermore, there is no obvious relation between inclusion depth or fisheye radius and lifetime. Figure 6.25 also indicates the transition of fisheye surface structure from smooth fisheyes into smooth-rough fisheye. It can be seen that for fisheye

radii below 300 µm, the fisheye surface has only a smooth structure, while for radii above 300 µm, a smooth and rougher, wavy structure as shown in Figure 6.23c is present. A transition from smooth to smooth-rough fisheye has been observed for both TMT and HT specimens. Furthermore, it is visible that the sizes of fisheyes and the corresponding inclusion depths of TMT specimens are considerably larger than for HT specimens.

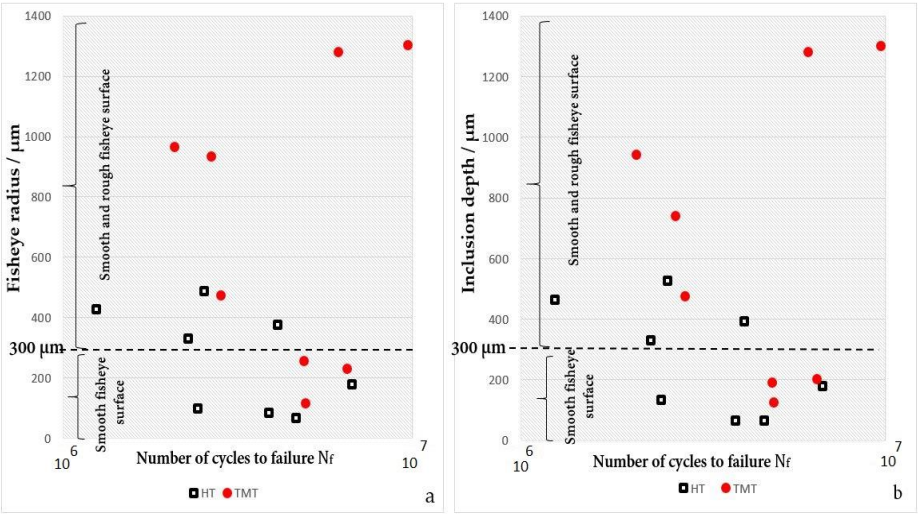

Figure 6.25 (a) Fisheye radius versus lifetime at σ_a = 775 MPa. (b) Inclusion depth versus lifetime at σ_a = 775 MPa.

6.10.7 Fracture surface analyses of TMT specimens after shot peening

As depicted in Figure 6.15, fatigue tests were conducted on TMT specimens after shot peening for $N_f < 7 \times 10^5$ cycles. Fracture surface analysis of TMT specimens after shot peening shows both surface and internal crack initiation. For the stress amplitudes of 1000 MPa and 950 MPa, still, crack initiation at the surface is the main reason for the fatigue failure of the specimens. However, for the stress amplitudes of 925 MPa and 900 MPa a crack initiation transition from surface to the volume of the specimen can be seen. Figure 6.26 illustrates the transition of crack initiation from surface to volume after shot peening of the TMT specimen at σ_a = 900 MPa.

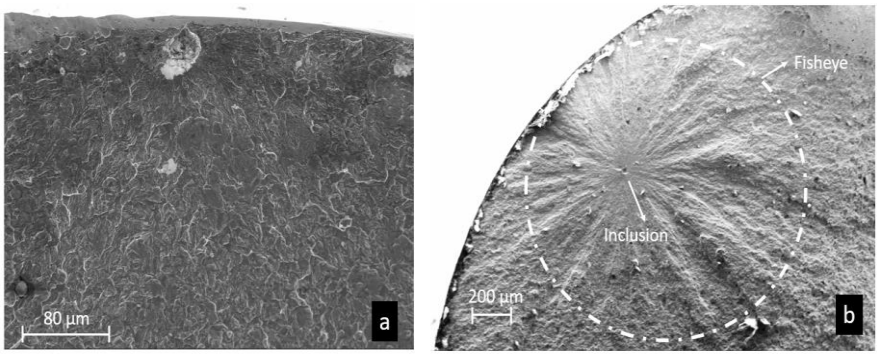

Figure 6.26 The transition of crack initiation from surface to volume after shot peening of TMT specimen at $\sigma_a = 900$ MPa: (a) TMT without shot peening, $N_f = 3.07 \times 10^4$ cycles; (b) TMT with shot peening, $N_f = 4.35 \times 10^5$ cycles.

7 Discussion

7.1 Finding the temperature of maximum DSA and suitable mechanical load for TMT

Observing Figure 6.1 reveals that at all temperatures the highest cyclic hardening (refer to subsection 2.4) occurs between the first and the second cycle and after that by increasing the number of cycles, the cyclic hardening effect reduces considerably. This means that during the first loading cycle a relatively large plastic deformation takes place and the dislocation density is remarkably increased compared to subsequent cycles. Findings from other research studies similarly indicate that the greatest cyclic strengthening occurs between the first and the second cycle. Therefore, to avoid any cumulative damage during the treatment, the number of cycles should be minimized [13,15]. Furthermore, it can be seen that the strongest extent of cyclic hardening and, therefore, the maximum of this ratio (the maximum ratio of the plastic strain amplitude value between the first and the last cycle) was found at 265 °C, which is interpreted as the temperature of the maximum DSA for the applied testing frequency. This means that at this temperature, the generated density of mobile dislocation is at the highest compared to the other temperatures and the locking of edge dislocations due to the accumulation of solved carbon atoms in the dilatational region of the dislocations is quite significant [13,15]. The reason for the strengthen-

ing reduction at a temperature lower and higher than 265 °C can be explained by the lower and higher diffusion rate of solute atoms (carbon) which cannot be adjusted to the mobile dislocation motion and cause therefore a lower immobilisation of dislocations [13]. Figure 6.2 represents plastic strain amplitude decreases (stepwise cyclic hardening) from 600 MPa to 1600 MPa. However, the stress level at 1700 MPa contains three cycles of cyclic softening, and only the last 2 cycles can be considered as a cyclic hardening. Therefore, it can not be considered as a suitable mechanical load for the TMT. Kerscher et al. (2005) revealed that stepwise increasing the mechanical load during TMT can optimize the hardening effect. However, applying mechanical loads resulting in cyclic softening during TMT leads to premature damage [15]. As shown in Figure 6.2, the TMT in this study is characterized by experimental parameters showing cyclic hardening only from 600 MPa to 1600 MPa. Hence, an increasing load amplitude at every fifth cycle by equidistant steps of 100 MPa from 600 MPa to 1600 MPa at 265 °C, with the frequency of 1 Hz, has been chosen for the TMT.

7.2 Effect of TT, MT and, TMT on the Hardness

As depicted in Figure 6.7b, the average hardness reduction inside the gauge length (position 5 to 15) of the TT specimen by 26 HV compared to the HT one is attributed to the thermal effect of the TT. Since the TT is performed at the temperature of 265 °C, which is higher than the tempering temperature of 180 °C during the initial heat treatment, the TT can be considered to

work as short-term tempering which leads to the transformation of martensite (initial state) to tempered martensite [14,87]. This transformation from martensite to tempered martensite during thermal treatment is one of the main reasons for the hardness reduction. Yudo et al. (2021) also analysed the hardness behaviour of carbon steel under different tempering conditions and realised that due to the formation of tempered martensite in the microstructure after tempering the hardness values were decreased. This is because tempered martensite is inherently softer than martensite [88].

Figure 7.1 shows the microstructural analysis of the specimen both before the thermal treatment (HT) and after the thermal treatment (TT). The formation of tempered martensite after TT is observable from Figure 7.1b.

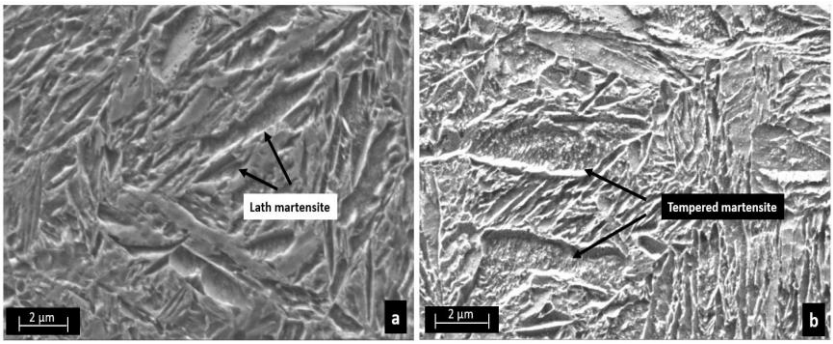

Figure 7.1 Microstructural analysis: (a) HT specimen without any extra thermal treatment; (b) TT specimen

The temperature outside of the gauge length was above 200 °C, which shows that outside of the gauge length is also affected by thermal treatment

due to the heat flow and thermal conduction, and, thus, a hardness reduction outside of the gauge length can be expected. However, as during TT, the temperature outside of the gauge length is not as high as inside the gauge length (the heating induction coil was located exactly at the gauge length). Thus, the material outside of the gauge length is not highly affected by TT and the hardness decrease outside of the gauge length is not as pronounced as inside of the gauge length. Other investigations also show that for different carbon steels applying tempering leads to a decrease in hardness value [87,89]. A minor increase in hardness over the gauge length of the MT specimen is possibly due to the cyclic hardening during mechanical loading at room temperature. Naoe et al.(2020) analysed the effect of cyclic loading on the mechanical properties of steel and showed that cyclic loading at RT can lead to a slight increase in hardness when cyclic hardening occurs [90]. However, since the TMT is a combination of TT and MT, it is affected by both processes. As discussed above, TT leads to a reduction in the hardness and MT causes an increase in the hardness, Therefore, the overall effect on the hardness behaviour of the TMT specimen is not significant and it is almost similar to HT one. Like the TT specimen, it can be seen that outside of the gauge length of the TMT specimen, the hardness increases compared to the gauge length. This is due to less effect of the TT outside of the gauge length, as well as the slight cyclic hardening effect of the MT process during TMT.

7.3 Transition of fatigue crack initiation site from surface to volume of specimen

As it is described in subsection 6.5, the fatigue fracture analysis indicates that the crack initiation site is independent of the applied treatment (HT, MT, TT, and TMT) and mainly depends on the fatigue lifetime and applied stress amplitudes. The dependence of crack initiation sites on fatigue lifetime and stress amplitude has been reported by other investigations as well [36,37].

Surface crack initiation typically occurs at high-stress amplitudes, when the applied stresses reach a level that is high enough to cause the extrusion and intrusion of slip bands on the surface of the specimen [91]. It has been confirmed by multiple investigations that crack initiation transition from surface to volume of the specimen at high-stress amplitudes may occurs when significant compressive residual stresses at the surface and subsurface of the specimens were induced [72,92–94]. Compressive residual stresses can avoid any crack initiation at the surface and subsurface due to restricting crack initiation. As a result, the crack initiation shifts from the surface to the volume of the specimen [93,94]. As shown in Figure 6.13 the HT and TT specimens with compressive residual stresses both on the surface and subsurface still exhibit crack initiation from the surface at high stress amplitudes and within a lifetime shorter than 7×10^5 cycles. Hence, for the same lifetime the TMT and MT specimens, which induce tensile residual stresses and reduce the compressive residual stresses at both the surface and

subsurface (shown in Figure 6.13) clearly do not influence the shift from surface crack initiation to internal crack initiation. However, by decreasing the stress amplitudes which corresponds to $N_f \geq 7 \times 10^5$, the extrusion and intrusion of the slip bands at the surface are not possible anymore (the applied stresses are usually far below the elastic limit of the material). Therefore, a transition to an internal crack initiation occurs where localised cyclic plastic deformation and stress concentrations around the inclusion are the main reasons for the crack initiation [91].

7.4 Fatigue behaviour analysis of TMT specimen ($N_f \geq 7 \times 10^5$)

As it is presented in subsection 6.5, for $N_f \geq 7 \times 10^5$ cycles the crack initiation from inclusions inside the volume of the specimen is one of the most common reasons for the fatigue failure of steels. As a result of DSA and interacting carbon atoms with the mobile dislocations around the non-metallic inclusion, a new dislocation structure with higher dislocation density could be formed which is remarkably more stable than before and therefore, it could lead to an increase in fatigue strength [13,14,65]. Hong and Lee et al. (2004) performed a microstructural analysis using Transmission Electron Microscopy (TEM) on stainless steel (SAE 316L). The objective was to investigate the microstructural changes occurring during cyclic deformation with a load ratio of -1 and a strain amplitude of ±0.5% at both room

temperature (RT) and the temperature at which DSA occurs. The results showed that at RT, the dislocations exhibited a cell structure (shown in Figure 7.2a). However, for cyclic loading at 400 °C, where DSA occured, there was a noticeable increase in dislocation density as well as a transition in the dislocation structure from cellular to planar (shown in Figure 7.2b) [95,96]. It is important to note that the TEM analysis showed in Figure 7.2 is not result of this research project, and the examination of the increase in dislocation density was conducted qualitatively.

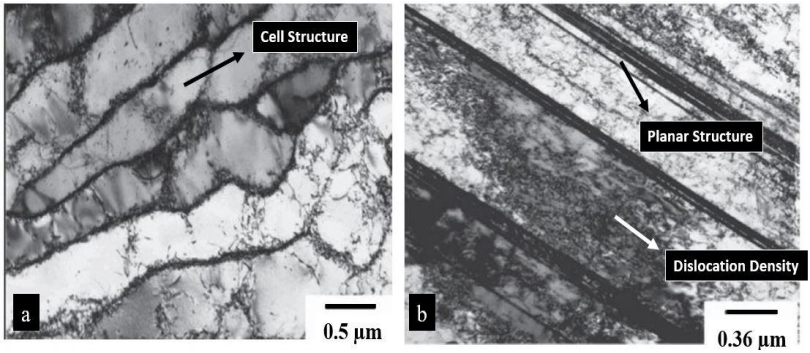

Figure 7.2 TEM microstructural analysis of stainless steel (SAE 316L) during cyclic loading with the load ratio of R = -1 and $\Delta\varepsilon_t/2 = \pm 0.5\%$. (a) Cyclic deformation at RT, $\dot{\varepsilon} = 1\times10^{-3}$/ sec (non-DSA regime); (b) Cyclic loading at 400 °C, $\dot{\varepsilon} = 1\times10^{-2}$/ sec (DSA regime) [95,96].

The rise in dislocation density is due to interactions between diffusing carbon atoms and mobile dislocations during DSA [95]. These interactions are mainly dependent on temperature and strain rate. In other words, during DSA, the strain rate affects the dislocation velocity, and temperature influences the diffusion speed of solute atoms [59]. The diffusion rate of solute

atoms corresponds to the temperature, which means that by increasing the temperature during DSA, the solute atom (e.g., carbon in the case of steels) diffusion rate and consequently the local solute concentration increase [60]. Since in Figure 7.2a, the cyclic loading occurs at RT and thus, the generated dislocation density is at its lowest. However, by increasing the temperature to 400 °C, diffusing carbon atoms and gliding dislocations have approximately the same velocity, allowing the solute atoms to pin the mobile dislocations [61]. This means that during plastic deformation in the DSA regime, a new dislocation can be formed which could be impeded in their movement. This locking process (especially around the internal non-metallic inclusion) can increase the resistance to any further dislocation movement, thereby strengthening the microstructure [13,65]. Therefore, for $N_f \geq 7 \times 10^5$ cycles where the fatigue crack initiation is at non-metallic inclusions inside the volume, applying stepwise increasing cyclic hardening in the temperature of maximum DSA enables us to strengthen the microstructure around the critical non-metallic inclusions. Furthermore, Figure 6.17 confirms the enhancement of fatigue lifetime after a TMT compared to HT at a constant stress amplitude in the HCF regime which is assumed to be a result of the strengthening of dislocation structure around inclusions and it has a good agreement with the results of former investigations [14].

- **Analysis of TMT effect on the $K_{max,Inc}$**

As it is discussed in subsection 2.3.1, $K_{max,Inc}$ is an approximate way of analysing the maximum stress distribution around a flaw or defect [1,52].

It is noticeable that in order to see the effect of TMT on the values of $K_{max,Inc}$ and make a comparison with the $K_{max,Inc}$ values of HT ones, it is essential to consider the area of inclusions within the same ranges. This precaution is important to avoid the influence of the inclusion area which remains independent of the applied TMT treatment on the comparative results [22,97].

The higher values of $K_{max,Inc}$ observed for the equivalent crack initiation areas in TMT specimens, as compared to HT ones in the HCF regime (indicated by numbers from 1 to 4 as shown in Figure 6.10b) are a result of the strengthening effect of TMT on the microstructure around the critical inclusions. Due to the applied TMT, the damage tolerance of the microstructure around the inclusions is increased, which in the end leads to higher fatigue lifetimes and enhances the fatigue strength in this regime (see Figure 6.9). For the equivalent inclusion area, half of TMT treated specimens show higher K_{max}values (see Figure 6.10b). However, TMT cannot increase the $K_{max,Inc}$ of all the TMT specimens. This can be explained by Figure 6.9, which shows the increase in fatigue strength for TMT specimens compared to HT ones. However, it does not necessarily mean that all the TMT-treated specimens should show better fatigue behaviour than HT ones. Kerscher et al. (2008) also analysed the $K_{max,Inc}$ at fracture surfaces of both TMT and non-TMT-treated specimens of 100Cr6 steel. Similarly, the $K_{max,Inc}$ of TMT treated specimens were higher than the initial state

ones. However, this increase in $K_{max,Inc}$ was not observed in all TMT specimens. According to Kerscher, the vicinity of inclusions is strengthened step by step during stepwise increased load amplitude of TMT which eventually leads to the stabilisation of the dislocation structure in the vicinity of inclusions and increasing the K_{max} around the inclusions [14].

TMT and HT specimens originate from identical batches, ensuring that the sizes of critical inclusions are almost within the same ranges. However, TT and MT specimens belong to different batches, showing significantly disparate inclusion sizes. Consequently, comparing the K_{max}values of TT and MT specimens with those of TMT and HT specimens is not feasible.

7.5 Fatigue behaviour analysis of TT and MT specimen ($N_f \geq 7 \times 10^5$)

The reason for the significant reduction of the fatigue strength after TT in Figure 6.9 could be possibly answered by the hardness analysis of the specimens, which is shown in subsection 6.4. Due to the hardness decrease after TT, the crack initiation at the inclusion occurs at the lower fatigue stress level, which consequently leads to a decrease in the fatigue strength and earlier fatigue failure [14]. As can be seen from the hardness analysis shown in Figure 6.7, the average hardness values drop after TT from 594 HV to 568 HV (5% reduction) which correlates well to the fatigue strength decrease from 712 MPa to 677 MP (5% decrease in the fatigue strength) after

TT. According to Schmiedel et al. 2021, the fatigue strength reduces due to a decrease in the material's hardness during tempering at higher temperatures [98] and a reduction in the hardness of the material leads to an increase in the crack growth rate and earlier failure of the specimen [99]. He considered the fatigue behaviour of quenched and tempered steel within the HCF regime at room temperature (RT) and at 200°C. The findings showed a 15% reduction in the fatigue strength following a 12% decrease in hardness [98], aligning well with our findings regarding the correlation between reduction in the fatigue strength and hardness after tempering of the steel. Furthermore, it should be noted that the amount of hardness reduction is highly dependent on the tempering temperature and time. An increase in tempering temperature and time can lead to a remarkable decrease in hardness values [100].

The effects of TT and MT on the fatigue behaviour were presented in Figure 6.9, confirming how important it is to apply both thermal and mechanical treatment at the same time to improve the fatigue strength of quenched and tempered steel.

As shown in the TEM analysis in Figure 7.2a, only cyclic loading at RT cannot activate the carbon atoms to interact with dislocations. Therefore, no increase in the dislocation density and strengthening of the microstructure can be observed [59,60,95,96]. Since the strengthening effect during cyclic loading is not significant, no enhancement in the fatigue behaviour is visible. This means that an MT, which consists of cyclic loading at room

temperature without any thermal treatment cannot strengthen the microstructure around the critical inclusion and therefore, no significant influence on the fatigue behaviour and endurance limit can be seen. According to Kreethi et al. 2015 and Hussain et al. 1993, cyclic loading at room temperature rearranges the dislocations into a new configuration. However, there is no notable increase in dislocation density [101,102]. Since MT occurs at room temperature, where the carbon atom diffusion rate is at its minimum level, no locking process during cyclic loading could take place to strengthen the microstructure.

By comparing the fatigue behaviours of HT, TT, MT and TMT specimens in Figure 6.9, it can be realised that only a combined thermo-mechanical treatment (TMT) at the temperature of maximum DSA can strengthen the microstructure around the inclusions, which finally results in better fatigue behaviour of TMT specimens. Individual MT and TT have no or even negative influence on the fatigue behaviour, respectively.

7.6 Effect of HT, TT, MT, and TMT on the residual stress at the surface and subsurface of the specimen

Figure 6.12 illustrates a significant disparity in residual stress between the surface and subsurface regions of both HT and TT specimens compared to

MT and TMT specimens. This contrast highlights the impact of cyclic tensile-compressive loading applied during the TMT and MT processes on the residual stresses at the surface and subsurface. This means that applied cyclic tensile - compressive mechanical loading during TMT and MT leads to a significant reduction of compressive residual stress at the surface and subsurface of the specimens. Holzapfel et al. (1998) also analysed the residual stress at the surface and subsurface of steel AISI4140 after cyclic loading at different temperatures ranging from 25 °C to 400 °C. He reported that at each temperature and after a certain stress amplitude by increasing the number of cycles, the compressive residual stress at surface and subsurface is decreasing. He showed that the reduction of surface and subsurface compressive residual stress at higher temperatures during cyclic loading is even more significant [25]. This suits to the results of the surface and subsurface residual stress analysis of TMT and MT specimens. As shown in Figure 6.12, applying cyclic loading at the temperature of 265 °C during TMT decreased the surface compressive residual stress more pronounced than MT which is conducted at room temperature.

The reason for the highest amount of compressive residual stress at the surface and subsurface of HT specimens can be explained by the temperature difference between the core and surface during quenching and tempering. During the time of quenching, the surface shrinks more than the interior creating pressure against the core. Since the core does not shrink by the

same amount, an irreversible plastic flow occurs leading to a generation of compressive residual stress at the surface of the specimen [103].

Furthermore, as a result of quenching a phase transformation from austenite to martensite occurs. Austenite has an FCC structure, higher density, and lower yield stress than martensite with a BCC structure. During the cooling process, the difference in density between austenite and martensite causes an expansion in volume [104]. Additionally, the transition from austenite to martensite induces a variation in yield stress, leading to transformation plasticity [105]. Both transformation plasticity and volume changes at the time of quenching have a considerable impact on the development of compressive residual stresses at the surface and subsurface of specimens [106–109]. During the tempering of the specimen, the generated surface compressive residual stress can be reduced. However, since the tempering temperature is 180 °C, the decrease in compressive residual stress is not remarkable [25]. TT can also be considered as a tempering at the temperature of 265 °C for 70 s. Since tempering can reduce the compressive residual stress at the surface and subsurface of quenched and tempered steel [25], a compressive residual stress decrease can be expected at the surface and subsurface of TT specimens compared to HT ones.

7.7 Influence of generated surface and subsurface residual stress after TMT and MT on the lifetime ($N_f < 7 \times 10^5$ cycles)

The reason for the negative influence of TMT and MT on the fatigue lifetimes and fatigue behaviour for $N_f < 7 \times 10^5$ cycles (shown in Figure 6.11) can be rationalised by considering the residual stresses at surfaces and subsurfaces of the HT, TT, TMT, and MT specimens. On the one hand, nucleation and initiation of the crack for $N_f < 7 \times 10^5$ cycles is at the surface and subsurface of the specimens (see subsection 6.5). On the other hand, depending on the applied treatment, compressive residual stresses at the surface and subsurface can be changed or even tensile residual stresses might be generated. In the case of TMT specimens, the generated tensile residual stress and the considerable decrease of compressive residual stress at the surface and subsurface simplify the initiation of the crack remarkably and lead to keeping cracks open during crack propagation [73,74] compared to HT and TT specimens whose surface and subsurface are covered by significant compressive residual stress. For MT specimens, tensile residual stress cannot be observed at the surface and subsurface of the specimens. However, residual stress analysis reveals a significant reduction in the compressive residual stress compared to HT and TT ones (see Figure 6.12). This significant decrease in the compressive residual stress leads to a reduction in the fatigue lifetime compared to HT and TT specimens (see Figure 6.11). Maleki et al. (2020) considered the fatigue behaviour of high carbon steel

(AISI1060) during different generated residual stresses at the surface and subsurface of the specimens. The results show that both fatigue lifetime and fatigue strength correlate strongly with the induced compressive residual stress at the surface and subsurface of the specimens and reduction in compressive residual stresses at the surface and subsurface causes of remarkable decrease in the fatigue strength and fatigue lifetime [110].

Contrary to generation of tensile residual stress or decrease in the compressive residual stress at the surface and subsurface (TMT and MT specimens), the presence of considerable compressive residual stress (HT and TT specimens) can prolong the crack initiation and propagation and keeps the crack closed [72,111]. As a result, for $N_f < 7 \times 10^5$ cycles a remarkable fatigue lifetime difference can be observed between the TMT and MT specimens on the one hand and HT and TT specimens on the other (shown in Figure 6.11).

In contrast to other studies that focus on improving the fatigue strength of steel by TMT in the temperature of DSA, where crack initiation occurs internally (HCF regime) [13,14], the present finding reveals that TMT in the LCF regime and the regime where crack initiation occurs at the surface and subsurface leads to a significant reduction in fatigue lifetime. This reduction is due to the presence of generated tensile residual stress and a considerable decrease in compressive residual stress at the surface and subsurface of the TMT specimens.

Since for $N_f \geq 7 \times 10^5$cycles, the crack initiation is at the inclusion inside the volume and not from the surface (see subsection 6.5), thus, the crack initiation and propagation and subsequently fatigue lifetime is not affected by the generated residual stress at the surface of the different treated specimens.

7.8 Analysis of the effect of shot peening on the residual stress distribution, hardness, and lifetime of TMT specimens

Tensile residual stress was identified at the surface and subsurface of TMT specimens (see Figure 6.12). Due to promising fatigue behaviour of TMT in the regime where crack initiation occurs from inclusions inside the specimen volume ($N_f \geq 7 \times 10^5$ cycles, see Figure 6.9), shot peening was implemented to regenerate compressive residual stress at the surface and subsurface of TMT specimens. However, the MT and TT specimens do not exhibit any enhancement in the fatigue lifetime and fatigue strength for $N_f \geq 7 \times 10^5$ cycles (see Figure 6.9). As well, the residual stress analysis of the surface and subsurface of HT specimens has already shown a remarkable amount of compressive residual stress. Therefore, applying shot peening was only conducted for TMT specimens to increase fatigue behaviour and fatigue lifetime of TMT specimens for $N_f < 7 \times 10^5$ cycles where the crack initiation is from the surface and subsurface.

According to Luong et al. (2009) and Watanabe et al. (2003), shot peening has a great influence on the introduction of compressive residual stress and improvement of fatigue lifetime [72,111]. A higher and deeper generation of compressive residual stress at the surface and subsurface of the specimen can increases the fatigue lifetime [112]. Enhancement of fatigue lifetime using shot peening depends to a great extent on the in-depth compressive residual stress profile produced in the specimen. Figure 6.13 demonstrates that the magnitude and depth of the compressive residual stress created at the surface and subsurface of the TMT specimen after shot peening exceed those of the initial state (HT). This observation indicates that shot peening was conducted in a good performance. Furthermore, the positive effect of shot peening on the hardness values at the surface and subsurface of a TMT specimen has been shown in Figure 6.14. The hardness value increases from the surface until it reaches its maximum value at the depth of 60 µm inside the volume of the specimen (635 HV). However, for the measured hardness values deeper than 60 µm from the surface, a hardness drop can be seen. This decrease in the hardness can be explained as a return to the specimen's original hardness. By comparing the effect of shot peening on the compressive residual stress and hardness of the TMT specimens, it becomes clear that at a depth of 60 µm, both compressive residual stress and hardness reach their maximum peak values before subsequent decreasing (see Figures 6.13 and 6.14). This means that the 60 µm distance below the surface of the gauge length is the effective hardness and compressive residual stress depth which is induced by shot peening.

According to Vöhringer, the plastic deformation induced by shot peening leads to a hardness increase at the surface and subsurface of the specimen. Since plastic deformation and dislocation density induced by shot peening are decreasing with increasing distance from the surface, thus, the hardness values reduce [113]. The results are in good agreement with the other researches regarding the influence of shot peening on the hardness. Sanni Slat et al. (2018) discussed that due to work hardening, the microhardness of the surface and subsurface of the shot peened specimen increases until a certain depth inside the volume of the specimen [114].

The fatigue behaviour of the TMT specimen after shot peening needs to be discussed in two different regimes. For $N_f < 7 \times 10^5$ cycles where the crack initiates from the surface and subsurface, due to the reintroduction of compressive residual stresses and improvement of the hardness at the surface and subsurface after shot peening, retardation in the nucleation and initiation of the crack at the surface and subsurface of the specimens or a transition from surface crack initiation to an internal crack initiation can be observed. In the end, this leads to significant improvements in the fatigue lifetimes of TMT-shot peened specimens (shown in Figure 6.15). The lifetimes of TMT-shot peened specimens are even significantly longer than those of HT specimens due to the higher values of hardness and compressive residual stresses at the surface and subsurface. Watanabe and Saklakoglu also observed that after a suitable shot peening treatment at the surface of the specimens, significant fatigue lifetime improvement is obtained.

They found that the shot peening introduces the near-surface compressive residual stress field, which increases the threshold of crack initiation during fatigue and subsequently leads to a fatigue lifetime enhancement of shot-peened specimens [72,92].

The reason for the significant enhancement of fatigue lifetimes at the stress amplitudes of 925 MPa and 900 MPa, compared to stress amplitudes of 1000 MPa and 950 MPa, as depicted in Figure 6.15, is that shot peening causes a strong compressive residual stress generation (see Figure 6.13) and increased hardness at surface and subsurface of the specimen (see Figure 6.14). This prevents any crack initiation at the surface and subsurface. As a result, the crack initiation shifts from the surface to the volume of the specimen, where the TMT strengthened the microstructure around non-metallic inclusions (see Figure 6.26). This reinforcement at both surface and volume of the specimen using shot peening and TMT effectively delays the initiation of cracks within the material. Therefore, for both stress levels of 925 MPa and 900 MPa, a pronounced improvement in the fatigue lifetime can be observed. Breuner et al. (2021) and Shiozawa et al. (2002) also reported a crack initiation transition from the surface to the volume of the specimen after shot peening [93,94]. According to Shiozawa, the crack initiation transition after shot peening is due to the hardness increase and the introduced compressive residual stress at the surface and subsurface of the specimen by restricting crack initiation. He observed that the crack initiation site

movement from the surface to the interior at the same stress amplitude after shot peening [94].

However, the stress levels of 1000 MPa and 950 MPa are high enough to extrude and intrude the slip bands at the surface of the specimen even after shot peening. Therefore, only a retardation in the surface crack initiation is visible and no crack initiation transition from the surface to the volume of the specimen can be seen.

For $N_f \geq 7 \times 10^5$ cycles, since cracks initiate typically at inclusions inside the volume of the specimens, the compressive residual stresses at the surface and subsurface generated by shot peening have an insignificant influence on the initiation of the crack (shown in Figure. 6.16). It can only affect and decelerate the propagation of the crack until the crack reaches the surface of the specimen. Shiozawa et al. (2002) also reported no fatigue strength and lifetime enhancement of the shot-peened specimens when the crack initiates internally and not from the surface [94]. Nevertheless, it has been observed from other investigations that the fatigue lifetimes are mainly governed by the crack initiation stage rather than by the crack propagation stage [19,20]. Thus, no remarkable influence in fatigue lifetime was expected.

7.9 Analysis of type and shape of non-metallic inclusions at the fracture surface

As previously stated in subsection 6.10.1, chemical compositions at non-metallic inclusion of the fracture surfaces were always oxides containing aluminum and calcium. According to Lang et al. (2016), AlCaO ($CaO\text{-}Al_2O_3$) is the most detrimental inclusion from which the crack initiates for the 42CrMo4 steel in the HCF and VHCF regimes [45]. In another study, Spriestersbach et al. (2014) showed that AlCaO inclusions ($CaO\text{-}Al_2O_3$) are comparatively larger than the others, which subsequently lead to higher maximum stress intensity factor (K_{max}) values compared to other types of inclusions. Ultimately, this could result in the initiation and propagation of the crack in the specimen [42]. As it is described in subsection 6.10.3 and Figure 6.22, after the analysis of the fracture surfaces of both TMT and HT specimens, three different inclusion shapes (round, angular, and eye-shaped) with the same chemical compositions are found as critical inclusion shapes which lead to crack initiation and finally failure of the specimens. Oxide inclusions containing both aluminum (Al) and calcium (Ca), are typically reported as having a round or globular shape [23,115] which is in good agreement with the SEM results of this study (see Figures 6.20b). However, on the fracture surface of the specimens, there were also observed inclusions of AlCaO ($CaO\text{-}Al_2O_3$) that displayed eye-shaped (see 6.20a) and angular shapes (see 6.21). Regarding the deformation of round inclusions into eye-shaped or angular forms, one might suggest that deformation

of inclusion occurred during the fatigue experiment. However, the hardness of AlCaO ($CaO\text{-}Al_2O_3$) inclusion is significantly higher (2800 HV) [116] than the hardness of the specimen (600 HV). As a result, any remarkable deformation in the shape of inclusion during fatigue test is not expected.

Spriestersbach et al. (2014) considered the fatigue behaviour of artificial defects (artificial pores) with a shape and size comparable to AlCaO ($CaO\text{-}Al_2O_3$) inclusions at subsurface of high strength steel (100Cr6). The artificial inclusions were created by removing the material at the subsurface of the specimen using ultra-short laser. This investigation was conducted at VHCF regime. He observed crack initiation from the artificial inclusion. Nevertheless, no remarkable changes in the shape and size of inclusions during fatigue experiment were reported [42].

Based on Bernard et al. (1981) and Ren et al. (2022), non-metallic inclusions can be deformed during the hot and cold rolling process. Depending on the temperature, inclusion composition and physical properties, the plasticity varies and a round inclusion may deform differently [97,117]. For instance, during the hot rolling process, the deformability index of oxide inclusions was often related due to the melting temperature and viscosity of inclusions [97]. Accordingly, it is assumable that the initial round shape of AlCaO ($CaO\text{-}Al_2O_3$) inclusions of specimens was deformed during the hot and cold rolling process of steel production and resulted in forming angular and eye-shaped inclusions.

7.10 Effects of shape and area of critical inclusions on the fatigue lifetime

In this study, the effects of the shape and inclusion area on the lifetime were investigated at a constant stress amplitude to avoid the influence of stress level changes on the fatigue lifetime and having an accurate analysis of the area and shape of inclusions (see Figure 6.22).

As can be seen, for both TMT and HT specimens the square root of inclusion area varies from almost 30 µm to above 55 µm. This means that during cyclic hardening of TMT, no remarkable changes in the area of inclusions occurred and TMT has no considerable effect on the area. Thus, TMT possibly changes the microstructure around the inclusions.

Furthermore, it is observable that for both HT and TMT specimens, the lifetime does not correlate with the inclusion area. For instance, the fatigue lifetime of the specimens does not exhibit a clear correlation with the area of round or angular inclusions. This is rather surprising since one might expect that for the given constant stress amplitude and similar shapes, larger inclusions lead to earlier crack initiation and consequently shorter lifetimes. However, other studies have also shown that the critical inclusion area has no significant effect on the lifetime of steels after crack initiation at internal inclusions in the HCF regime [18,19]. Guan et al. (2017) made a Voronoi finite element modelling (VFEM) to analyse the fatigue behaviour of different sizes of oxide inclusions ranging from 5 µm to 20 µm in bearing

steel. The results show that as the round inclusion size increases, the area of stress concentration expands. However, the maximum stress concentration around the inclusions is very similar (see Figure 7.3) [17].

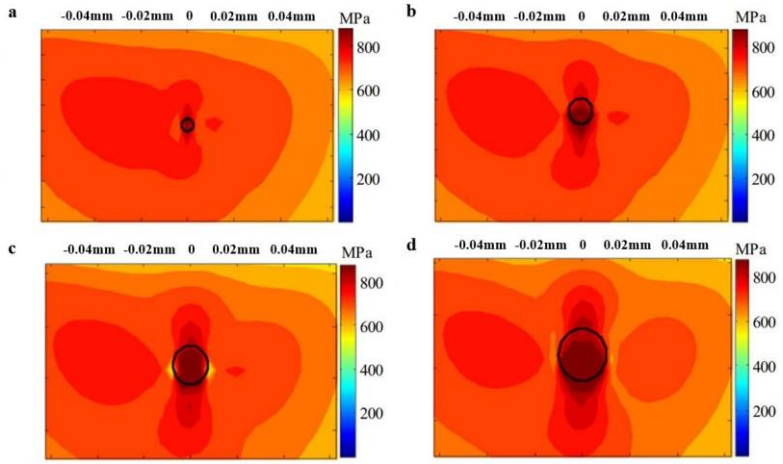

Figure 7.3 Effect of inclusion area on the stress distribution of round inclusion. (a) 5 µm; (b) 10 µm; (c) 15 µm; (d) 20 µm [17].

This means that only an increase in the area of critical inclusion does not necessarily lead to an increase in the maximum stress concentration around the inclusion and subsequently earlier crack initiation and failure of the specimen. There are other important factors such as the shape of inclusions that have an effect on the maximum stress concentration and must be also taken into account during the analysis of critical inclusions.

Figure 6.22 shows that, all critical inclusions with square root areas smaller than about 35 µm are eye-shaped with sharp edges. This means that small

inclusions including sharp edges can be as detrimental as round bigger ones due to higher-stress concentration around the sharp edges that become the initiation point for cracks. Consequently, these sharp-edged inclusions even with smaller areas can significantly contribute to the failure of the specimens. Apparently, the shape of inclusions plays a more important role for crack initiation than the area. The results presented here are in good agreement with other studies concerning inclusions characterized by sharp edges or voids [54].

7.11 Inclusion depth and fisheye formation

7.11.1 Analysis of effect of inclusion depth on the fatigue lifetime

Stanzl-Tschegg et al. (2010) measured fatigue crack growth of AISI410 stainless steel experimentally at a frequency of 19 kHz under different load ratios in vacuum (10^{-3}Pa) and ambient air (see Figure 7.4) [47]. As can be seen, the crack growth rates under various load ratios are higher in ambient air compared to the rates observed in vacuum. Furthermore, it can be obtained that the stress intensity thresholds for the tested specimens in ambient air are lower than those in the vacuum with the same load ratios.

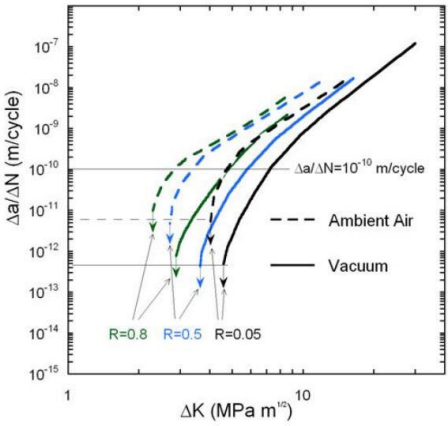

Figure 7.4 Comparing fatigue crack growth in vacuum (10^{-3}Pa) and air [47].

The reason for higher crack growth rates and lower stress intensity thresholds of ambient air compared to vacuum can be attributed to the corrosive effects of air moisture and hydrogen embrittlement [47].

As observed by Figure 6.24 and Figure 6.25b, no correlation has been found between inclusion depth and fatigue lifetime at a constant stress amplitude. Based on the crack growth rate analyses shown in Figure 7.4, it can be assumed that due to the detrimental effect of air moisture, the crack propagation rate is much higher for an internal crack that has reached the surface than for a crack that is still in the fisheye stadium. Therefore, when the critical inclusion is located at a larger distance from the surface the lifetime period required in the crack propagation stage should be longer to reach the surface. As the results show no clear influence of inclusion depth on the fatigue lifetime, which is confirming also other investigations in the HCF

regime [19,20], it can be deduced that the fatigue lifetime is mainly governed by the period before crack initiation and the crack propagation stage comprises only a small percentage of the total fatigue lifetime. The parameter responsible for a fatigue lifetime scatter of about factor three for critical inclusions with nearly the same inclusion area and shape at a constant stress amplitude and the same specimen state, remains unclear (see Figure 6.24). A possible explanation might be the difference in the volumetric shape and size of inclusions. At the fracture surface, it is only possible to see the area and shape of inclusion. However, the volumetric shape and size of inclusion inside the specimen are not visible which may in this case play a role in the sooner or later initiation of the crack at the inclusions and consequently different fatigue lifetimes of the specimens.

It is important to mention that obtaining a larger set of experimental results concerning the impact of inclusion depth on fatigue lifetime would enhance the reliability of the results. However, analysing the effect of inclusion depth on fatigue lifetime is challenging due to the difficulty of finding inclusions with identical area and shape while varying only their depth.

7.11.2 Fisheye formation in two stages and effect of inclusion depth

Figures 6.23c and 6.25 presented fisheye formation in two stages. A transition from smooth to rough area during fisheye growth was reported also by Stanzl-Tschegg et al. [46,47] who found that the transition from smooth to

rough fisheye structure goes along with a considerable increase in crack growth rate [47]. Figure 6.25a shows that the fisheye radius corresponds to the roughness and waviness of the fracture surface independent of the applied treatment, which means for both TMT and HT specimens with increasing fisheye radius, the roughness and waviness of the fisheye surface become more significant and at the fisheye radius of 300 µm a transition from smooth to rough fisheye occurs. Therefore, the formation of fisheye in one or two stages depends only on the inclusion depth (see Figure 6.25b), and different treatments do not affect the fisheye formation and the subsequent crack propagation. This was expected as the TMT is assumed to strengthen the microstructure around the inclusions and not in the bulk. The data points in both diagrams of Figure 6.25a and 6.25b exhibit a high degree of correlation, which means that the size of inclusion depth is almost the same as the radius of fisheye and indicating that fisheyes grow in a circular pattern originating from the critical inclusion until they extend to the surface. Figures 6.25a and 6.25b confirm subsections 7.11.1 and 6.10.5 that the crack propagation stage comprises only a small portion of the total fatigue lifetime. To have a reliable evaluation of fatigue lifetime, it is essential to consider other parameters such as the shape and stress concentration around the inclusions that lead to initiation of the crack.

7.11.3 Influence of TMT on the depth of inclusion and fisheye formation

It is observed from Figure 6.25 that the sizes of fisheyes and the corresponding inclusion depths of TMT specimens are considerably larger than for HT specimens. The first scenario for the interpretation of the reason for the larger inclusion depth of TMT specimens compared to HT ones might be due to the temperature difference between the area near the surface and the volume in a specimen. During the TMT a radial temperature gradient in the specimen's gauge length occurred. Inductive heating was used to reach the temperature of TMT (265 °C) and the process was measured and controlled at the specimen surface. The soaking time is 15 s at 265 °C before the mechanical loading begins in order to minimize purely thermal effects. Since during the TMT, only the temperature at the surface was measured, it could be possible that the internal temperature of the specimens did not reach 265 °C when the mechanical loading began. If the temperature inside the gauge length at the center of the specimen would be considerably lower than 265 °C, the strengthening DSA effects might not be as effective as at the surfaces and subsurfaces. Consequently, the crack initiation might occur from the there. To analyse the homogeneity of the temperature at the surface and volume in the gauge length of the specimen simulation and experimental analyses were conducted.

- **Simulation of the temperature profile at a certain point at the center of the gauge length during TMT soaking time**

Three thermocouples were employed at the top, middle, and bottom of the gauge length to ensure uniform temperature across the entire surface of the gauge length. However, the temperature inside the gauge length was not measured during the soaking time. Since the distance from the center of the gauge length inside the volume to the surface of the gauge length is at its maximum, this point was chosen for simulation to represent a worst-case scenario. The point is to determine, after 15 seconds of soaking time, whether the furthest distance to the surface of the gauge length also reaches 265 °C or not.

The temperature profile in a central point at the gauge length of the specimen during the soaking time of TMT is simulated by SolidWorks using a very fine mesh to determine the required time at a point in the center of the gauge length to reach 265 °C when the initial internal temperature of the specimen is 20 °C and the surface temperature of the specimen is 265 °C (see Figure 7.5).

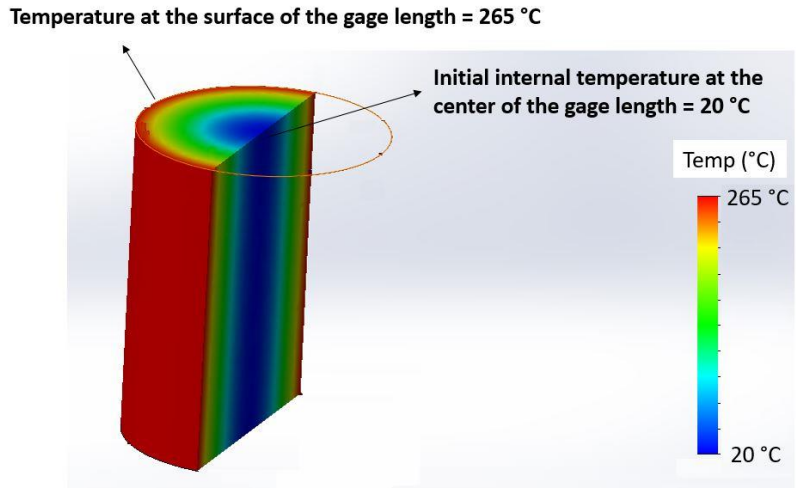

Figure 7.5 Initial temperature distribution across the surface and volume of the gage length at the beginning of the simulation.

Since during the soaking time of TMT, the thermoelement showed that the surface temperature reached the desirable temperature (265 °C). It was only important to see how the internal temperature inside the volume of the specimen changes over time. If we reach the same temperature within a soaking time of 15 s, then one can assume that even the entire volume of the specimen has a homogenous temperature after a soaking time of 15 s. Figure 7.6 exhibits a simulation of the temperature profile inside the gauge length at a certain point at the center of the gauge length during TMT soaking time. Figure 7.6 shows that at the time of 2 s the center of the specimen already reaches 265 °C and then it remains constant. Since the thermal conductivity of 42CrMo4 is high and the gauge length volume of the specimen is small,

thus, the result of the simulation was expectable. According to simulation, it can be assumed that after 15 s of soaking time the whole gauge length has the temperature of 265 °C. As shown in Figure 7.5, initially, the temperature at the surface of the specimen is maintained at 265°C through the induction system and is measured by a thermocouple. As a result, only thermal conduction plays role in the simulation of the time required for the center of the specimen to reach the same temperature as the surface and heat loss during simulation is negligible.

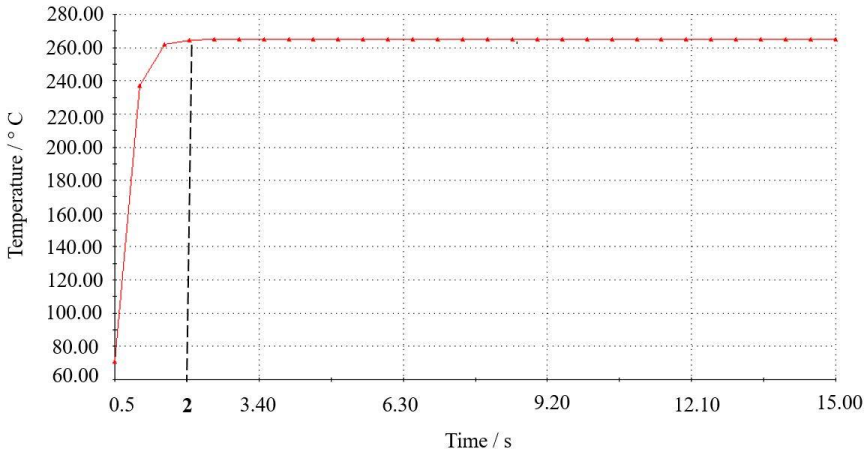

Figure 7.6 Temperature profile simulation at a certain point at the center of gauge length during TMT soaking time.

- **Experimental analysis of temperature at a certain point at the center of the gauge length during TMT soaking time**

The temperature at a certain point at the center of the gauge length was also measured experimentally using sheathed thermocouple during the soaking time of TMT. The result shows that during the heating of the specimen, the internal temperature rises almost the same as the surface temperature with a minor difference of 2 °C to 3 °C. It is observed that when the surface temperature reaches 265° C after a couple of seconds the internal temperature also reaches 265° C. The experimental results of soaking time during TMT confirm the simulation results and prove that there is no temperature difference between the surface and the volume of the specimen after 15 s soaking time.

This shows that possibly the main reason for the larger sizes of fisheyes and the corresponding inclusion depths of TMT specimens is a better TMT strengthening influence around the inclusions near the surface in comparison with the inclusions positioned deeper in the volume, resulting in shifting the crack initiation site further into the volume of the specimen. It can be assumed that the plastic deformation during the TMT is more significant in near-surface regions because the respective grains have no neighboring grains in the direction to the surface.

7.12 Analysis of the effect of increasing soaking time on the fatigue lifetime and hardness

As previously mentioned in subsection 6.1.4, the TMT soaking time was increased from 15 s to 300 s to ensure that the temperature all over the gauge length reached 265 °C and analyse the influence of this duration increase on the fatigue lifetime. According to subsection 6.9.1, a remarkable decrease in the fatigue lifetime of the TMT specimens has been observed after increasing the soaking time to 300 s (see subsection 6.9.1). Figure 6.18 exhbits an average hardness decrease of 50 HV in the gauge length of the TMT specimens after increasing the soaking time. As discussed in subsection 7.2, during thermal treatment a transformation in the microstructure from martensite to tempered martensite occurs. Since tempered martensite is inherently softer than martensite, a reduction in hardness within the microstructure is observable [88]. Significant reduction in the hardness is due to the increased soaking time, resulting in an earlier initiation of the cracks as well as an increased crack growth rate. This leads to a more rapid propagation of cracks through the material and ultimately resulting in a reduction in fatigue lifetime and earlier specimen failure [14,98,99]. Increasing the soaking time during TMT can be considered as a long TT which relates to a significant decrease in the hardness. A remarkable reduction in the fatigue lifetimes of the specimens after increasing the soaking time reveals that applying increasing cyclic mechanical load in the temperature of maximum DSA after a notable reduction in the hardness not only can enhance

the fatigue lifetime but also it could cause a significant decrease in the fatigue lifetime.

8 Summary and conclusion

In this study, three major fields of fatigue strength of quenched and tempered steel have been investigated and analysed which are summarized as follows:

(1) Effect of a thermo-mechanical treatment (TMT) in the temperature of maximum DSA on fatigue behaviour.

(2) Analysis of the influence of shape, type, inclusion depth, and site of critical non-metallic inclusions of HT and TMT specimens on the crack initiation, crack propagation, and fatigue lifetime.

(3) Analysis of the fatigue behaviour of TT, MT, and shot peened TMT treatments individually and making comparisons with the combined TMT.

(1) Effect of a thermo-mechanical treatment (TMT) in the temperature of maximum DSA on the fatigue behaviour

A suitable TMT was found and applied with the optimum temperature of 265 °C and a gradually increasing stress amplitude of 600 MPa1600 MPa. It has been shown that a TMT at the temperature of maximum DSA not only can increase the fatigue lifetime and delays the fatigue failure but also it improves the fatigue strength in the HCF regime ($N_f \geq 7 \times 10^5$ cycles)

by more than 50 MPa (8%). It has been found that the critical non-metallic inclusions inside the volume of both TMT and HT specimens are the main reason for crack initiation and failure of the specimens for $N_f \geq 7 \times 10^5$ cycles. Moreover, it has been observed that the maximum stress intensity factors of critical inclusions for the TMT specimens are higher than those for the reference specimens (HT). This means that the damage tolerance of the microstructure around the inclusions was increased by the TMT which is due to the strengthening of the microstructure around the critical non-metallic inclusions. On the other hand, in case of crack initiation from the surface and subsurface ($N_f < 7 \times 10^5$ cycles), the TMT decreases the fatigue resistance and leads to a reduction in the fatigue lifetime. Residual stress analysis showed that after TMT and due to the applied cyclic tensile–compressive mechanical loading during TMT a significant tensile residual stress at the surface and subsurface of the specimens was generated which eventually caused earlier crack initiation and fatigue failure of TMT specimens.

(2) Analysis of the influence of shape, type, inclusion depth, and site of critical non-metallic inclusions of HT and TMT specimens on the crack initiation, crack propagation, and fatigue lifetime

The effect of shape, type, inclusion depth and site of critical non-metallic inclusions of HT and TMT specimens on the lifetime, internal crack initiation and crack propagation behaviours under high cycle fatigue loading was investigated at a constant stress amplitude of 775 MPa. It has been observed that all specimens failed due to internal cracks, which were initiated at oxide inclusions of type AlCaO ($CaO\text{-}Al_2O_3$). Furthermore, for both TMT and HT specimens, the area of the critical inclusion and the inclusion depth have no significant effect on the overall fatigue lifetime. However, the shape of non-metallic inclusion plays a significant role in the crack initiation and failure of both TMT and HT specimens. It has been observed that smaller inclusions including sharp edges can be as detrimental as larger ones without sharp edges, which is due to the stress concentration near the sharp edges. Depending on the shape of critical inclusion, the minimum required inclusion area for the crack initiation and its corresponding stress intensity factor may vary. This means that eye-shaped inclusions and inclusions with sharp edges can lead to crack initiation and failure of the specimen even with smaller inclusions and maximum stress intensity factor compared to the bigger round ones. The results of the fatigue experiments at a constant stress amplitude of 775 MPa also show that the depth of inclusions correlates strongly with the fisheye radius. This confirms the growth of internal cracks in fisheye mode until they reach the surface. Afterwards, oxygen-assisted crack growth produces a distinguishable fracture surface. No effect of TMT can be seen on the inclusion depth, fisheye growth, and crack propagation. It has been identified that for both TMT and HT specimens, after

reaching a certain depth of inclusion the fracture surface appearance changes from smooth to a rougher wavy form, which is possibly the transition to crack propagation in the Paris regime. Another remarkable point is that for both TMT and HT specimens, no correlation between inclusion depth and lifetime could be found. Hence, the lifetime is predominantly governed by the number of cycles until crack initiation and the crack propagation stage comprises only a small portion of the lifetime.

(3) Analysis of the fatigue behaviour of TT, MT and shot peened TMT treatments individually and making comparisons with the combined TMT.

It has been observed that for $N_f \geq 7 \times 10^5$ cycles, where the crack initiation is from non-metallic inclusion inside the volume, the only treatment which can increase the fatigue strength of quenched and tempered steel is a thermo-mechanical treatment (TMT) which is the combination of TT and MT. MT and TT individually have no remarkable and negative effects on fatigue strength and lifetime, respectively. As well, for $N_f < 7 \times 10^5$ cycles, where the crack initiation is at the surface and subsurface, no improvement in the fatigue lifetime of TT and MT compared to HT can be observed. Similar to TMT, it has been found that the applied cyclic mechanical loading during MT leads to a significant reduction of compressive residual stress at the surface and subsurface of the specimens. Shot peening was used to regenerate the compressive residual stresses at the surface and subsurface of the TMT specimens and to improve the fatigue lifetimes for $N_f <$

7×10^5 cycles. The residual stress analysis indicates that after shot peening considerable compressive residual stresses have been regenerated at the surface and subsurface of TMT specimens, which leads to a longer lifetime for TMT specimens in the LCF regime. The fatigue behaviour analysis shows even a longer fatigue lifetime for TMT specimens after shot peening compared to HT ones which is due to increasing the hardness and higher amounts of regenerated compressive residual stress at the surface and subsurface. However, for $N_f \geq 7 \times 10^5$ cycles, where cracks initiate typically at inclusions inside the volume of the specimens, the generated compressive residual stresses at the surface and subsurface of shot-peened specimens have no remarkable effect on the enhancement of fatigue lifetime and behaviour. After all, the results prove that by applying a TMT in the temperature of maximum DSA and subsequently shot-peening of the specimens' surface, it is possible to achieve a better fatigue behaviour of quenched and tempered steel for both $N_f < 7 \times 10^5$ cycles and $N_f \geq 7 \times 10^5$ cycles.

9 References

1. Murakami, Y. Quantitative Evaluation of Effects of Non-Metallic Inclusions on Fatigue Strength of High Strength Steels. I: Basic Fatigue Mechanism and Evaluation of Correlation between the Fatigue Fracture Stress and the Size and Location of Non-Metallic Inclusions. **1989**, 8, doi:https://doi.org/10.1016/0142-1123(89)90054-6.
2. Kucharski, P.; Lesiuk, G.; Szata, M. Description of Fatigue Crack Growth in Steel Structural Components Using Energy Approach - Influence of the Microstructure on the FCGR.; Fojutowo, Poland, **2016**; p. 050003 doi:10.1063/1.4965950.
3. Starke, P.; Walther, F.; Eifler, D. Fatigue Assessment and Fatigue Life Calculation of Quenched and Tempered SAE 4140 Steel Based on Stress–Strain Hysteresis, Temperature and Electrical Resistance Measurements. *Fat Frac Eng Mat Struct* **2007**, *30*, 1044–1051, doi:10.1111/j.1460-2695.2007.01174.x.
4. Li, K.-S.; Gu, L.-H.; Wang, X.-R.; Wang, J.; Wang, R.-Z.; Gu, H.-H.; Zhang, X.-C.; Tu, S.-T. A Unified Rule for High-Cycle and Low-Cycle Fatigue Life Prediction in Multi-Scale Framework. *International Journal of Fatigue* **2023**, *170*, 107512, doi:10.1016/j.ijfatigue.2023.107512.
5. Mughrabi, H. Fatigue, an Everlasting Materials Problem - Still En Vogue. *Procedia Engineering* **2010**, *2*, 3–26, doi:10.1016/j.proeng.2010.03.003.
6. Mughrabi, H. On ‘Multi-Stage’ Fatigue Life Diagrams and the Relevant Life-Controlling Mechanisms in Ultrahigh-Cycle Fatigue: On ‘Multi-Stage’ Fatigue Life Diagrams. *Fatigue & Fracture of*

Engineering Materials & Structures **2002**, *25*, 755–764, doi:10.1046/j.1460-2695.2002.00550.x.
7. Mughrabi, H. Specific Features and Mechanisms of Fatigue in the Ultrahigh-Cycle Regime. *International Journal of Fatigue* **2006**, *28*, 1501–1508, doi:10.1016/j.ijfatigue.2005.05.018.
8. Lipiński, T.; Wach, A.; Detyna, E. Influence Of Large Non-Metallic Inclusions On Bending Fatigue Strength Hardened And Tempered Steels. *Advances in Materials Science* **2015**, *15*, 33–40, doi:10.1515/adms-2015-0013.
9. Li, W.; Deng, H.; Liu, P. Interior Fracture Mechanism Analysis and Fatigue Life Prediction of Surface-Hardened Gear Steel under Axial Loading. *Materials* **2016**, *9*, 843, doi:10.3390/ma9100843.
10. Guo, J.; Han, S.; Chen, X.; Guo, H.; Yan, Y. Control of Non-Metallic Inclusion Plasticity and Steel Cleanliness for Ultrathin 18 Pct Cr-8 Pct Ni Stainless Steel Strip. *Metall Mater Trans B* **2020**, *51*, 1813–1823, doi:10.1007/s11663-020-01862-4.
11. Yang, Z.G.; Li, S.X.; Zhang, J.M.; Zhang, J.F.; Li, G.Y.; Li, Z.B.; Hui, W.J.; Weng, Y.Q. The Fatigue Behaviors of Zero-Inclusion and Commercial 42CrMo Steels in the Super-Long Fatigue Life Regime. *Acta Materialia* **2004**, *52*, 5235–5241, doi:10.1016/j.actamat.2004.06.031.
12. Yang, C.; Luan, Y.; Li, D.; Li, Y.; Tariq, N. ul H. Very High Cycle Fatigue Behavior of Bearing Steel with Rare Earth Addition. *International Journal of Fatigue* **2020**, *131*, 105263, doi:10.1016/j.ijfatigue.2019.105263.
13. Kerscher, E.; Lang, K.; Vohringer, O.; Lohe, D. Increasing the Fatigue Limit of a Bearing Steel by Dynamic Strain Ageing. *International Journal of Fatigue* **2008**, *30*, 1838–1842, doi:10.1016/j.ijfatigue.2008.02.003.
14. Kerscher, E.; Lang, K.-H.; Löhe, D. Increasing the Fatigue Limit of a High-Strength Bearing Steel by Thermomechanical Treatment.

Materials Science and Engineering: A **2008**, *483–484*, 415–417, doi:10.1016/j.msea.2006.09.170.
15. Kerscher, E. *Steigerung der Schwingfestigkeit von 100Cr6 durch thermomechanische Behandlungen*; Schriftenreihe Werkstoffwissenschaft und Werkstofftechnik; Shaker: Aachen, **2005**; ISBN 978-3-8322-4100-1.
16. Xie, J.P.; Wang, A.Q.; Wang, W.Y.; Li, J.W.; Yang, D.X.; Zhang, K.F.; Ma, D.Q. Stress Field Numerical Simulation of the Inclusions in Large Rudder Arm Steel Casting. *AMR* **2011**, *311–313*, 906–909, doi:10.4028/www.scientific.net/AMR.311-313.906.
17. Guan, J.; Wang, L.; Zhang, C.; Ma, X. Effects of Non-Metallic Inclusions on the Crack Propagation in Bearing Steel. *Tribology International* **2017**, *106*, 123–131, doi:10.1016/j.triboint.2016.10.030.
18. Shiozawa, K.; Murai, M.; Shimatani, Y.; Yoshimoto, T. Transition of Fatigue Failure Mode of Ni–Cr–Mo Low-Alloy Steel in Very High Cycle Regime. *International Journal of Fatigue* **2010**, *32*, 541–550, doi:10.1016/j.ijfatigue.2009.06.011.
19. Shiozawa, K.; Hasegawa, T.; Kashiwagi, Y.; Lu, L. Very High Cycle Fatigue Properties of Bearing Steel under Axial Loading Condition. *International Journal of Fatigue* **2009**, *31*, 880–888, doi:10.1016/j.ijfatigue.2008.11.001.
20. Liu, P.; Li, W.; Nehila, A.; Sun, Z.; Deng, H. High Cycle Fatigue Property of Carburized 20Cr Gear Steel under Axial Loading. *Metals* **2016**, *6*, 246, doi:10.3390/met6100246.
21. Krewerth, D.; Lippmann, T.; Weidner, A.; Biermann, H. Influence of Non-Metallic Inclusions on Fatigue Life in the Very High Cycle Fatigue Regime. *International Journal of Fatigue* **2016**, *84*, 40–52, doi:10.1016/j.ijfatigue.2015.11.001.
22. Lei, Z.; Hong, Y.; Xie, J.; Sun, C.; Zhao, A. Effects of Inclusion Size and Location on Very-High-Cycle Fatigue Behavior for High

Strength Steels. *Materials Science and Engineering: A* **2012**, *558*, 234–241, doi:10.1016/j.msea.2012.07.118.

23. Costa e Silva, A.L.V. da The Effects of Non-Metallic Inclusions on Properties Relevant to the Performance of Steel in Structural and Mechanical Applications. *Journal of Materials Research and Technology* **2019**, *8*, 2408–2422, doi:10.1016/j.jmrt.2019.01.009.
24. Taheri, F.; Trask, D.; Pegg, N. Experimental and Analytical Investigation of Fatigue Characteristics of 350WT Steel under Constant and Variable Amplitude Loadings. *Marine Structures* **2003**, *16*, 69–91, doi:10.1016/S0951-8339(02)00004-7.
25. Holzapfel, H.; Schulze, V.; Vöhringer, O.; Macherauch, E. Residual Stress Relaxation in an AISI 4140 Steel Due to Quasistatic and Cyclic

Loading at Higher Temperatures. *Materials Science and Engineering: A* **1998**, *248*, 9–18, doi:10.1016/S0921-5093(98)00522-X.
26. M. Benachour; N. Benachour; M. Benguediab Fatigue Crack Initiation And Propagation Through Residual Stress Field. **2012**, doi:10.5281/ZENODO.1081623.
27. Wildeis, A.; Christ, H.-J.; Brandt, R. Influence of Residual Stresses on the Crack Initiation and Short Crack Propagation in a Martensitic Spring Steel. *Metals* **2022**, *12*, 1085, doi:10.3390/met12071085.
28. Sippel, J.; Kerscher, E. Influence of a Thermomechanical Treatment on the Lifetime of a High Strength Steel in Very High Cycle Fatigue.; Malaga, Spain, **2023,** doi: 10.1063/5.0145133.
29. *Elements of Metallurgy and Engineering Alloys*; Campbell, F.C., Ed.; ASM International: Materials Park, Ohio, **2008**; ISBN 978-0-87170-867-0.
30. W . A . J . Albert ; über Treibseile am Harz," Die Bergwerks-Verwaltung des Hannoverschen Ober-Harzes in den Jahren 1831–1836, pp. 215–234, Dec. **1837**, doi: 10.1515/9783111515229-009.
31. A. Wöhler: Versuch Über Die Festigkeit Der Eisenbahnwagenachsen. Zeitschrift Für Bauwesen 10, **1860**.
32. Murakami, Y.; Takagi, T.; Wada, K.; Matsunaga, H. Essential Structure of S-N Curve: Prediction of Fatigue Life and Fatigue Limit of Defective Materials and Nature of Scatter. *International Journal of Fatigue* **2021**, *146*, 106138, doi:10.1016/j.ijfatigue.2020.106138.
33. Chang, K.-H. Fatigue and Fracture Analysis. In *e-Design*; Elsevier: Oklahoma, USA, **2015**; pp. 463–521 ISBN 978-0-12-382038-9.
34. Jelaska, D.T.; Podrug, S.; Glodez, S. Comparison of Numerical Models for Gear Tooth Root Fatigue Assessments. In Proceedings of the Recent Advances in Solids and Structures; ASMEDC: Orlando, Florida, USA, January 1 **2005**; pp. 77–84, doi: 10.1115/imece2005-79891.
35. Jelaska, D.T.; Glodez, S.; Podrug, S. Numerical Modelling of the Crack Propagation Path at Gear Tooth Root. In Proceedings of the

Volume 4: 9th International Power Transmission and Gearing Conference, Parts A and B; ASMEDC: Chicago, Illinois, USA, January 1 **2003**; pp. 201–207, doi: 10.1115/detc2003/ptg-48026..
36. Nishijima; Kanazawa Stepwise *S-N* Curve and Fish-Eye Failure in Gigacycle Fatigue: GIGACYCLE FAILURE. *Fatigue & Fracture of Engineering Materials & Structures* **1999**, *22*, 601–607, doi:10.1046/j.1460-2695.1999.00206.x.
37. Shiozawa, K.; Lu, L.; Ishihara, S. *S-N* Curve Characteristics and Subsurface Crack Initiation Behaviour in Ultra-Long Life Fatigue of a High Carbon-Chromium Bearing Steel: S -N CURVE AND CRACK INITIATION IN ULTRA-LONG LIFE FATIGUE. *Fatigue & Fracture of Engineering Materials & Structures* **2001**, *24*, 781–790, doi:10.1046/j.1460-2695.2001.00459.x.
38. Zettl, B.; Stanzl-Tschegg, S.; Mayer, H. Crack Initiation Mechanisms and Fatigue Lifetime of AISI 420 Steel under Constant and Variable Amplitude Loading.VHCF-4 Fourth International Conference on Very High Cycle Fatigue University of Michigan, Ann Arbor, Michigan USA TMS (The Minerals, Metals & Materials Society), August 19-22, **2007**.
39. Zhu, X.; Dong, Z.; Zhang, Y.; Cheng, Z. Fatigue Life Prediction of Machined Specimens with the Consideration of Surface Roughness. *Materials* **2021**, *14*, 5420, doi:10.3390/ma14185420.
40. *ASM Handbook. Volume 19: Fatigue and Fracture*; 4. print.; ASM International: Materials Park, Ohio, **2005**; ISBN 978-0-87170-385-9.
41. Sarma, D.S.; Karasev, A.V.; Jönsson, P.G. On the Role of Non-Metallic Inclusions in the Nucleation of Acicular Ferrite in Steels. *ISIJ International* **2009**, *49*, 1063–1074, doi:10.2355/isijinternational.49.1063.
42. Spriestersbach, D.; Grad, P.; Kerscher, E. Crack Initiation Mechanisms and Threshold Values of Very High Cycle Fatigue

Failure of High Strength Steels. *Procedia Engineering* **2014**, *74*, 84–91, doi:10.1016/j.proeng.2014.06.229.
43. Liu, D.; Wang, Z.; Liu, J.; Wang, Z.; Zuo, X. Study of the Fracture Behavior of TiN and TiC Inclusions in NM550 Wear-Resistant Steel during the Tensile Process. *Metals* **2022**, *12*, 363, doi:10.3390/met12020363.
44. Toribio, J.; Ayaso, F.-J.; González, B. Role of Non-Metallic Inclusions in the Fracture Behavior of Cold Drawn Pearlitic Steel. *Metals* **2021**, *11*, 962, doi:10.3390/met11060962.
45. Lang, K.-H.; Korn, M.; Rohm, T. Very High Cycle Fatigue Resistance of the Low Alloyed Steel 42CrMo4 in Medium- and High-Strength Quenched and Tempered Condition. *Procedia Structural Integrity* **2016**, *2*, 1133–1142, doi:10.1016/j.prostr.2016.06.145.
46. Stanzl-Tschegg, S.E. Fracture Mechanical Characterization of the Initiation and Growth of Interior Fatigue Cracks: Fracture Mechanics for Interior Fatigue Cracks. *Fatigue Fract Engng Mater Struct* **2017**, *40*, 1741–1751, doi:10.1111/ffe.12622.
47. Stanzl-Tschegg, S.; Schönbauer, B. Near-Threshold Fatigue Crack Propagation and Internal Cracks in Steel. *Procedia Engineering* **2010**, *2*, 1547–1555, doi:10.1016/j.proeng.2010.03.167.
48. Li, Y.-D.; Zhang, L.-L.; Fei, Y.-H.; Liu, X.-Y.; Li, M.-X. On the Formation Mechanisms of Fine Granular Area (FGA) on the Fracture Surface for High Strength Steels in the VHCF Regime. *International Journal of Fatigue* **2016**, *82*, 402–410, doi:10.1016/j.ijfatigue.2015.08.021.
49. Deng, H.; Li, W.; Sakai, T.; Sun, Z. Very High Cycle Fatigue Failure Analysis and Life Prediction of Cr-Ni-W Gear Steel Based on Crack Initiation and Growth Behaviors. *Materials* **2015**, *8*, 8338–8354, doi:10.3390/ma8125459.
50. Deng, H.; Li, W.; Zhao, H.; Sakai, T. Multiple Fatigue Failure Behaviors and Long-Life Prediction Approach of Carburized Cr-Ni

Steel with Variable Stress Ratio. *Materials* **2017**, *10*, 1084, doi:10.3390/ma10091084.
51. Murakami, Y. Material Defects as the Basis of Fatigue Design. *International Journal of Fatigue* **2012**, *41*, 2–10, doi:10.1016/j.ijfatigue.2011.12.001.
52. Murakami, Y. Effects of Small Defects and Nonmetallic Inclusions on the Fatigue Strength of Metals. *JSME international journal. Ser. 1, Solid mechanics, strength of materials* **1989**, *32*, 167–180, doi:10.1299/jsmea1988.32.2_167.
53. Schönbauer, B.M.; Ghosh, S.; Kömi, J.; Frondelius, T.; Mayer, H. Influence of Small Defects and Nonmetallic Inclusions on the High and Very High Cycle Fatigue Strength of an Ultrahigh-strength Steel. *Fatigue Fract Eng Mat Struct* **2021**, *44*, 2990–3007, doi:10.1111/ffe.13534.
54. Gu, C.; Liu, W.; Lian, J.; Bao, Y. In-Depth Analysis of the Fatigue Mechanism Induced by Inclusions for High-Strength Bearing Steels. *Int J Miner Metall Mater* **2021**, *28*, 826–834, doi:10.1007/s12613-020-2223-9.
55. Zhang, Z. Cyclic Hardening/Softening. In *Encyclopedia of Tribology*; Wang, Q.J., Chung, Y.-W., Eds.; Springer US: Boston, MA, **2013**; pp. 687–691 ISBN 978-0-387-92896-8.
56. D'Hondt, C.; Doquet, V.; Couzinié, J.P. Cyclic Hardening/Softening and Deformation Mechanisms of a Twip Steel under Reversed Loading. *Materialia* **2022**, *22*, 101421, doi:10.1016/j.mtla.2022.101421.
57. Mulford, R.A.; Kocks, U.F. New Observations on the Mechanisms of Dynamic Strain Aging and of Jerky Flow. *Acta Metallurgica* **1979**, *27*, 1125–1134, doi:10.1016/0001-6160(79)90130-5.
58. Sleeswyk, A.W. Slow Strain-Hardening of Ingot Iron. *Acta Metallurgica* **1958**, *6*, 598–603, doi:10.1016/0001-6160(58)90101-9.
59. Mardoukhi, A.; Rämö, J.; Vuoristo, T.; Roth, A.; Hokka, M.; Kuokkala, V.-T. Effects of Microstructure on the Dynamic Strain

Aging of Ferriticpearlitic Steels at High Strain Rates. *EPJ Web Conf.* **2018**, *183*, 03009, doi:10.1051/epjconf/201818303009.
60. Hörnqvist, M.; Karlsson, B. Temperature and Strain Rate Effects on the Dynamic Strain Ageing of Aluminium Alloy AA7030. *MSF* **2006**, *519–521*, 883–888, doi:10.4028/www.scientific.net/MSF.519-521.883.
61. Bergström, Y.; Roberts, W. The Application of a Dislocation Model to Dynamical Strain Ageing in α-Iron Containing Interstitial Atoms. *Acta Metallurgica* **1971**, *19*, 815–823, doi:10.1016/0001-6160(71)90138-6.
62. Robinson, J.M.; Shaw, M.P. Microstructural and Mechanical Influences on Dynamic Strain Aging Phenomena. *International Materials Reviews* **1994**, *39*, 113–122, doi:10.1179/imr.1994.39.3.113.
63. Yilmaz, A. The Portevin–Le Chatelier Effect: A Review of Experimental Findings. *Science and Technology of Advanced Materials* **2011**, *12*, 063001, doi:10.1088/1468-6996/12/6/063001.
64. de Oliveira, M.; Couto, A.; Almeida, G.; Reis, D.; de Lima, N.; Baldan, R. Mechanical Behavior of Inconel 625 at Elevated Temperatures. *Metals* **2019**, *9*, 301, doi:10.3390/met9030301.
65. Pohl, K.; Mayr, P.; Macherauch, E. Cyclic Deformation Behavior of a Low Carbon Steel in the Temperature Range between Room Temperature and 850 K. *Int J Fract* **1981**, *17*, 221–233, doi:10.1007/BF00053521.
66. Kerscher, E.; Lang, K.-H. Influence of Thermal and Thermomechanical Treatments on the Fatigue Limit of a Bainitic

High-Strength Bearing Steel. *Procedia Engineering* **2010**, *2*, 1731–1739, doi:10.1016/j.proeng.2010.03.186.
67. Lu, J.; Society for Experimental Mechanics (U.S.) *Handbook on Residual Stress. Vol. 2, Vol. 2*,; Society for Experimental Mechanics: Bethel, CT, **2005**; ISBN 978-0-912053-92-9.
68. Okamoto, A.; Nakamura, H. The Influence of Residual Stress on Fatigue Cracking. *Journal of Pressure Vessel Technology* **1990**, *112*, 199–203, doi:10.1115/1.2928614.
69. Withers, P.J.; Bhadeshia, H.K.D.H. Residual Stress. Part 2 – Nature and Origins. *Materials Science and Technology* **2001**, *17*, 366–375, doi:10.1179/026708301101510087.
70. Morikage, Y.; Igi, S.; Oi, K.; Jo, Y.; Murakami, K.; Gotoh, K. Effect of Compressive Residual Stress on Fatigue Crack Propagation. *Procedia Engineering* **2015**, *130*, 1057–1065, doi:10.1016/j.proeng.2015.12.263.
71. Torres, M. An Evaluation of Shot Peening, Residual Stress and Stress Relaxation on the Fatigue Life of AISI 4340 Steel. *International Journal of Fatigue* **2002**, *24*, 877–886, doi:10.1016/S0142-1123(01)00205-5.
72. Watanabe, Y.; Hattori, K.; Handa, M.; Hasegawa, N.; Tokaji, K.; Ikeda, M.; Duchazeaubeneix, J.-M. Effect of Ultrasonic Shot Peening on Fatigue Strength of High Strength Steel. In *Shot Peening*; Wagner, L., Ed.; Wiley-VCH Verlag GmbH & Co. KGaA: Weinheim, FRG, **2006**; pp. 305–310 ISBN 978-3-527-60658-0.
73. Miki, C.; Mori, T.; Tajima, J. Effect Of Stress Ratio And Tensile Residual Stress On Near Threshold Fatigue Crack Growth. *Doboku Gakkai Ronbunshu* **1986**, *1986*, 187–194, doi:10.2208/jscej.1986.368_187.
74. A. Ohta, N. Suzuki, and Y. Maeda, “Unique fatigue threshold and growth properties of welded joints in a tensile residual stress field,”

International Journal of Fatigue, vol. 19, no. 93, pp. 303–310, Jun. **1997**, doi: 10.1016/s0142-1123(97)00049-2.
75. Iurea, P.; Carausu, C. Considerations Concerning the Causes and Effects of the Occurrence of Residual Stresses in Metallic Materials: A Review. *AMM* **2014**, *659*, 91–100, doi:10.4028/www.scientific.net/AMM.659.91.
76. James, M.R. Relaxation Of Residual Stresses An Overview. In *Residual Stresses*; Elsevier, **1987**; pp. 349–365 ISBN 978-0-08-034062-3.
77. Vöhringer, O. Relaxation Of Residual Stresses By Annealing Or Mechanical Treatment In *Residual Stresses*; Elsevier, **1987**; pp. 367–396 ISBN 978-0-08-034062-3.
78. Mühl, F.A. Simulationsgestützte Prozessoptimierung des Wärmebehandlungsverfahrens Internal Quenching. **2022**, doi:10.5445/IR/1000145728.
79. Müller, C.; Wächter, M.; Masendorf, R.; Esderts, A. Accuracy of Fatigue Limits Estimated by the Staircase Method Using Different Evaluation Techniques. *International Journal of Fatigue* **2017**, *100*, 296–307, doi:10.1016/j.ijfatigue.2017.03.030.
80. Ekaputra, I.M.W.; Dewa, R.T.; Haryadi, G.D.; Kim, S.J. Fatigue Strength Analysis of S34MnV Steel by Accelerated Staircase Test. *Open Engineering* **2020**, *10*, 394–400, doi:10.1515/eng-2020-0048.
81. Wolfstieg, U. Das ψ-Goniometer. *HTM Härtereitechnische Mitteilungen* **1976**, *31*, 19–22.
82. Macherauch, E.; Müller, P. Das Sin2ψ-Verfahren Der Röntgenographischen Spannungsmessung. *Zeitschrift für Angew. Phys.* **1961**, *13*, 305–312.
83. Wolfstieg, U. Die Symmetrisierung Unsymmetrischer Interferenzlinien Mit Hilfe von Spezialblenden. *HTM - J. Heat Treat. Mater.* **1976**, *31*, 24–26.
84. Eigenmann, B.; Macherauch, E. Röntgenographische Untersuchung von Spannungszuständen in Werkstoffen. Teil III. Fortsetzung von

Matwiss. und Werkstofftechn. Heft 3/1995, S. 148-160 und Heft 4/1995, S. 199-216. *Mat.-wiss. u. Werkstofftech.* **1996**, *27*, 426–437, doi:10.1002/mawe.19960270907.

85. Holmberg, J.; Berglund, J.; Stormvinter, A.; Andersson, P.; Lundin, P. Influence of Local Electropolishing Conditions on Ferritic–Pearlitic Steel on X-Ray Diffraction Residual Stress Profiling. *J. of Materi Eng and Perform* **2023**, doi:10.1007/s11665-023-08525-w.
87. *DIN EN ISO 6508-1:2016-12, Metallische Werkstoffe_- Härteprüfung Nach Rockwell_- Teil_1: Prüfverfahren (ISO_6508-1:2016); Deutsche Fassung EN_ISO_6508-1:***2016**; Beuth Verlag GmbH;
87. Ismail, N.M.; Khatif, N.A.A.; Kecik, M.A.K.A.; Shaharudin, M.A.H. The Effect of Heat Treatment on the Hardness and Impact Properties of Medium Carbon Steel. *IOP Conf. Ser.: Mater. Sci. Eng.* **2016**, *114*, 012108, doi:10.1088/1757-899X/114/1/012108.
88. Yudo, H.; Jokosisworo, S. The Effect of Low Tempering, Medium Tempering, and High Tempering Heating Temperature Variations in the Type of Medium Carbon Steel ST 60 on Microstructure, Hardness, and Toughness. *IOP Conf. Ser.: Mater. Sci. Eng.* **2021**, *1052*, 012047, doi:10.1088/1757-899X/1052/1/012047.
89. Pavlíčková, M.; Vojtech, D.; Novák, P.; Gemperlová, J.; Gemperle, A.; Zárubová, N.; Jurči, P.; Lejček, P. Influence of Thermal Treatment on Microstructure and Hardness of Niobium Alloyed PM-Tool Steel. *Instrumentation Science & Technology* **2004**, *32*, 207–219, doi:10.1081/CI-120028773.
91. Naoe, T.; Harjo, S.; Kawasaki, T.; Xiong, Z.; Futakawa, M. Change in Mechanical Properties by High-Cycle Loading Up to Gigacycle for 316L Stainless Steel. In Proceedings of the Proceedings of the 14th International Workshop on Spallation Materials Technology; Journal of the Physical Society of Japan: Fukushima, Japan, February 6 **2020**, doi: 10.7566/jpscp.28.061009..
92. Chai, G. Transitions of Fatigue Crack Initiation from Surface, Subsurface to SNDFCO. In *Fracture of Nano and Engineering*

Materials and Structures; Gdoutos, E.E., Ed.; Springer Netherlands: Dordrecht, **2006**; pp. 195–196 ISBN 978-1-4020-4971-2.

92. Saklakoglu, N.; Bolouri, A.; Irizalp, S.G.; Baris, F.; Elmas, A. Effects of Shot Peening and Artificial Surface Defects on Fatigue Properties of 50CrV4 Steel. *Int J Adv Manuf Technol* **2021**, *112*, 2961–2970, doi:10.1007/s00170-020-06532-y.
93. Breuner, C.; Guth, S.; Gall, E.; Swadźba, R.; Gibmeier, J.; Heilmaier, M. Influence of Shot Peening on the Isothermal Fatigue Behavior of the Gamma Titanium Aluminide Ti-48Al-2Cr-2Nb at 750 °C. *Metals* **2021**, *11*, 1083, doi:10.3390/met11071083.
95. Shiozawa, K.; Lu, L. Very High-Cycle Fatigue Behaviour of Shot-Peened High-Carbon-Chromium Bearing Steel: .Very High-cycle Fatigue Behaviour *Fatigue & Fracture of Engineering Materials & Structures* **2002**, *25*, 813–822, doi:10.1046/j.1460-2695.2002.00567.x.
95. Hong, S.-G.; Lee, S.-B. Dynamic Strain Aging under Tensile and LCF Loading Conditions, and Their Comparison in Cold Worked 316L Stainless Steel. *Journal of Nuclear Materials* **2004**, *328*, 232–242, doi:10.1016/j.jnucmat.2004.04.331.
96. Hong, S.-G.; Lee, S.-B. Mechanism of Dynamic Strain Aging and Characterization of Its Effect on the Low-Cycle Fatigue Behavior in Type 316L Stainless Steel. *Journal of Nuclear Materials* **2005**, *340*, 307–314, doi:10.1016/j.jnucmat.2004.12.012.
97. Ren, Y.; Yang, W.; Zhang, L. Deformation of Non-Metallic Inclusions in Steel during Rolling Process: A Review. *ISIJ Int.* **2022**, *62*, 2159–2171, doi:10.2355/isijinternational.ISIJINT-2022-235.
98. Schmiedel, A.; Kirste, T.; Morgenstern, R.; Weidner, A.; Biermann, H. The Fatigue Life of 42CrMo4 Steel in the Range of HCF to VHCF

at Elevated Temperatures up to 773 K. *International Journal of Fatigue* **2021**, *152*, 106437, doi:10.1016/j.ijfatigue.2021.106437.
99. Suzuki, H.; Mcevily, A.J. Microstructural Effects on Fatigue Crack Growth in a Low Carbon Steel. *MTA* **1979**, *10*, 475–481, doi:10.1007/BF02697075.
100. Kumar, R.; Behera, R.K.; Sen, S. Effect of Tempering Temperature and Time on Strength and Hardness of Ductile Cast Iron. *IOP Conf. Ser.: Mater. Sci. Eng.* **2015**, *75*, 012015, doi:10.1088/1757-899X/75/1/012015.
101. Kreethi, R.; Mondal, A.K.; Dutta, K. Ratcheting Induced Cyclic Softening Behaviour of 42CrMo4 Steel. *IOP Conf. Ser.: Mater. Sci. Eng.* **2015**, *75*, 012027, doi:10.1088/1757-899X/75/1/012027.
103. K. Hussain and E. R. de los Rios, "Monotonic and cyclic stress-strain behaviour of a structural steel," Scripta Metallurgica et Materialia, vol. 28, no. 6, pp. 757–762, Mar. **1993**, doi: 10.1016/0956-716x(93)90049-x.
104. Neves, F.O.; Oliviera, T.L.L.; Braga, D.U.; Silva, A.S.C. da Influence of Heat Treatment on Residual Stress in Cold-Forged Parts. *Advances in Materials Science and Engineering* **2014**, 1–6, doi:10.1155/2014/658679.
105. Callister, W.D.; Rethwisch, D.G. *Materials Science and Engineering: An Introduction*; 10th edition.; John Wiley & Sons, Inc.: Hoboken, NJ, **2018**; ISBN 978-1-119-40549-8.
106. Becker, Martin, et al. Prediction and measurement of phase transformations, phase-dependent properties and residual stresses in steels. No. LM-05K049. KAPL (Knolls Atomic Power Laboratory (KAPL), Niskayuna, NY), **2005**.
107. Ohta, Akihiko, et al. "Fatigue. Fatigue Strength Improvement of Lap Joints of Thin Steel Plates for Automobile Use by Using Low Transformation Temperature Welding Material." Journal of the

Society of Materials Science, Japan, vol. 50, no. 10, 1 Jan. **2001**, pp. 1086–1090, https://doi.org/10.2472/jsms.50.1086.
107. Ota, A.; Shiga, C.; Maeda, Y.; Suzuki, N.; Watanabe, O.; Kubo, T.; Matsuoka, K.; Nishijima, S. Fatigue Strength Improvement of Box-welded Joints Using Low Transformation Temperature Welding Material. *Welding International* **2000**, *14*, 801–805, doi:10.1080/09507110009549271.
108. Alghamdi, A.; Alharthi, H.A. Finite Element Simulation of the Effect of Phase Transformation on Residual Stress in a Thick Section T-Joint. *Crystals* **2022**, *12*, 1422, doi:10.3390/cryst12101422.
109. Alves, J.M.; Paula, A. dos S.; Brandao, L.P. Residual Stress Analysis After the Induced Martensitic Transformation by Rolling and Tensile Test in the 304L TRIP Steel. *Mat. Res.* **2021**, *24*, e20210156, doi:10.1590/1980-5373-mr-2021-0156.
110. Maleki, E.; Farrahi, G.H.; Reza Kashyzadeh, K.; Unal, O.; Gugaliano, M.; Bagherifard, S. Effects of Conventional and Severe Shot Peening on Residual Stress and Fatigue Strength of Steel AISI 1060 and Residual Stress Relaxation Due to Fatigue Loading: Experimental and Numerical Simulation. *Met. Mater. Int.* **2021**, *27*, 2575–2591, doi:10.1007/s12540-020-00890-8.
111. Luong, H.; Hill, M.R. The Effects of Laser Peening and Shot Peening on High Cycle Fatigue in 7050-T7451 Aluminum Alloy. *Materials Science and Engineering: A* **2010**, *527*, 699–707, doi:10.1016/j.msea.2009.08.045.
112. Aguado-Montero, S.; Vázquez, J.; Navarro, C.; Domínguez, J. Optimal Shot Peening Residual Stress Profile for Fatigue. *Theoretical and Applied Fracture Mechanics* **2021**, *116*, 103109, doi:10.1016/j.tafmec.2021.103109.
114. Vohringer, O. Changes In The State Of The Material By Shot Peening. *Conf Proc: ICSP-3, (p.185-204* **1987**.
115. Slat, W.S.; Malau, V.; Iswanto, P.T. The Effects of Shot Peening Treatment on the Hardness and Fatigue Strength of HQ 805. In

Proceedings of the 2018 International Conference on Applied Science and Technology (iCAST); IEEE: Manado, Indonesia, October **2018**; pp. 142–145.
115. Pan, C.; Hu, X.; Zheng, J.; Lin, P.; Chou, K. Effect of Calcium Content on Inclusions during the Ladle Furnace Refining Process of AISI 321 Stainless Steel. *Int J Miner Metall Mater* **2020**, *27*, 1499–1507, doi:10.1007/s12613-020-1981-8.
116. Ånmark, N.; Karasev, A.; Jönsson, P. The Effect of Different Non-Metallic Inclusions on the Machinability of Steels. *Materials* **2015**, *8*, 751–783, doi:10.3390/ma8020751.
117. Bernard, G.; Riboud, P.V.; Urbain, G. Étude de La Plasticité d'inclusions d'oxydes. *Rev. Met. Paris* **1981**, *78*, 421–434, doi:10.1051/metal/198178050421.